METAL OXIDE NANOCRYSTALLINE THIN FILMS AS BUFFER LAYERS IN ORGANIC/ HYBRID SOLAR CELLS

BY

NORMAN MARK BOWERS

A thesis submitted in fulfilment of the requirement for the degree of Magister Scientiae in the Department of Physics and Astronomy, University of the Western Cape (UWC).

Supervisor: Dr T.F.G. Muller (UWC)
Co-supervisor: Prof C.J. Arendse (UWC)

November 2019

DEDICATION

This thesis is dedicated to my mother, Joyce Bowers and my father, Noel Bowers.

KEYWORDS

Metal oxide nanocrystalline thin films as buffer layers in organic/hybrid solar cells.

Nanocrystalline

Thin film

Metal oxide

Sol-gel

Spin coating

Annealing

Electron blocking

Hole blocking

Organic

Solar cell

ABSTRACT

Metal oxide nanocrystalline thin films as buffer layers in organic/hybrid solar cells

N. M. Bowers

MSc. Thesis, Department of Physics and Astronomy, University of the Western Cape

Without reverting to encapsulation, organic bulk - heterojunction solar cells can be protected from the oxidation of the highly reactive low work function cathode metal electrode, by the deposition of metal oxide buffer layers onto an indium-tin oxide (ITO) substrate. The zinc-oxide (ZnO) or titanium dioxide (TiO_2) layer can serve as an electron collecting contact. In such a case the ordering of layer deposition is inverted from the traditional layer sequencing, using an additional effect of the metal oxide layer acting as a hole blocking contact. In this study an investigation of metal oxide layers such as zinc oxide (ZnO) and titanium dioxide (TiO_2) was performed. The application of these nanocrystalline thin films was done by the sol-gel process, and eventually thermal evaporation of powders. Solar cells were manufactured with active layers of blends of poly (3-hexylthiophene) (P3HT), as electron donor and [6,6]-phenyl-C61-butyric acid methyl ester (PCBM) as electron acceptor. The effect of the incorporation of these buffer layers on the device efficiency was investigated with electrical measurements. Molybdenum trioxide layers were utilized as electron blocking layer.

November 2019

DECLARATION

I declare that, "*Metal oxide nanocrystalline thin films as buffer layers in organic/hybrid solar cells"* is my own work, that is has not been submitted for any degree or examination in any other university, and that all the sources I have used or quoted have been indicated and acknowledged by complete references.

Full name: Norman Mark Bowers Date: 26 November 2019

Signed: 

ACKNOWLEDGEMENTS

Firstly, I would like to thank God my Creator and Sustainer, for providing me with the intellect, to pursue my dreams. Without Him this would not have been possible.

I would like to express my deepest and heartfelt gratitude's to the following people and organisations without whose assistance and support, the completion of this study would not have been possible.

My supervisor Dr T.F.G. Muller for his excellent supervision, encouragement guidance and support. Working with him has been a great experience of my life and I thank him for that and for always showing interest in my progress.

My co-supervisor, Prof C.J. Arendse for his enlightening advice and expertise in photovoltaics.

The National Research Foundation, iThemba Labs and University of the Western Cape for financial support.

The Electron Microscope Unit (UWC), Dr F.R. Cummings, Miss N. Peterson, Mr E. McDonald, Mr A. Josephs and Miss N. Kensley for always opening their arms whenever I needed to do SEM and/or TEM characterisations.

Miss A. Adams and Mr S. Mqhayi, the administrators of the Department of Physics and Astronomy, UWC, for their support.

The staff of the Department of Physics and Astronomy (UWC) and the MANUS/ MATSCI group, R. Lindsay, S. Khanyile, S. Ngqoloda, S. Magubane, R. Khunou, S. Magogodi, C. Ngwetsheni, M. Masevhe, S.

Mthembu and L. Fourie for their inspiration, motivation and encouragements throughout the duration of my studies.

To my immediate, extended family and friends I would like to thank thee for their patience, encouragement, consistent love and support throughout this journey I will forever appreciate the fact that you believed in me:
Firstly, my mother Joyce Bowers, my pillar of strength, for always guiding and inspiring me to never give up. Then my father for his wisdom and leadership. My siblings Erin and Evelene, always being there for me in times of need. Also, my brother-in-law, Donovan for his support and motivation.

Last but not least, I would like to thank Estrenita for her support, motivation and comfort through difficult times. Thank you for your love, patience and understanding through this period.

LIST OF TABLES

LIST OF FIGURES

LIST OF ABBREVIATIONS, ACRONYMS AND SYMBOLS

acetic acid - (AA)

aluminium - (Al)

amorphous silicon - (a-Si)

angle - (θ)

attenuation coefficient - (κ)

bulk-heterojunction - (BHJ)

Cadmium Telluride - (Cd-Te)

carbon dioxide - (CO_2)

chemical vapour deposition - (cvd)

conduction band - (CB)

conventionally annealed - (ca)

Copper - (Cu)

copper indium gallium diselenide - (CIGS)

Current - Voltage - (I-V)

depth of field - (DOF)

dye-sensitized hybrid solar cells - (DSSC)

efficiency - (η_e)

electron energy-loss near edge structure - (ELNES)

electron energy-loss spectroscopy - (EELS)

electron transport layer - (ETL)

electron volt - (eV)

energy band gap - (E_g)

Energy Dispersive Spectroscopy - (EDS)

ethanolamine - (MEA)

Everhart-Thornley detector - (ETD)

Fermi level - (E_f)

field-emission gun - (FEG)

fill factor - (FF)

Focused Ion Beam - (FIB)

Focused Ion Beam Scanning Electron Microscopy - (FIB-SEM)

Fourier transform infrared - (FTIR)

gallium ion - (Ga^{+})

Gold - (Au)

Grazing incident X-ray diffraction - (GIXRD)

greenhouse gas - (GHG)

high work function - (HWF)

highest occupied molecular orbital - (HOMO)

High-resolution scanning electron microscopy - (HR-SEM)

High-resolution transmission electron microscopy - (HR-TEM)

hole blocking layer - (HBL)

hole transport layer - (HTL)

Hybrid solar cells - (HSCs)

hydrogenated silicon - (Si:H)

incident solar power density - (P_{in})

Indium-tin oxide - (ITO)

infrared - (IR)

Kubelka–Munk - (K–M)

Lanthanum hexaboride - (LaB6)

lithium fluoride - (LiF)

low work function - (LWF)

lowest unoccupied molecular orbital - (LUMO)

millibar - (mbar)

Molybdenum oxide - (MoO_x)

Molybdenum Trioxide - (MoO_3)

crystalline silicon solar cells - (c-Si)

multi-crystal silicon - (mc-Si)

nanometer - (nm)

National Renewable Energy Laboratory - (NREL)

Nickel oxide - (NiO)

open-circuit - (V_{oc})

organic photovoltaic cells - (OPV)

organic solar cell - (OSC)

oxygen - (O_2)

Phenyl-C61-butyric acid methyl ester - (PCBM)

photoelectrochemical cells - (PEC)

photovoltaic - (PV)

pi - (π)

poly (3, 4- ethylenedioxythiophene): poly(styrenesulfonate)- (PEDOT: PSS)

Poly 3-hexylthiophene - (P3HT)

power conversion efficiency - (PCE)

ramp-annealed - (ra)

revolution per minute - (rpm)

selected-area electron diffraction - (SAED)

short circuit - (I_{sc})

shunt resistance - (R_{sh})

sigma - (σ)

Silver - (Ag)

single-crystal silicon - (c-Si)

Titanium dioxide - (TiO_2)

titanium isopropoxide - (TTIP)

transition metal oxides - (TMOs)

Transmission Electron Microscopy - (TEM)

Transmission – T(ω)

Tungsten oxide - (WO_3)

Ultra violet - (UV)

Ultraviolet-visible - (UV-Vis)

valence band - (VB)

Vanadium oxide - (V_2O_5)

wave vector - (k)

wavelength - (λ)

wavenumber - (ω)

X-ray diffraction - (XRD)

Zinc acetate dehydrate - (ZAD)

zinc oxide - (ZnO)

CONTENT

CHAPTER ONE

1 Introduction and Literature review

1.1 Solar energy utilized as an alternative energy source.

The demand for global energy has increased during the last century and became a cause for concern. This is due to the expansion of the human population and the advancement in technology which require an increased supply of energy. During the last century, the consumption of fossil fuels remained the primary source of energy. Unfortunately, the result of burning fossil fuels for energy is increasing carbon dioxide (CO_2) emission which contributes to greenhouse gas (GHG) emission and is related to climate change. By employing renewable energy resources on a larger scale in this century, there is a potential for reduction of GHG emission, hence solving or addressing the environmental problem of global warming and reducing the depletion rate of fossil fuels as predicted (Shafiee and Topal, 2006) [1.1-1.3].

Renewable energy generation technology makes use of natural environmental cycles to generate electricity, which includes solar energy, hydropower, wind energy, biomass energy, etc. Renewable energy is sustainable and non-polluting [1.4]. In order to address issues regarding climate change and global warming, solar energy is an excellent alternative renewable energy source due to its renewability, sustainability and cleanliness. As shown in Figure 1.1, the annual solar irradiation in South Africa is a good indicator as a possible source of energy for electricity production since radiant energy is in abundance over this region [1.5-1.7].

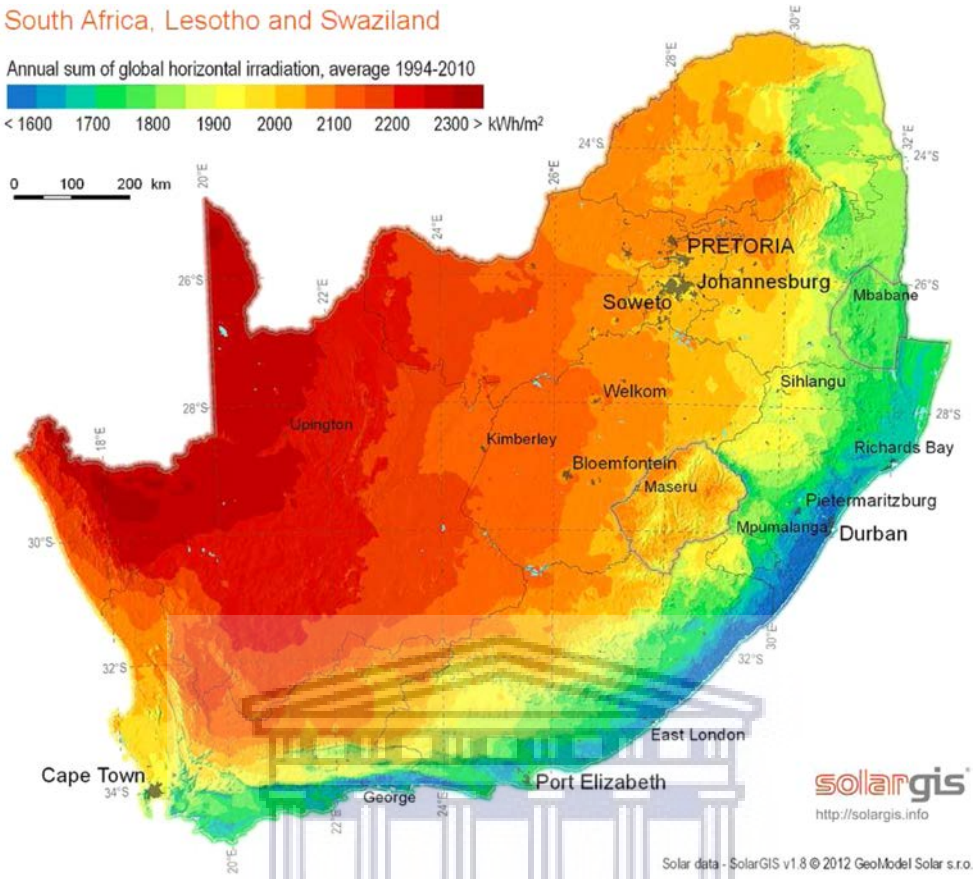

Figure 1.1: Solar irradiation across South Africa [1.6].

Solar energy can be harvested directly from the sun by utilizing light or heat. The solar radiation can be gathered and used without converting it. On the other hand, by using mechanical and electrical equipment the solar irradiation can be converted into heat and electricity [1.8].

1.2 Photovoltaics

1.2.1 Discovery of Photovoltaics

In 1839, Alexandre-Edmund Becquerel, a French physicist made history by discovering the photovoltaic (PV) effect. Becquerel found that when solid electrodes (selenium) were immersed into an electrolyte a small electric current arose when illuminated by white light. Later, in 1954 the first silicon solar cell with 6% efficiency was developed in Bell Laboratories [1.9].

Since then the efficiencies of solar cells have reached 24% for mono-crystalline silicon solar cells (c-Si). Photovoltaics is becoming more accepted as an important form of power generation due to its reliability and very low operational and maintenance costs, as shown in Figure 1.2 [1.9, 1.10].

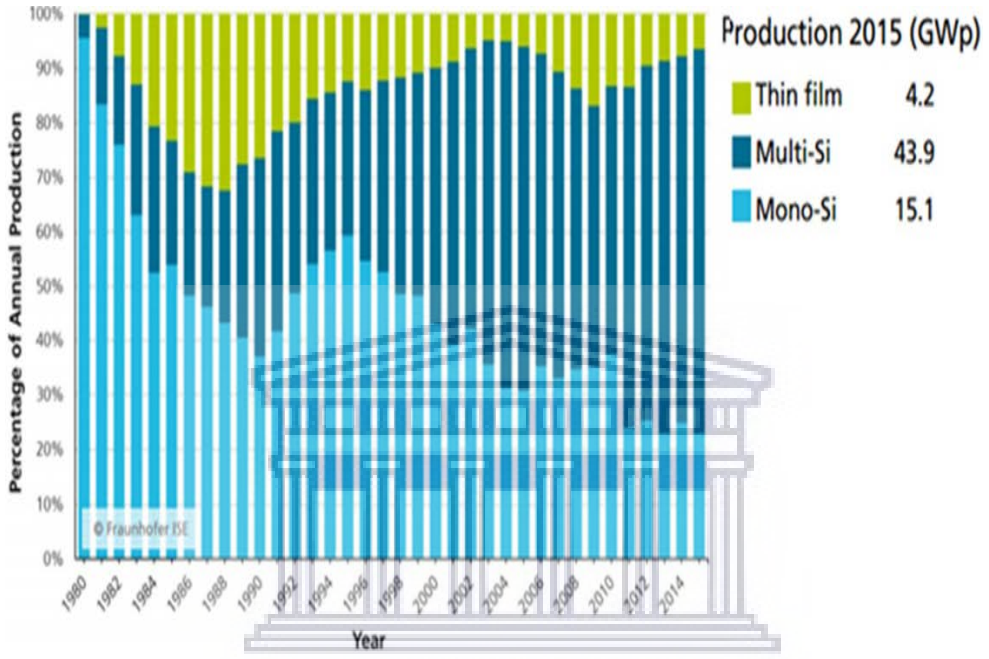

Figure 1.2: Global PV production by technology [1.9].

1.2.2 Basic Principles of Photovoltaics

PVs makes use of the ability of semiconducting materials that exhibit the PV effect for the conversion of sunlight into electricity. Semiconductors are materials with photoconductivity which are suitable for photovoltaics.

A single atom contains atomic orbitals with discrete energy levels for holding electrons. According to the Pauli exclusion principle, these levels are allowed to only contain two electrons with different angular momentum (spin up and spin down) as illustrated in Figure 1.3. In a solid, these discrete energy levels merge to forms bands. This solid is known as a metal if the valance band is partially full, or if it overlaps in the energy with the lowest

unoccupied band. In semiconductors, we can distinguish between two distinct energy bands. [1.10]. At low temperatures, one energy band is completely filled with valence electrons, known as the valence band (VB). This energy band is separated from a partially filled conduction band (CB) by an energy band gap (E_g). Semiconductors are distinguished by their band gap ranging from 0.5 to 3 eV.

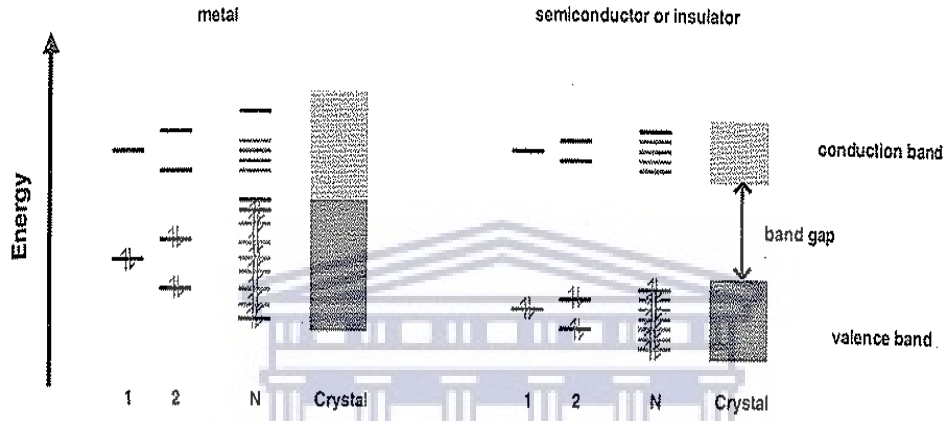

Figure 1. 3: Energy levels and bands of semiconductors [1.11].

In order for an electron to be excited from the VB into the CB, they require the energy of the incident photon to be equivalent to or greater than the band gap energy of the semiconductor material. When the photon energy is transferred to the valance electron it gains the required kinetic energy to be excited across the band gap, at this instance an electron-hole pair; also known as an exciton is created and the free electron can travel and transport charge or energy. If the VB maximum and the CB minimum share the same wave vector k, the photon of energy (E_g) is enough to form an exciton. This material is known as a direct band gap material, as shown in figure 1.4. For some materials the VB maximum and the CB minimum does not occur at the same wave vector k. Now, the photon with energy E_g on its own is not enough to excite the electron out of the valence band; extra momentum is thus needed. To create the exciton, the electron needs the energy that is absorbed from the photon, and momentum which is supplied by a lattice

vibration (phonon), such materials are known as indirect band gap materials [1.10, 1.11].

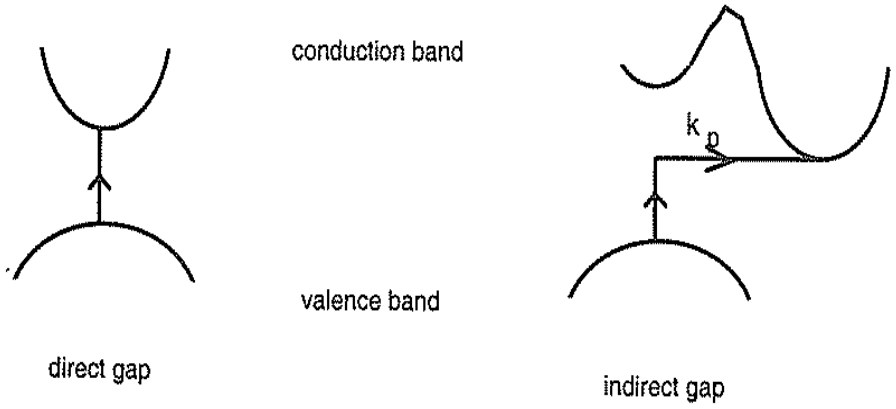

Figure 1. 4: Direct and indirect band gap [1.11].

Theoretically, the band gap determines the position of the Fermi level, described as the highest energy state occupied by electrons in a material at absolute zero temperature. The Fermi level is usually midway between the two bands for intrinsic semiconductors. The conductivity of intrinsic semiconductors can be improved with increasing the temperature and decreasing the band gap; electrons will then gain enough thermal energy to cross the lower band gap easily and be utilized by the PV effect for conducting electricity. Introducing impurities into the crystal structure modifies the electrical properties of the semiconductor resulting in an extrinsic semiconductor [1.11].

When doping a semiconducting material with an impurity atom the desired controlled changes introduce either electron acceptors or donors. Electron donors are formed when an extra electron is donated to the lattice, this material is called a n-type semiconductor. The extra electron can be easily stripped, leaving the donor atom positively charged. Donor electrons are promoted from the donor level into the conduction band. Since the donor states are filled at T = 0, the Fermi level (E_F) lies between the donor level and the conduction band. Another doping method is when an extra hole

(electron acceptor) is donated to the material; the material is said to be p-type. Here E_F now lies between the valance band and the acceptor level. Also notice from Figure 1.5, for an intrinsic material E_F lies roughly in the middle of the band gap.

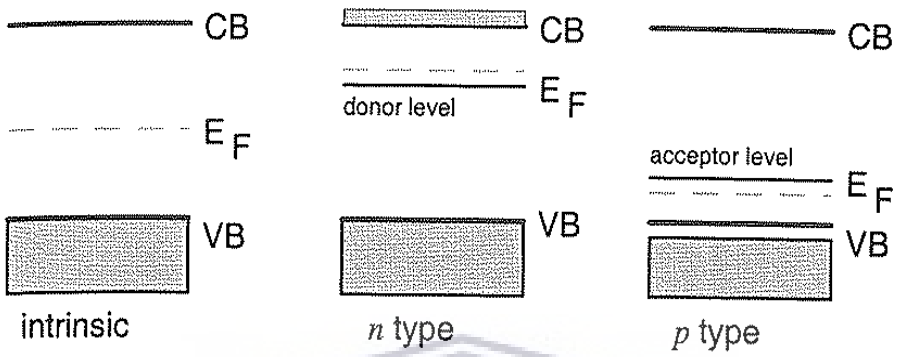

Figure 1. 5: Position of Fermi level [1.11].

Generation of excitons is known as an electronic excitation phenomenon which increases the number of free charge carriers. This may be due to the promotion of an electron from the VB to the CB which generates an exciton. It may also be the promotion from the valence band into a localised state in the band gap, which generates only a hole, or from a localised state into the conduction band, which generates only an electron. Recombination is the loss of an electron or hole through the decay of an electron to a lower state. This may be from band to band, stripping an exciton, or it may occur from the CB to a trap state or from a trap state to the VB; removing only an electron or a hole, respectively. This release of energy can be given up in the form of a photon (radiative recombination), as thermal energy through phonon emission (non-radiative recombination), or as kinetic energy to another free carrier (Auger recombination) [1.11].

1.2.3 Basic Photovoltaic device operation

A PV cell employs the PV effect by converting the energy of light directly into electricity by means of a p-n semiconductor junction. A p-n junction is

formed when we have an interface between n-type and p-type layers of semiconductor material. When the two layers are brought together an electrostatic potential is established. This occurs when electrons diffuse from the n-type into the p-type side, leaving behind a positively charged layer containing donors. Holes from the p-type side diffuse into the n-type side which leaves a negatively charged layer stripped of holes; hence an electrostatic potential is established. The interface region is left depleted of charge carriers; this boundary region is now known as the space charge/ depletion region. When visible radiation illuminates the solar cell, as depicted in Figure 1.6, the solar cell absorbs photons of wavelengths equal to or greater than the band gap energy of the semiconductor. This absorption leads to the creation of excitons on both sides of the junctions. The minority carriers on each side of the junction are then swept away by the electric field which in turn produces an electric current across the device [1.10].

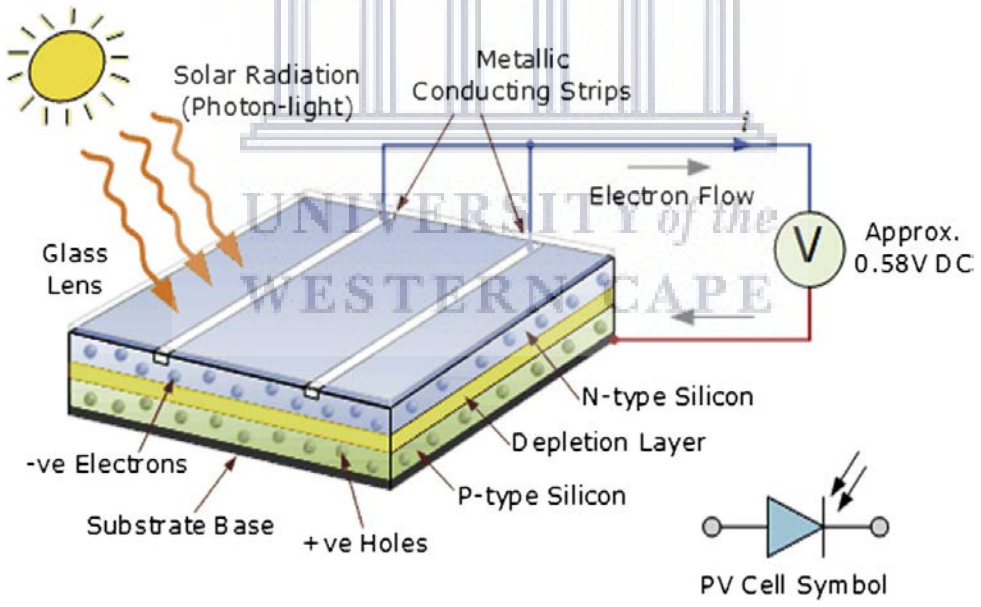

Figure 1. 6: Principle of photovoltaic device or charge transfer p-n junction [1.1].

1.3 Photovoltaic technologies

1.3.1 First Generation solar cells

The first generation solar cells are based on silicon (Si) wafers and this includes single-crystal (c-Si) and multi-crystal (mc-Si) silicon solar cells. Silicon cells account for nearly 90% of the solar cell market due to its abundance, stability and absorption of photons in a wide range of the electromagnetic visible spectrum [1.12]. For commercial use, first generation solar cells have a high efficiency of over 20 % and with the possibility of improving since they have a theoretical efficiency of up to 33 % [1.13]. However, the main disadvantages are due to the requirement of high purity silicon crystals, high fabrication temperatures, high material cost and the high manufacturing cost; as high as 70 % of the total manufacturing costs [1.14, 1.15].

1.3.2 Second Generation solar cells

In the need to reduce manufacturing cost, second generation solar cells were developed. These solar cells are based on thin film technology that provides the potential for reduced manufacturing cost, ascribed to the device requiring less material [1.13]. This generation mainly focusses on three types of thin film solar cells namely amorphous silicon (a-Si), Cadmium Telluride (Cd-Te) and copper indium gallium diselenide (CIGS). These thin films can be deposited onto substrates such as glass or transparent film. Also, these semiconductors require only 1-10µm thickness of photo-active material to absorb the solar spectrum much more efficiently compared to the thickness required for c-Si and mc-Si, which is 100 times less. The photovoltaic devices based on thin film technologies are much cheaper and have shown good efficiencies but they are still less efficient than c-Si technology devices [1.14, 1.16]. Therefore, further research and improvement of these devices are still needed.

1.3.3 Third Generation solar cells

Third generation technologies aspire to further enhance the poor electrical performance and quality of the second generation thin film technologies while maintaining very low production costs. The majority of the work on third generation solar cells are being explored in the laboratory and are being developed by new companies and most devices are still not commercially available. Currently, the third generation applications being investigated comprise of nanocrystal solar cells, photoelectrochemical cells (PEC), dye-sensitized hybrid solar cells (DSSC), tandem cells, organic photovoltaic cells (OPVs), and the cells constructed from the materials that generate multiple excitons. These cells are based on low energy and high-throughput processing technologies. For example, OPVs are chemically synthesized and solution-processable with high potential for large area deposition; they have low material costs and are lightweight and flexible. The Graetzel (DSSC) cell is an attractive replacement for existing technologies in low weight applications like rooftop solar collectors; they are seen to be working even in low-light conditions. However, the efficiencies of the first and second generation PV technologies still surpass all third generation cells. Secondly, their efficiencies decay over time due to the degradation effects under environmental conditions [1.16].

1.4 Organic photovoltaic devices

Amongst the various photovoltaic technologies that have been discovered, OPVs are the most promising [1.17]. Organic PVs have emerged as a promising PV technology due to its potential for low-cost production and deposition on flexible substrates. Research concerning OPVs has impressively improved over the past few years. Firstly, increasing the efficiency of OPVs towards and surpassing 10 % is an always-pervasive challenge. According to the National Renewable Energy Laboratory (NREL), the efficiency of OPVs (for various types) has grown since the

1980s from 0.8% to an efficiency of 11.5% in 2017, as shown in Figure 1.7 [1.18].

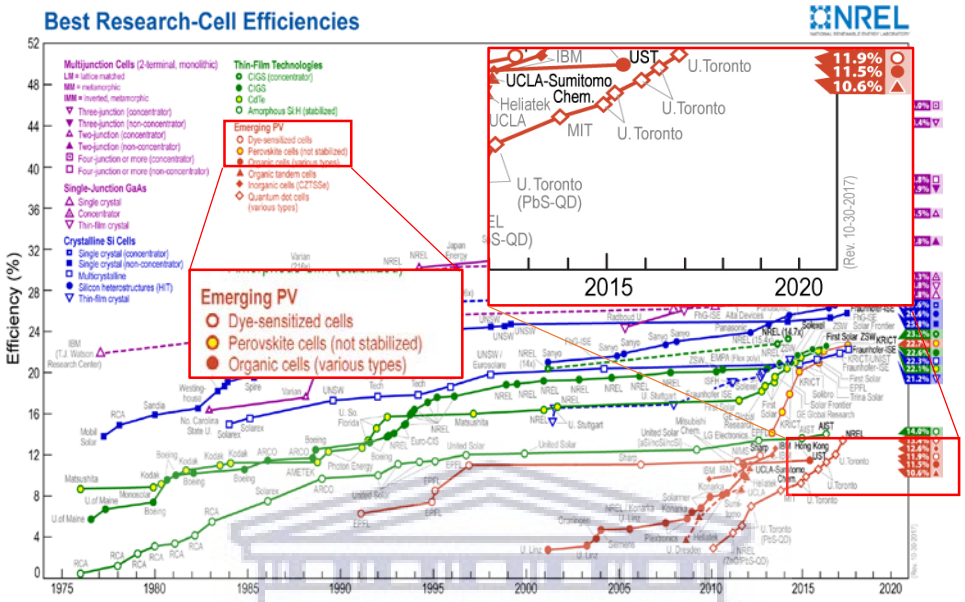

Figure 1.7: Best research cell-efficiencies for different technologies [1.18].

1.4.1 Organic solar cell-structure

An organic solar cell (OSC) is usually comprised of a combination of stacked layers with the active layer between two electrodes. A basic OSC structure, depicted in Figure 1.8, consists of distinct layers for device optimization. On top of the substrate, usually glass, is indium tin oxide (ITO) which is used as an electrode for its transparent and conducting properties that makes it suitable for light transmission into the photoactive material. The hole transport layer (HTL) facilitates in the extraction of dissociated holes and block electrons from diffusing backwards. Most commonly the HTL used is a conductive polymer mixture made of poly (3,4-ethylene dioxythiophene): poly (styrene sulfonate) (PEDOT: PSS). Next, on top of the HTL is deposited the photoactive layer made up of a donor and acceptor material and coated using a solution; responsible for light absorption for exciton generation, dissociation and charge carrier diffusion. Common donors are poly- (phenylene vinylene) derivatives and

poly- (alkylthiophene); common acceptors are fullerene and its derivatives. On top of the active layer is deposited an electron transport layer (ETL), such as lithium fluoride (LiF), which facilitates electron extraction and blocks holes from diffusing backwards. Finally, a metal contact (e.g. aluminium (Al)), is evaporated on top of the ETL by thermal evaporation.

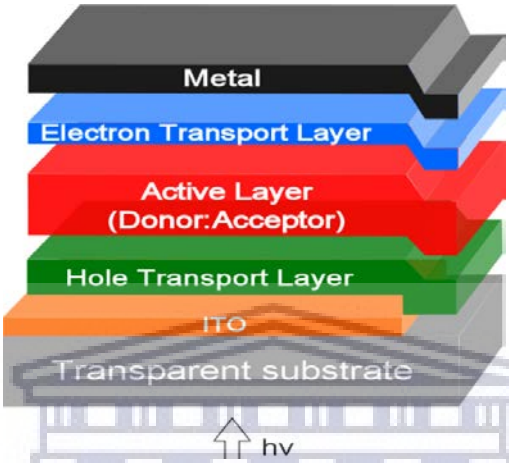

Figure 1. 8: Device architecture of a typical organic solar cell [1.23].

The first single-layered PV cell developed, Figure 1.9(a), consisted of an organic semiconductor layer sandwiched between a metal contact, ITO and a low work function metal such as aluminium. In this cell charge separation was inefficient. For the next type of cell, the efficiency of the donor/ acceptor bilayer cell, Figure 1.9(b), increased but only the light absorbed by a thin layer next to the interface contributed to the photocurrent, the rest is lost during recombination. For the third cell, as depicted in Figure 1.9(c), the bulk heterojunction PV cell provided more efficient charge separation since donor and acceptor materials are mixed [1.17,1.19].

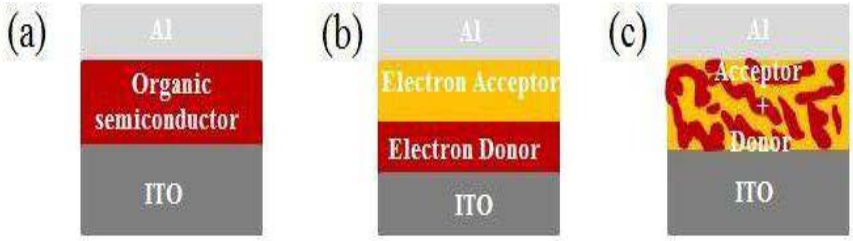

Figure 1. 9: The different architectures of organic photovoltaic cells: (a) single-layer PV cell, (b) bilayer PV cell and (c) conventional bulk heterojunction [1.17].

1.4.2 Hybrid solar cells

Hybrid solar cells (HSCs) consist of a combination of organic and inorganic materials where the unique properties of inorganic nanocrystal semiconductors are blended with the properties of organic/polymer materials. In HSCs, inorganic semiconductor nanostructures from a variety of metal oxides (e.g. ZnO, TiO_2) are commonly fabricated using various synthesis methods. These metal oxide nanostructures can be tailored by varying their sizes and shapes, crystallographic structure, or the optoelectronic properties to induce tunability of the optical band gap and absorption/ emission properties. The metal oxide also has higher mobility compared to the organic material; this improves charge transfer when the surface structure is modified. HSCs combine the excellent electronic properties of inorganic molecules with the reduced cost and the compatibility with flexible substrates. In order to achieve high HSC performance, both the electron and hole mobilities have to be balanced and optimized [1.20-1.23].

1.4.3 Inverted organic solar cells

The normal device structure usually consists of a bulk-heterojunction (BHJ) layer or planar heterojunction layer sandwiched between a high work function (HWF) and transparent metal oxide as bottom anode and a low

work function (LWF) metal as the top cathode [1.24]. Due to the instability of OSC devices in air caused by the degradation of the hole transporting layer (HTL), an inverted device, as schematically shown in Figure 1.10(b), is proposed to improve the lifetime and stability of such devices [1.25, 1.26]. A thin film of electron blocking polystyrene sulfonate (PEDOT: PSS) in such a structure is then used as a hole blocking layer (HBL) to match the required reversal of polarities of the electrodes. Nowadays, this polymer is replaced with a thin film of metal oxide, such as ZnO or TiO_2 since it shows superior atmospheric stability. The HTL is then made with oxides such as Molybdenum trioxide (MoO_3), vanadium pentoxide (V_2O_5), NiO and tungsten oxide (WO_3) [27]. Also, high work function electrodes such as silver and gold (Ag and Au) are introduced to minimise or avoid the oxidation process [1.28]. The electrons are then extracted at the ITO while holes are extracted at the metal electrode. This inverted configuration of the OSCs presents long term stability [1.29].

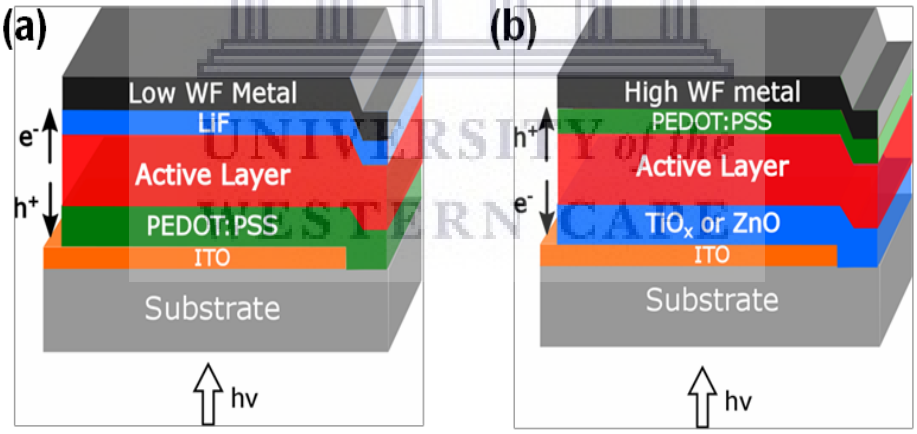

Figure 1. 10: Schematic of (a) conventional device (b) inverted device [1.23].

1.4.4 Operational mechanism in organic photovoltaic devices

Upon the absorption of a photon, an electron is excited from the highest occupied molecular orbital (HOMO) to the lowest unoccupied molecular orbital (LUMO), leaving behind a positive charge carrier in the HOMO,

called a hole. The generation of the electron-hole pair is known as an exciton [1.30]. As illustrated in Figure 1.11, the difference between the HOMO and LUMO energy levels of the polymer is defined as the optical band gap. After excitons are generated, dissociation is required for the electrons and holes in order for each to be transported to their respective electrodes. To achieve this charge separation an electric field is required which originates from the differences in the work function of the electrodes. Hence, electron flow is more favourable from the electrode with a low work function to the electrode with a high work function.

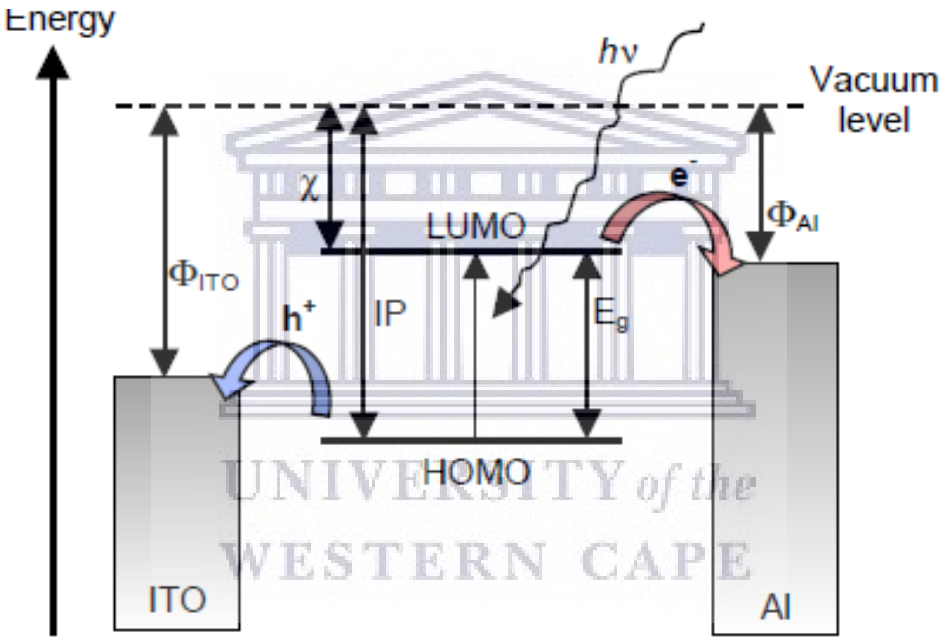

Figure 1. 11: Energy levels and photoelectric conversion mechanism [1.31].

1.5 Device Efficiency

The graph of current vs voltage in Figure 1.12 illustrates the properties of a solar cell in the dark and when exposed to light. When measured in complete darkness there will not be a flow of current due to lack of illumination. Only when the injection barrier is overcome can current start to flow. When the device is exposed to light, maximum power is produced [1.32, 1.33].

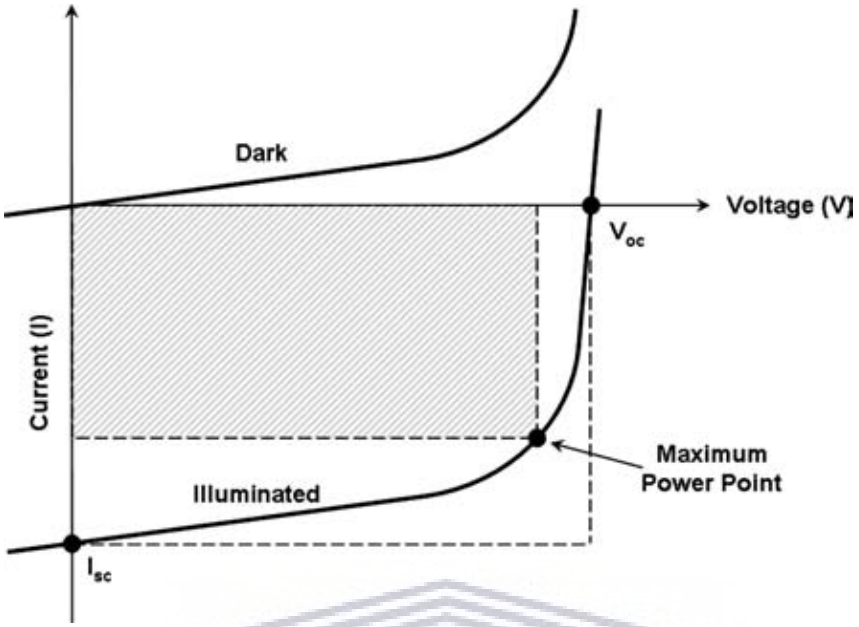

Figure 1. 12: Graph of current vs voltage for photovoltaic device illustrating device characteristics under illumination [1.32].

The photovoltaic power conversion efficiency η_e is determined by the following parameters:

$$\eta_e = \frac{V_{oc} \times I_{sc} \times FF}{P_{in}} \quad (1.1)$$

$$FF = \frac{I_{mmp} \times V_{mmp}}{I_{sc} \times V_{oc}} \quad (1.2)$$

where V_{oc} is the open-circuit voltage, I_{sc} is referred to as the short circuit current, which refers to current flow when there is no applied voltage. FF is the fill factor, and P_{in} is the incident solar power density. When I = 0, V_{oc} is the maximum voltage available from the solar cell. When V = 0, I_{sc} is the current that flows in the solar cell under illumination. The light intensity is standardized at 1000 W/m^2 with a spectral intensity distribution matching that of the sun on the earth's surface at an incident angle of 48.2°, which is called the AM1.5G spectrum. I_{mpp} and V_{mpp} are the current and voltage which represents the maximum power point on the I-V curve [1.32, 1.35].

1.6 Material properties of individual layers within the solar cell.

In this section, key materials will be presented as they are important for donor and acceptor characteristics. These material properties are necessary to determine how different they are from each other and how they will behave in response to each other and the environment. The stability, operating conditions and functionality of the materials are important to evaluate since they are beneficial for charge transport which can improve the exciton dissociation, thus improving device performance. Furthermore, the material properties give an indication of whether any chemical reactions may occur between the layers in the device, as well as diffusion into the active layer, which may restrict performance and stability.

1.6.1 Molybdenum Trioxide (MoO_3) as a hole transport layer (HTL)

Molybdenum trioxide (MoO_3), is a transition metal oxide which can exist in different crystalline polymorphs such as thermodynamically stable orthorhombic α- MoO_3 and metastable monoclinic β- MoO_3. The orthorhombic structure, Figure 1.13, is composed of layers of distorted MoO_6 octahedra [1.36, 1.37].

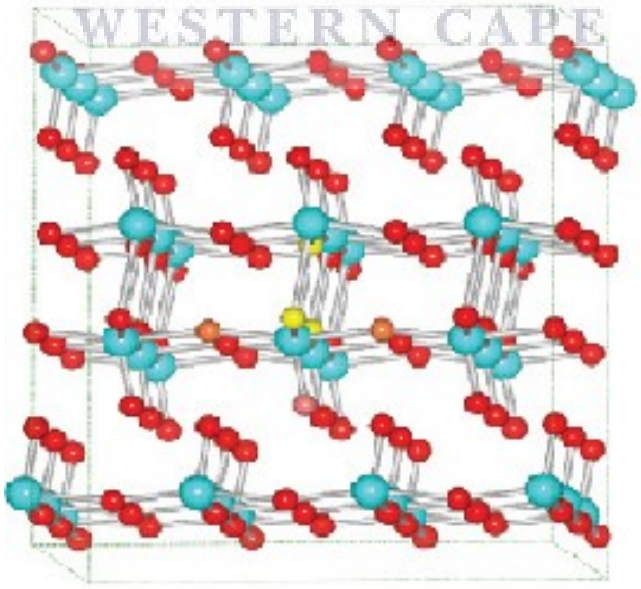

Figure 1. 13: Crystal structure of orthorhombic MoO_3 [1.36].

The lattice constants of the α- MoO_3 are as follows: a= 3.962Å, b = 13.855Å and c = 3.699Å. Stoichiometric MoO_3 is an insulator with an indirect wide band gap of (3.0 - 3.3 eV) and a high work function (>6 eV), with a corresponding electron affinity value of 2.3 eV and ionization energy of 5.3–5.4 eV. Conductivity variations ranges from insulating MoO_3 to semiconductor $Mo_{18}O_{52}$ (p=78.1Ω-cm) to the metallic Mo_4O_{11} (p=1.66×10^{-4} Ω-cm) [1.37- 1.40].

1.6.2 Titanium dioxide (TiO_2) as an electron transport layer (ETL)

TiO_2 also known as titania is a photosensitive semiconductor. It is a very well-known and well-researched material because of its interesting properties. TiO_2 can basically exist in three different crystalline phases as shown in Figure 1.14. Rutile and anatase phases have a tetragonal crystal structure while brookite has an orthorhombic crystalline structure. TiO_2 also have an amorphous phase. When exposed to UVA light (320nm – 400nm) the rutile and anatase phase has excellent photocatalytic and antibacterial properties. Rutile is a stable phase, whereas anatase and brookite are metastable phases and readily transformable to rutile phase under suitable conditions [1.40, 1.41].

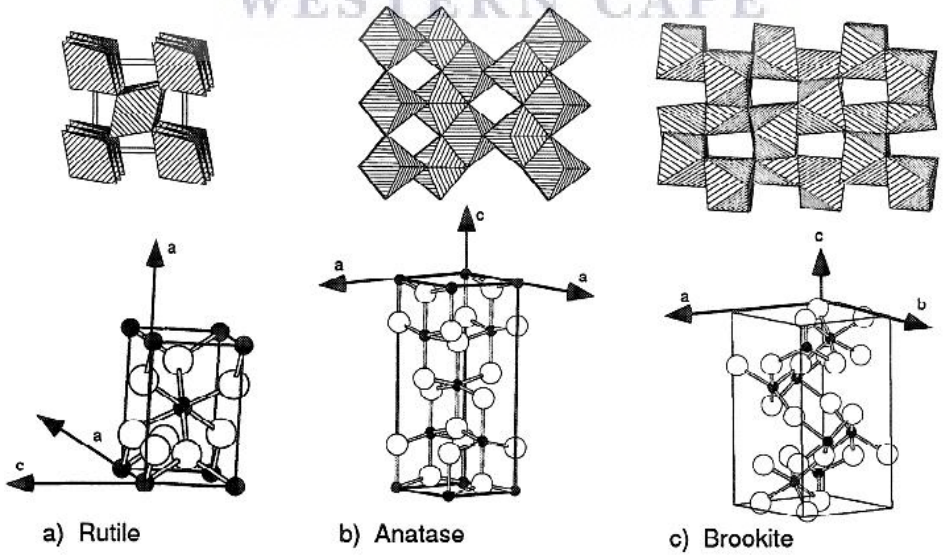

Figure 1. 14: Representation of TiO_2 Crystal structures [1.45].

As shown in Figure 1.15, the anatase phase of TiO_2 can be obtained at temperatures below 600°C. It is then transformed to rutile phase above 800°C; Bakri et al. reported that the phase transition from anatase to rutile occurs at 900°C [1.42]. These three phases are characterized by lattice constants, rutile (a=4.59Å, c=2.96Å), anatase (a=5.36Å, c=9.53Å) and brookite (a=9.15Å, b=5.44Å, c=5.14Å). Amongst the three forms, there is not much of a difference in terms of refractive index which is 2.61, 2.56 and 2.58 for rutile, anatase and brookite, respectively [1.44, 1.45].

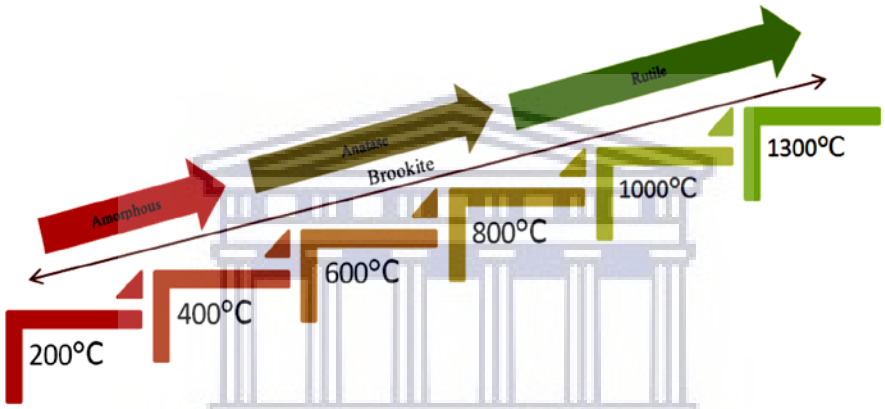

Figure 1. 15: Crystal structure with respect to the annealing temperature [1.43].

The mobility of TiO_2 lies within the range of 20 to 10^{-6} $cm^2V^{-1}s^{-1}$ depending on the structure [1.47]. The anatase phase of TiO_2 with a band gap of 3.2 eV is well known for its use as a photocatalyst due to its relatively low cost, non-toxicity and high chemical stability. UV light with a wavelength shorter than 400 nm can excite an electron from the VB to the CB and create an exciton. When the photogenerated electrons interact with molecular oxygen (O_2), superoxide radical anions ($•O_2$-) are then produced; photogenerated holes reacts with water resulting in hydroxyl (•OH) radicals. These two reactive radicals act together to decompose organic compounds. The longer exposure time to UV light means more of the organic material will be decomposed. This implies that even an oily stain would gradually disappear when exposed to UV light [1.46].

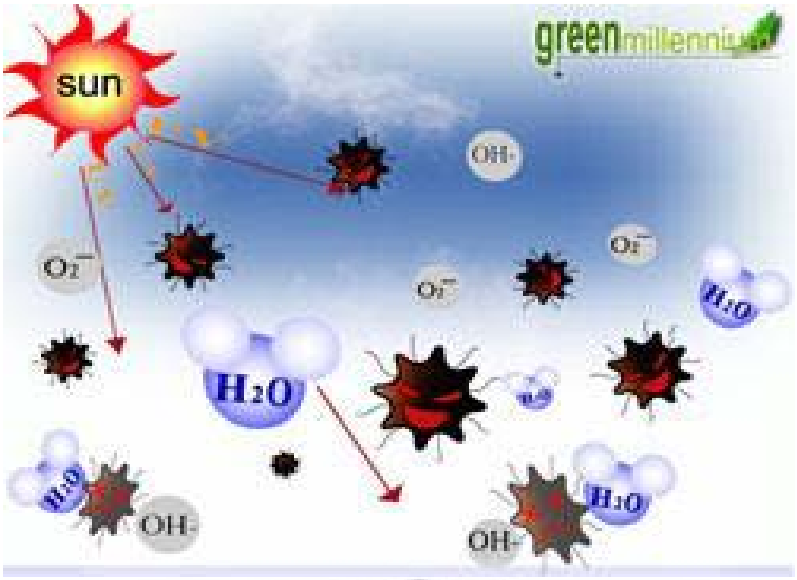

Figure 1. 16: Photocatalytic action of TiO_2 [1.46].

1.6.3 Zinc Oxide (ZnO) as an electron transport layer (ETL)

ZnO in its mineral form is known as zincite. ZnO is a member of II-IV compound semiconductor material. ZnO crystallizes mainly in two structures: either the hexagonal wurtzite, cubic rock salt or cubic zinc blend. These crystal structures shared by ZnO are schematically shown in Figure 1.17. The thermodynamically stable phase at room temperature is wurtzite. The zinc blende structure can only be stabilized by the growth of a cubic structure, while the rock salt (NaCl) structure can be obtained at relatively high pressure. The ZnO hexagonal wurtzite structure has lattice parameters a = 3.25 Å and c = 5.19 Å with a c/a ratio of 1.602, which is close to 1.633 for an ideal hexagonal closed-packed structure. The zinc atoms are tetrahedrally coordinated to four oxygen atoms. The tetrahedral points are in the same direction along the hexagonal axis and this gives the crystal its polar symmetry [1.48, 1.49, 1.51].

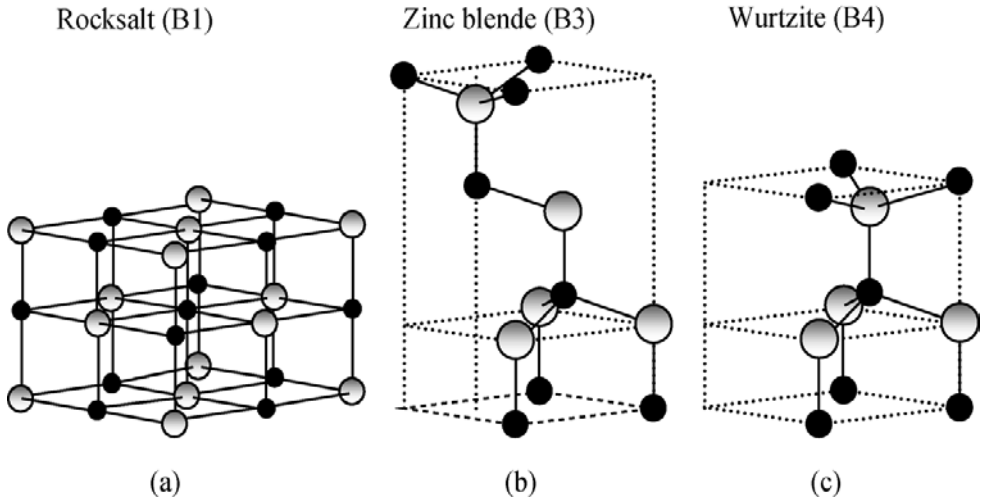

Figure 1. 17: Stick and ball representation of the ZnO crystal structures (a) cubic rock salt (B1), (b) cubic zinc blende (B3), and (c) hexagonal wurtzite (B4). Shaded grey spheres (Zn atoms) and black spheres (O atoms) [1.48].

ZnO has a direct and wide band gap of 3.44 eV at low temperatures and 3.37 eV at room temperature; it also has a large exciton binding energy of 60 meV allowing for efficient UV stimulated emission. This makes ZnO a promising material that exhibits UV attenuation characteristics blocking 95% of all UV radiation. It also exhibits excellent transparency in the long wavelength region and shows strong luminescence in the green-visble wavelength region of the spectrum, with an emission peak at 495 nm and half-width of 0.4 eV [1.53-1.55]. The importance of ZnO, among other metal oxides, is increasing due to many applications, such as transistors, optical waveguides, solar cells, ultraviolet detectors and gas sensing [1.56-1.58]. Thin films of zinc oxide combine interesting properties like excellent substrate adherence, radiation hardness which is good for high altitude application, and large piezoelectric behaviour [1.54]. ZnO also has good electrical properties, a wide range of resistivity (10^{-4} -10^{12} V.cm), high electron Hall mobility (200 cm^2. V. s^{-1}) and it is highly transparent at room temperature. It also has high thermal conductivity for the removal of heat during device operation [1.56]. Moreover, ZnO is a very cheap and stable material that is abundant and non-toxic. Various processing techniques have been used to fabricate ZnO thin films such as physical vapour deposition

(PVD) [1.57], spray pyrolysis [1.58], thermal evaporation [1.59] and the sol-gel technique [1.52]. Amongst the various techniques the sol-gel spin coating method provides a simple, low cost and large area thin film coating. The sol-gel process also provided the ability to optimise thin films and produce a uniform film thickness [60,61].

1.6.4 Poly(3-hexylthiophene) P3HT

P3HT is a conjugated polymer; organic macromolecules characterized by a backbone chain of alternating double- and single bonds. These conjugated polymers possess overlapping p-orbitals which enables useful optical and electronic properties. They originate from polythiophene which is a monomer structure, as depicted in Figure 1.18. P3HT is built-up from asymmetric monomers which can couple since the thiophene is a 5-membered ring that is polymerised at the 2- and 5-positions; substitution leads to directionality in the polymer which brings about regioregularity [1.62]. This coupling results in efficient packing and higher crystallinity. It is a commonly used polymer in OSCs and acts as the light-absorbing and electron donor material. P3HT is a low band gap polymer absorbing light of wavelength corresponding to the band gap energy of 1.8 – 2.0 eV, providing an improved overlap of the absorption spectrum and the solar spectrum, potentially absorbing more photons that may lead to making P3HT capable of improving the current as well as enhancing the efficiency of OPVs. The absorption of P3HT that overlaps with the solar spectrum depends on its molecular weight, thus by increasing the molecular weight the maximum absorption wavelength will also increase and this will result in a broader absorption spectrum of up to 600 nm. Regioregular P3HT exhibits increased absorption whereby regioregularities of head-to-tail (HT) couplings are usually obtained in excess of 90%. In highly regioregular P3HT, the majority charge carriers which are holes exhibit high field-effect mobilities of up to 0.1 $cm^2V^{-1}s^{-1}$; directly correlated to the microcrystalline

microstructure [1.62-1.64]. The regularity of P3HT is thus of great importance to achieve a higher efficiency of OPV devices.

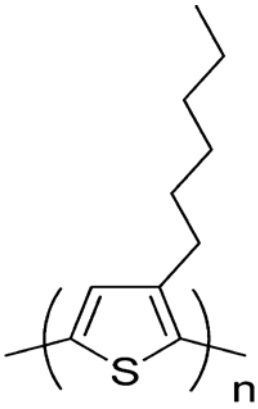

Figure 1. 18: Structural representation of P3HT [1.62].

1.6.5 Phenyl-C61-butyric acid methyl ester (PCBM)

PCBM, shown in Figure 1.19 is a derivative of a fullerene based molecule that is commonly used as an electron acceptor and transporting material in organic solar cells due to its solubility and other properties inherent to all fullerenes. Fullerenes are very high electron affinity molecules owing to their high energy LUMO of 4.4 eV. The electron mobility in the PCBM is between 2×10^{-3} and 2×10^{-2} cm^2/ Vs, while the hole mobility is negligibly small. All these fundamental properties contribute positively to the choice of using PCBM as an acceptor material [1.64, 1.65].

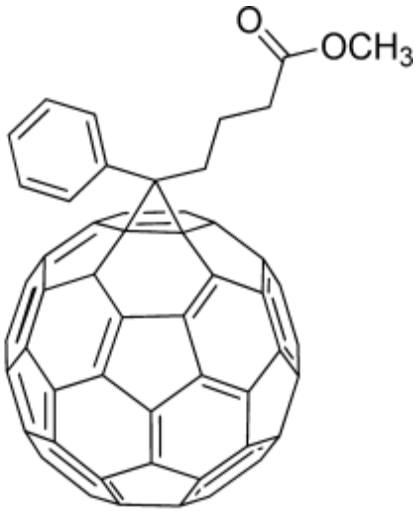

Figure 1. 19: Structural representation of PCBM [1.62].

Newer alternatives for replacing the active material blend of P3HT:PCBM are used nowadays, but ours study is not about the development of new active materials, but about the need to develop our lab workable devices. Once this is achieved, we can move on to newer and better materials.

1.7 Aims and outline of the study

OSCs are very promising organic-based devices for low-cost solar conversion, compatible with solution process methods such as spin coating and roll to roll or printing, for mass production. However, many issues still need to be addressed. The performance of OSCs is constrained by the limited light absorption, and poor stability under ambient conditions. Apart from this, high charge collection efficiency at the electrode interface is also critical for the device performance. One way to overcome these issues is to implement the so-called inverted OSC, a device structure in which the charge collection is reverted in comparison with the conventional structure; it thus allows for the HWF top metal electrode, like silver and gold, to avoid fast oxidation and degradation. The inverted geometry can also eliminate the use of acidic PEDOT:PSS on ITO as a hole transport layer. The use of a metal oxide interlayer between the organic active layer and the electrodes can thus potentially improve the cell performance. In addition, the surface of

the metal oxide layer can be modified to facilitate enhanced charge collection.

In this thesis, the objective of the study is to optimise the solution processing of metal oxide (ZnO, TiO_2 and MoO_3) nanocrystalline thin films for use in an organic/ hybrid solar cell. These metal oxides will act as ETLs and HTLs. The optimisation of these metal oxides will be in terms of the concentration of the solution and the thickness of the thin films. By making use of the sol-gel process and thermal evaporation method (in cases where sol-gel processing fails to deliver a feasible thin film), metal oxide thin films will be synthesised. The fully optimised metal oxide layers will be combined with the active layers of P3HT and PCBM and will be used in the manufacturing of inverted hybrid organic solar cells. Finally, the effectiveness of the metal oxide/ organic active layer interface will be studied for enhanced performance in the inverted OSCs.

Chapter one of this study introduces information on the energy status and how photovoltaics has developed over the decades as potential renewable energy technology in order to assist in preventing the depletion of our coal resources and to aid in reducing greenhouse gas emission. An overview of the photovoltaic technologies that have been explored over the decades is also given, together with a brief process of the mechanisms of device fabrication and characterization. In addition, the basic properties of the materials employed in the manufacturing of the organic hybrid OSC are reviewed, followed by the objectives of this researched work.

Chapter two focusses on the description of the deposition methods that were used in this study. More specifically the solution-processed spin coating and thermal evaporation is covered. This chapter also discusses the analytical techniques used to characterise the fabricated thin films as well as the solar cells.

Chapter three introduces a review of the ZnO ETL. In addition, it will describe the experimental detail and processes. This is followed by the results and discussion on the surface morphology, structural, chemical and optical properties of the prepared ZnO thin films obtained during the optimisation of this study.

Chapter four introduces background information of the oxide layer TiO_2. In addition, we deal with the experimental detail and processes to produce the TiO_2 thin films similar to that of the ZnO thin film. This is followed by a discussion of the results on the surface morphology, structural, chemical and optical properties of the prepared TiO_2 thin films which are used as ETLs.

Chapter five finally describes the inverted geometry of the OSC and demonstrates how the ZnO and TiO_2 thin films can be used as buffer layers and be incorporated in the inverted OSC device. We also describe the preparation and fabrication of the inverted OSC devices; including substrate cleaning, thin film deposition by spin coating and thermal evaporation. This is followed by lamella preparation in order to inform discussion of the results on the morphology of the layers and the I-V characteristics of the inverted OSCs.

Chapter six gives an account of the summary and conclusion of the major findings in this researched work. Finally, the outlook of possible future work to improve device performance is recommended.

References

[1.1] Kusumawati, Y., 2015. Oxide and composite electron transport layers for efficient dye-sensitized solar cells. *Inorganic chemistry*. Doctoral dissertation, Sorbonne University Pierre and Marie Curie-Paris.

[1.2] Afonso, T.L., Marques, A.C. and Fuinhas, J.A., 2017. Strategies to make renewable energy sources compatible with economic growth. *Energy strategy reviews*, *18*, pp.121-126.

[1.3] Shafiee, S. and Topal, E., 2010. An overview of global gold market and gold price forecasting. Resources Policy, 35(3), pp.178-189.

[1.4] Tsai, S.B., Xue, Y., Zhang, J., Chen, Q., Liu, Y., Zhou, J. and Dong, W., 2017. Models for forecasting growth trends in renewable energy. Renewable and Sustainable Energy Reviews, 77, pp.1169-1178.

[1.5] Karaköse, E. and Çolak, H., 2017. Effect of substrate temperature on the structural properties of ZnO nanorods. Energy, 141, pp.50-55.

[1.6] Walwyn, D.R. and Brent, A.C., 2015. Renewable energy gathers steam in South Africa. Renewable and Sustainable Energy Reviews, 41, pp.390-401.

[1.7] Aliyu, A.K., Modu, B. and Tan, C.W., 2018. A review of renewable energy development in Africa: A focus in South Africa, Egypt and Nigeria. Renewable and Sustainable Energy Reviews, 81, pp.2502-2518.

[1.8] Kabir, E., Kumar, P., Kumar, S., Adelodun, A.A. and Kim, K.H., 2018. Solar energy: Potential and future prospects. Renewable and Sustainable Energy Reviews, 82, pp.894-900.

[1.9] Amin, N., Shahahmadi, S.A., Chelvanathan, P., Rahman, K.S., Hossain, M.I. and Akhtaruzzaman, M.D., 2017. Solar Photovoltaic Technologies: From Inception Toward the Most Reliable Energy Resource. In Encyclopedia of Sustainable Technologies (pp. 11-26). Elsevier.

[1.10] Markvart, T. and Bogus, K. eds., 2000. Solar electricity (Vol. 6). John Wiley & Sons.

[1.11] Nelson, J., 2003. The physics of solar cells. World Scientific Publishing Company.

[1.12] Saga, T., 2010. Advances in crystalline silicon solar cell technology for industrial mass production. Asia materials, 2(3), pp.96.

[1.13] Sampaio, P.G.V. and González, M.O.A., 2017. Photovoltaic solar energy: Conceptual framework. Renewable and Sustainable Energy Reviews, 74, pp.590-601.

[1.14] Kouhnavard M, Ikeda S, Ludin N A, Ahmad Khairudin N B, Ghaffari B V., Mat-Teridi M A, Ibrahim M A, Sepeai S and Sopian K 2014 A review of semiconductor materials as sensitizers for quantum dot sensitized solar cells Renew. Sustain. Energy Rev. 37 397–407

[1.15] Brown, G.F. and Wu, J., 2009. Third generation photovoltaics. Laser & Photonics Reviews, 3(4), pp.394-405.

[1.16] Bagnall, D.M. and Boreland, M., 2008. Photovoltaic technologies. Energy Policy, 36(12), pp.4390-4396.

[1.17] Gevorgyan, S.A., 2002. Production, Characterization and Stability of Organic Solar. Science, 295, pp.2425-2427.

[1.18] National Center for Photovoltaics (NCPV). "Best research-cells efficiencies, http://www.nrel.gov/pv/assets/images/efficiency-chart.png, 2017, [National Renewable Energy Laboratory (NREL)].

[1.19] Gevorgyan, S., 2010. Production, characterization and stability of organic solar cell devices. Riso National Laboratory for Sustainable Energy.

[1.20] Qi, J., Chen, J., Meng, W., Wu, X., Liu, C., Yue, W. and Wang, M., 2016. Recent advances in hybrid solar cells based on metal oxide nanostructures. Synthetic Metals, 222, pp.42-65.

[1.21] Günes, S. and Sariciftci, N.S., 2008. Hybrid solar cells. Inorganica Chimica Acta, 361(3), pp.581-588.

[1.22] He, M., Qiu, F. and Lin, Z., 2013. Toward high-performance organic–inorganic hybrid solar cells: bringing conjugated polymers and inorganic nanocrystals in close contact. The journal of physical chemistry letters, 4(11), pp.1788-1796.

[1.23] Jeng L, 2015. Materials Development and Interface Studies of Inverted Organic Solar Cells. PhD Thesis. National University of Singapore.

[1.24] Zhang, F., Xu, X., Tang, W., Zhang, J., Zhuo, Z., Wang, J., Wang, J., Xu, Z. and Wang, Y., 2011. Recent development of the inverted

configuration of organic solar cells. Solar Energy Materials and Solar Cells, 95(7), pp.1785-1799.

[1.25] Lattante, S., 2014. Electron and hole transport layers: their use in inverted bulk heterojunction polymer solar cells. Electronics, 3(1), pp.132-164.

[1.26] Morvillo, P., Diana, R., Nenna, G., Bobeico, E., Ricciardi, R. and Minarini, C., 2016. High performance inverted polymer solar cells with solution processed metal oxides as electron transport layers: A comparative study. Thin Solid Films, 617, pp.126-132.

[1.27] Banerjee, S., Gupta, S.K., Singh, A. and Garg, A., 2016. Buffer layers in inverted organic solar cells and their impact on the interface and device characteristics: An experimental and modelling analysis. Organic Electronics, 37, pp.228-238.

[1.28] Lattante, S., 2014. Electron and Hole Transport Layers: Their Use in Inverted Bulk Heterojunction Polymer Solar Cells. Electronics 3 132–64.

[1.29] Zimmermann, B., Würfel, U. and Niggemann, M., 2009. Longterm stability of efficient inverted P3HT: PCBM solar cells. Solar Energy Materials and Solar Cells, 93(4), pp.491-496.

[1.30] Gevorgyan, S., 2010. Production, Characterization and Stability of Organic Solar Cell Devices. National Laboratory for Sustainable Energy.

[1.31] Spanggaard, H. and Krebs, F.C., 2004. A brief history of the development of organic and polymeric photovoltaics. Solar Energy Materials and Solar Cells, 83(2-3), pp.125-146.

[1.32] Benanti, T.L. and Venkataraman, D., 2006. Organic solar cells: An overview focusing on active layer morphology. Photosynthesis Research, 87(1), pp.73-81.

[1.33] Bedeloglu, A., 2011. Progress in organic photovoltaic fibres research. In Solar Cells-New Aspects and Solutions. IntechOpen. New Asp. Solut. 255–86.

[1.34] Winder, C. and Sariciftci, N.S., 2004. Low bandgap polymers for photon harvesting in bulk heterojunction solar cells. Journal of Materials Chemistry, 14(7), pp.1077-1086.

[1.35] Potscavage, W.J. Jr., 2011, Physics and engineering of organic solar cells. PhD. Dissertation, Georgia Institute of Technology, Georgia.

[1.36] Derbal-Habak H., Simon J. J., Pasquinelli M., Boundia O., Hocine D., Belkaid, M. S and Chibane L., 2017. Development of Molybdenum trioxide (MoO_3) by spin coating method for photovoltaic application. Renew. Energy Power Qual. J. 1805–8.

[1.37] Meyer, J. and Kahn, A.L., 2011. Electronic structure of molybdenum-oxide films and associated charge injection mechanisms in organic devices. Journal of Photonics for Energy, 1(1), p.011109.

[1.38] Balendhran, S., 2013. Devices and systems based on two dimensional MoO_3 and MoS_2.

[1.39] Minoru I., Kousuke H. and Shuji O., 2001. Optical properties and electronic structures of layered MoO_3 single crystals. J. Phys. Condens. Matter 13 6853.

[1.40] Rao M. C., Ravindranadh K., Kasturi A. and Shekhawat M. S., 2013. Structural Stoichiometry and Phase Transitions of MoO_3 Thin Films for Solid State Micro batteries. *Res. J. Recent Sci. Res. J. Recent Sci* **2** 67–73.

[1.41] Bedikyan, L., Zakhariev, S. and Zakharieva, M., 2013. Titanium dioxide thin films: preparation and optical properties. Journal of Chemical Technology and Metallurgy, 48(6), pp.555-558.

[1.42] Noorfaizol Bin Mohamad Noor, Fabrication of titanium dioxide (TiO_2) by high-temperature oxidation of physical vapour deposition (PVD) titanium film *Eng. Mater*. 1–47

[1.43] Bakri, A.S., Sahdan, M.Z., Adriyanto, F., Raship, N.A., Said, N.D.M., Abdullah, S.A. and Rahim, M.S., 2017, January. Effect of annealing temperature of titanium dioxide thin films on structural and electrical properties. In *AIP conference proceedings* (Vol. 1788, No. 1, p. 030030). AIP Publishing.

[1.44] El-Salam, F.A., Mostafa, M.M., El-Nahass, M.M., Nada, R.H., El Zaidia, E.F.M. and Mohamed, H.S., 2015. Influence of annealing on structural and Micro-Hardness of nanocrystalline TiO_2 Thin Films. *International Journal of Scientific & Engineering Research*.

[1.45] Nakaruk, A., 2010. Synthesis and Characterisation of Titania Thin Films. *Materials Science and Engineering Faculty of Science University of New South Wales.*

[1.46] Theivasanthi, T. and Alagar, M., 2013. Titanium dioxide (TiO_2) nanoparticles XRD analyses: an insight. *arXiv preprint arXiv:1307.1091*.

[1.47] Sun, H., 2012. *Metal oxide layer in organic solar cells*. PhD, Ludwig Maximilian University of Munich.

[1.48] Morkoç, H. and Özgür, Ü., 2008. *Zinc oxide: fundamentals, materials and device technology*. John Wiley & Son.

[1.49] Bhachu, D., 2013. *The synthesis and characterisation of metal oxide thin films.* PhD. University College London.

[1.50] Janotti, A. and Van de Walle, C.G., 2009. Fundamentals of zinc oxide as a semiconductor. *Reports on progress in physics*, *72*(12), p.126501.

[1.51] Ozkendir, O.M., Yildirimcan, S., Yuzer, A. and Ocakoglu, K., 2016. Crystal and electronic structure study of Mn doped wurtzite ZnO nanoparticles. *Progress in Natural Science: Materials International*, *26*(4), pp.347-353.

[1.52] Vimalkumar, T.V., 2011. Highly conductive and transparent ZnO thin film using Chemical Spray Pyrolysis technique effect of doping and deposition parameters.

[1.53] Farooq, A. and Kamran, M., 2012. Effect of sol concentration on structural and optical behaviour of ZnO thin films prepared by sol-gel spin coating. *International Journal of Applied Physics and Mathematics*, *2*(6), p.430.

[1.54] Geetha, N., Sivaranjani, S., Ayeshamariam, A., Suthan Kissinger, J., Valan Arasu, M. and Jayachandran, M., 2016. ZnO doped oxide materials: Mini review. *Fluid Mech. Open Access*, *3*, p.141.

[1.55] Tabatabaei, M.R. and Ardekani, A.V., 2014. Physical and Electrical Characterization of ZnO Thin Films Prepared by Sol-Gel Method. *World Academy of Science, Engineering and Technology, International Journal of Chemical, Molecular, Nuclear, Materials and Metallurgical Engineering*, *8*(5), pp.458-463.

[1.56] Ali, M.M. and Meshari, S.M., 2014. Structural and Optical Characterization of ZnO Thin Films by Sol-gel technique. *Journal of Basrah Researches (Sciences)*, *40*(1A), pp.39-48.

[1.57] Jimenez-Cadena, G., Comini, E., Ferroni, M., Vomiero, A. and Sberveglieri, G., 2010. Synthesis of different ZnO nanostructures by a modified PVD process and potential use for dye-sensitized solar cells. *Materials Chemistry and Physics*, *124*(1), pp.694-698.

[1.58] Andrade, E. and Miki-Yoshida, M., 1999. Growth, structure and optical characterization of high-quality ZnO thin films obtained by spray pyrolysis. *Thin Solid Films*, *350*(1-2), pp.192-202.

[1.59] Bouhssira, N., Abed, S., Tomasella, E., Cellier, J., Mosbah, A., Aida, M.S. and Jacquet, M., 2006. Influence of annealing temperature on the properties of ZnO thin films deposited by thermal evaporation. *Applied Surface Science*, *252*(15), pp.5594-5597.

[1.60] Tsay, C.Y., Fan, K.S., Wang, Y.W., Chang, C.J., Tseng, Y.K. and Lin, C.K., 2010. Transparent semiconductor zinc oxide thin films deposited on glass substrates by sol-gel process. *Ceramics International*, *36*(6), pp.1791-1795.

[1.61] Dahnoun, M., Attaf, A., Saidi, H., Yahia, A. and Khelifi, C., 2017. Structural, optical and electrical properties of zinc oxide thin films deposited by sol-gel spin coating technique. *Optik*, *134*, pp.53-59.

[1.62] Dang, M.T., Hirsch, L., Wantz, G. and Wuest, J.D., 2013. Controlling the morphology and performance of bulk heterojunctions in solar cells. Lessons learned from the benchmark poly (3-hexylthiophene):[6, 6]-phenyl-C61-butyric acid methyl ester system. *Chemical Reviews*, *113*(5), pp.3734-3765.

[1.63] Sharma, T., Singhal, R., Vishnoi, R., Sharma, P., Patra, A., Chand, S., Lakshmi, G.B.V.S. and Biswas, S.K., 2016. Electronic excitation induced modifications of optical and morphological properties of PCBM thin films. Nuclear Instruments and Methods in Physics Research Section B: Beam Interactions with Materials and Atoms, 379, pp.176-180.

[1.64] Brown, P.J., Sirringhaus, H., Harrison, M., Shkunov, M. and Friend, R.H., 2001. Optical spectroscopy of field-induced charge in self-organized high mobility poly (3-hexylthiophene). *Physical Review B*, *63*(12), p.125204.

[1.65] Veldman, D., Meskers, S.C. and Janssen, R.A., 2009. The energy of charge-transfer states in electron donor-acceptor blends: insight into the energy losses in organic solar cells. *Advanced Functional Materials*, *19*(12), pp.1939-1948.

CHAPTER TWO

2 Deposition Methods and Analytical Techniques

2.1 Introduction

In this chapter, an overview will be given of the deposition techniques used in this study to produce ZnO and TiO_2 thin films and to construct inverted OSCs incorporating both of these as buffer layers. Section 2.2 gives the background of the spin coating technique that was used to produce solution-processed thin films under specific experimental conditions. Section 2.3 covers the thermal evaporation technique that was used to deposit the electrode in the final step of the manufacturing process of the lab-scale OSC.

The preparation methods for the thin films are described in the results chapters reserved for each ZnO and TiO_2 thin films respectively. However, the different analytical techniques required to extract the relevant information such as the surface, structural and optical properties of the above-mentioned materials and the manufactured solar cells will be described in section 2.4. Table 2.1 presents the different characterization techniques and the information obtained from each.

Table 2. 1: Analytical techniques used for characterization.

Technique	**Information obtained**
X-ray diffraction (XRD)	Crystallinity, grain size and orientation
High-resolution transmission electron microscopy (HR-TEM)	Morphology of the device
High-resolution scanning electron microscopy (HR-SEM)	Morphology, topography and chemical of individual thin films
Dektak Profilometry	The thickness of thin films
Fourier transform infrared (FTIR) spectroscopy	Chemical bonding
Ultraviolet-visible (UV-Vis) spectroscopy	Optical properties of thin films
Current - Voltage (I-V) measurements	Electrical characterization of devices

2.2 Deposition methods

2.2.1 Spin coating

2.2.1.1 Introduction

An Ossila spin coater was used for the deposition of solution-processed ZnO, TiO_2, P3HT: PCBM and MoO_x thin films. The Osilla spin coater comes with an innovative chuck that does not require a vacuum; substrates are held in place by a hollow square in the chuck. The spin coater is a multi-

function system with spin speeds range from 120 - 6000 rpm, covering different spin coating conditions. Moreover, it contains an inbuilt control system which allows for 10 recipes with up to 50 steps [2.1]. Spin coating is a procedure that has been used for several decades to deposit uniform thin films of materials onto substrates [2.2]. A typical process of spin coating involves depositing a small amount of solution onto the centre of the substrate and utilizing the centrifugal force to spread the solution evenly and leave a thin film ranging from a few nanometres to hundreds of micrometres in thickness. The homogeneity and thickness of the thin films depends on factors like the viscosity and concentration of the solution, type of solvent used, evaporation and drying rate. The thickness of the thin film is also dependent on the angular speed and the interaction between the coating material and the substrate [2.2-2.4]. Due to several advantages namely the simplicity and relatively low manufacturing cost, repeatability and its ability to quickly and easily produce very uniform thin films, easy control and handling of chemicals and substrates the spin coating method is frequently used in photovoltaic research [2.2, 2.3].

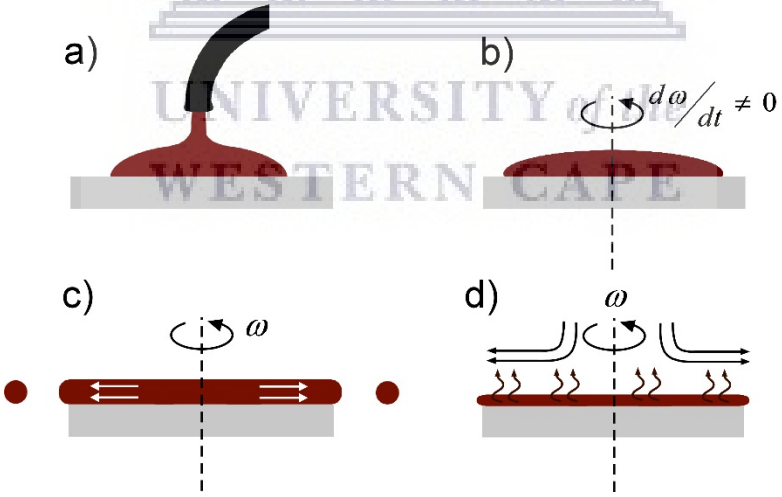

Figure 2. 1: Stages of the spin coating process to fabricate thin films [2.4].

The spin coating process consists of depositing a small amount of coating material onto the surface of the substrate. The solution is then evenly spread onto the substrate by utilizing the centripetal force. The substrate is then continuously rotated while the solution spins off the edges of the substrate

and the solvent evaporates to achieve a desired thickness of the film. The simple process can be divided into distinct stages, as shown in Figure 2.1.

The first stage is depositing the coating material onto the surface of the substrate, as in Figure 2.1 (a). Two methods of deposition are commonly used, static dispense or dynamic dispense. Static dispense is usually used to spread the coating material on the entire sample before starting the spin process-to ensure complete substrate coverage. Dynamic dispense is commonly used to deposit the coating material while the substrate is rotating at low speeds of about 500 rpm. This method allows for better coverage of the coating material on the substrate as well as reducing waste of source material since not much of it is required to wet and cover the entire surface of the substrate. Dynamic dispense is also used when the coating material or substrate has poor wetting abilities.

In the next stage of spin coating the substrate is rotationally accelerated, depicted in Figure 2.1 (b), to its desired speed while expulsing some of the coating material from the substrate, as shown in Figure 2.1 (c). Note that spiral vortices might present themselves due to the initial depth of the fluid on the substrate. They might form as the acceleration of the substrate provides a twisting motion attributed to the inertia of the fluid. During this stage the excess of fluid is expelled under rotational motion and the fluid becomes thin enough to be completely co-rotating with the substrate. Ultimately, the coating material is thin enough that the shear drag equals the rotational acceleration [2.2, 2.4].

The final stage of the spin coating process is the evaporation process, as shown in Figure 2.1 (d). During this stage, further fluid thinning occurs while the solvent is drying due to airflow leaving behind the desired material on the substrate in an even coverage, forming a thin film [2.4]. The drying rate of the fluid depends on the number of factors including solvent volatility, air temperature and humidity around the coated substrate [2.4].

Post deposition annealing is used to further evaporate the excess solvent and evoke structural and physical changes to the thin films.

2.2.2 Thermal evaporation

The MoO_x thin film and Ag back contact were deposited in the Vacutec-designed multi-chamber high vacuum deposition system in the CADAR lab at the University of the Western Cape. It is an interconnected five-chamber system allowing for transport of samples during different stages of deposition. Thermal evaporation is the process whereby materials such as metal, organic materials and semiconductors are evaporated by passing a high current through the crucible containing the material inside a high vacuum chamber. For the evaporated material to be deposited directly onto the substrate, it has to be positioned several centimetres from the source. This is a useful method for depositing numerous layers of different materials without chemical interaction between the respective layers. The control of materials evaporated depends on several parameters such as vacuum chamber pressure, material purity, deposition current and evaporation rate. Specifically, the pressure of the vacuum chamber must be low enough in a range (10^{-7} – 10^{-5} mbar), otherwise the hot vaporized material particles may react with existing oxygen molecules forming an oxide [5]. The hot vapourized material can also create holes in the film due to the shadowing phenomenon, which causes features like bulges and spirals, making it difficult to coat uniformly. This can reduce contact between layers which can excessively increase the series resistance of the device and thus reduce the short circuit current. Moreover, the materials left on the wall of the chamber during depositions may contaminate future depositions. Sometimes problems with regards to the thin film thickness and uniformity may arise over large scale substrates. These problems can be addressed by varying the distance between the source material and the substrate. A second example to consider is to rotate the substrate to even out the distribution of the source.

Two principal methods for optimizing the uniformity of a thin film over large areas are to vary the geometric location of the source and rotating shutters between evaporation sources and substrates [2.6]. Moreover, the angular position of the target with respect to the source can also be varied. The overall thickness is typically measured by a crystal monitor connected to the deposition system.

2.3 Analytical techniques

2.3.1 X-ray diffraction (XRD)

2.3.1.1 Introduction

X-ray diffraction (XRD) reveals the structure, crystal orientation and spacing between the atomic planes of particles and thin films; hence it was used to verify the crystallinity as well as the orientation and size of crystallites present in ZnO, TiO_2 and MoO_x metal oxide thin films. X-rays are electromagnetic radiation with small wavelengths lying in the range of 0.5 to 2.5 Å. These x-rays are produced in an x-ray tube, a vacuum tube that maintains a high voltage to accelerate the electrons released by a hot cathode at very high velocity. These electrons collide with a metal target or the anode, resulting in x-rays. Upon collision with the target, x-rays are created by two different atomic processes [2.7]:

X-ray fluorescence: Here electrons with sufficient kinetic energy can knock an orbital electron out of the inner electron shell of an atom, and as a result an electron from higher energy levels emits an x-ray photon and then fills up the vacancy. During this process, an emission spectrum also known as spectral lines of x-ray frequencies is produced. Usually these are transitions from upper shells into the K shell (called K lines), or into the L shell (called L lines).

Bremsstrahlung: The radiation released by the electrons being scattered and rapidly deaccelerated by the strong electric field near the High-Z (proton number) nuclei produce a continuous spectrum These wavelengths are known as X-rays.

Diffraction refers to the various phenomena that occur when waves interfere with a structure whose reoccurring distance is equivalent to that of the incident wavelength. The incoming wave scatters upon interaction with the structure resulting in constructive and destructive interference. X-rays can be diffracted by three-dimensional crystalline structures since the inter-atomic spacing within these crystalline structures have a similar range of wavelengths to x-rays. Moreover, each atom in the crystalline structure serves as a scattering centre for the incident wavelengths [2.7]. This phenomenon known as x-ray diffraction (XRD) can be used to investigate the fine, crystalline structure of matter. One of the most important purposes of this study is the identification of any crystalline phases present in ZnO and TiO_2 thin films. It can also supply information on the orientation and sizes of the crystal grains of the aforementioned thin films.

2.3.1.2 Theory

2.3.1.2.1 Crystal Structure and Bravais Lattices

The atoms within some materials are arranged periodically in three dimensions, thus resulting in crystalline material. These atoms can also be randomly distributed, making the material amorphous. Figure 2.2 illustrates the atomic arrangement found in a crystal, it is best to imagine the atoms as a set of imaginary points with a fixed relation in space. This concept can be referred to as a point lattice and is defined as an array of points in space, so arranged that each point has identical surroundings [2.8].

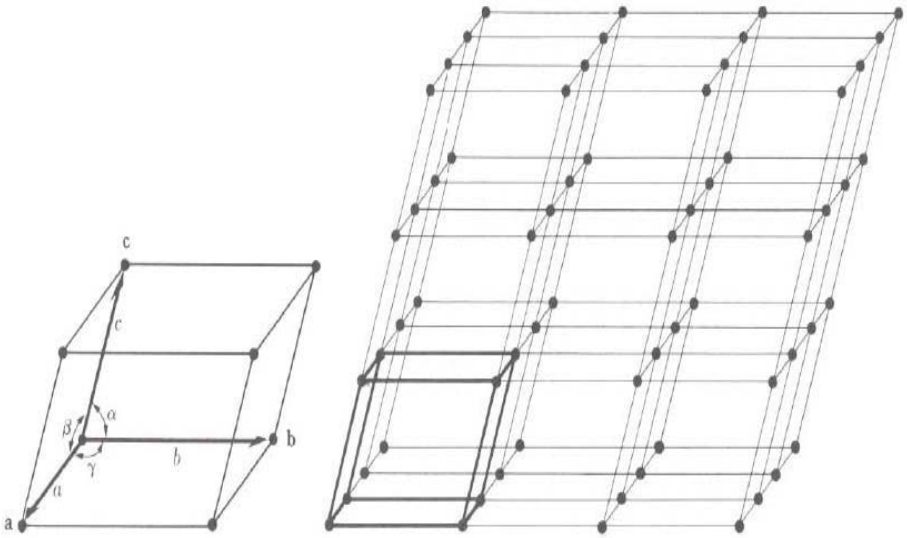

Figure 2. 2: Schematic of (a) its point lattice and (b) primitive cell and the angles between the translation vectors [2.8].

Three vectors a, b and c drawn from any lattice point produces a point lattice unit cell. These vectors are known as the crystallographic axes of the unit cell. It can also be described in terms of their lengths (a, b and c) and the angle between them (α, β and λ), known as the lattice constants or lattice parameters, as shown in Figure 2.2. The crystallographic axes also define the whole point lattice, which can be produced by repetitive translation of the vectors. There are fourteen different point or Bravais lattices, as described in Table 2.2., which are dependent on the relationship between the lattice parameters (i.e. a, b, c, α, β and λ). The direction of any vector within the Bravais lattice is given as a linear combination of the three crystallographic axes as:

$$x = ua + vb + wc, \qquad (2.1)$$

where a, b or c is any vector in the Bravais lattice and u, v and w are the coordinates of any point on the vector. Equation (2.1) can be written in short as [u v w]. However, [u v w] are always converted to a set of smallest

integers, e.g. [2 2 4] and [½½1] which represents the same direction, with [1 1 2] being the preferred notation. All of these vectors form the reciprocal space of the lattice, or reciprocal lattice.

Table 2. 2: The fourteen Bravais lattices [2.8].

	Axial length and angles	**Bravais lattice**
Cubic	Three equal axis at right angles $a = b = c$, $\alpha = \beta = \gamma = 90°$	Simple Body-centred Face-centred
Tetragonal	Three angles at right angles, two equal $a = b \neq c$, $\alpha = \beta = \gamma = 90°$	Simple Body-centred
Orthorhombic	Three unequal axes at right angles $a \neq b \neq c$, $\alpha = \beta = \gamma = 90°$	Simple Body-centred Face-centred Base-centred
Rhombohedral	Three equal axes, equally inclined $a = b = c$, $\alpha = \beta = \gamma \neq 90°$	Simple
Hexagonal	Two equal co-planar axes at 120°, third axis at right angles $a = b \neq c$, $\alpha = \beta = 90°$ $\gamma = 120°$	Simple
Monoclinic	Three unequal axes, one pair not at right angles $a \neq b \neq c$, $\alpha = \gamma = 90° \neq \beta$	Simple Base-centred
Triclinic	Three unequal axes, unequally inclined and none at right angles $a \neq b \neq c$, $\alpha \neq \beta \neq \gamma \neq 90°$	Simple

Given any Bravais lattice, a lattice plane is defined as any plane containing at least three non-collinear lattice points. A family of lattice planes is a set of parallel planes, when combined they contain all the points of the three-

dimensional Bravais lattice. For cubic systems, there is an intrinsic relationship between the family of lattice planes and the vectors in the reciprocal lattice, which provides a convenient way of specifying the orientation of the lattice planes in space.

2.3.1.2.2 Bragg's Law of Diffraction.

The basis for x-ray diffraction is described by the Bragg equation, named after Bragg who discovered that diffraction could be pictured as a reflection of the incident beam from the lattice planes. Bragg then developed a mathematical equation for the condition of reflection, which is equivalent to simultaneously solving the three Laue equations which are as follows:

$$\Delta k = 2\pi h, \quad (2.2)$$

$$\Delta k = 2\pi k, \quad (2.3)$$

and

$$\Delta k = 2\pi l \quad (2.4)$$

where (h, k, l) are Miller indices and must be integer numbers as they determine the scattering vector Δk. The vector $\Delta k = k_{out} - k_{in}$, k_{in} is the wave vector of the incoming beam, and k_{out} the wave vector of the outgoing beam. By means of mathematical derivation, a simpler and more workable expression of diffraction is provided [2.9]. A beam of parallel X-rays penetrating a stack of planes of spacing d can be considered, at a glancing angle θ as depicted in Figure 2.3. Each plane must be considered as reflecting a fraction of the incident beam [2.9].

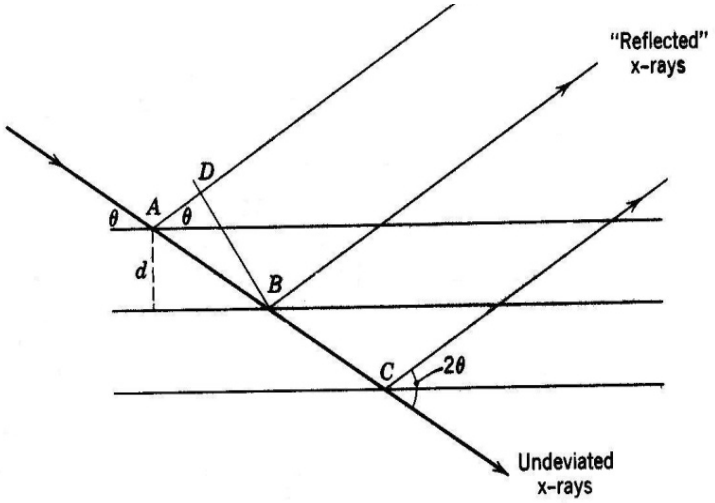

Figure 2. 3: Schematic depiction of the condition of reflection for Bragg's law [2.9].

The reflected rays combine to form a diffracted beam if they happen to be in phase by an integer number of wavelengths – that is if their path difference AB – AD = nλ, where n = 1, 2, 3.

AB and AD is given by:

$$AB = \frac{d}{\sin\theta}$$

and

$$AD = AB\cos 2\theta = \frac{d}{\sin\theta}(\cos 2\theta).$$

Therefore

$$n\lambda = \frac{d}{sin\theta} - \frac{d}{\sin\theta}(\cos 2\theta) = \frac{d}{\sin\theta}(1 - \cos 2\theta) = \frac{d}{\sin\theta}(2sin^2\theta),$$

leading to

$$n\lambda = 2dsin\theta. \qquad (2.5)$$

This is the Bragg condition for reflection [9]. Equation (2.5) gives the angle θ, at which a set of planes of spacing d constructively reflects x-radiation of wavelength λ in the nth order. The interplanar spacing d, of a set of parallel crystallographic lattice planes, is defined by the dimensions of the crystal unit cell. There exist an infinite number of such families of parallel planes in a given crystalline lattice, and each is associated with a particular Bragg angle θ, as indicated in Figure 2.3. Each set of planes is characterized by the three Miller indices hkl, and the resultant diffracted beam is termed the hkl Miller indices.

2.3.1.3 Grazing incident X-ray diffraction (GIXRD)

X-ray diffraction experiments for fairly thick films and bulk samples are generally performed in the symmetric Bragg-Brentano (BB) diffraction geometry. The BB geometry is highly penetrating (10 – 100 μm) [2.10] and is most often not useful for analysing thin thin films (nm range) because of the correspondingly low diffraction volume within the thin film that results in a very low peak-to-noise ratio and poor structural information about the film [2.11]. When an X-ray diffraction experiment is performed in an asymmetric geometry employing a low fixed grazing incidence, it is referred to as GIXRD. A schematic of the GIXRD configuration is shown in Figure 2.4 (a).

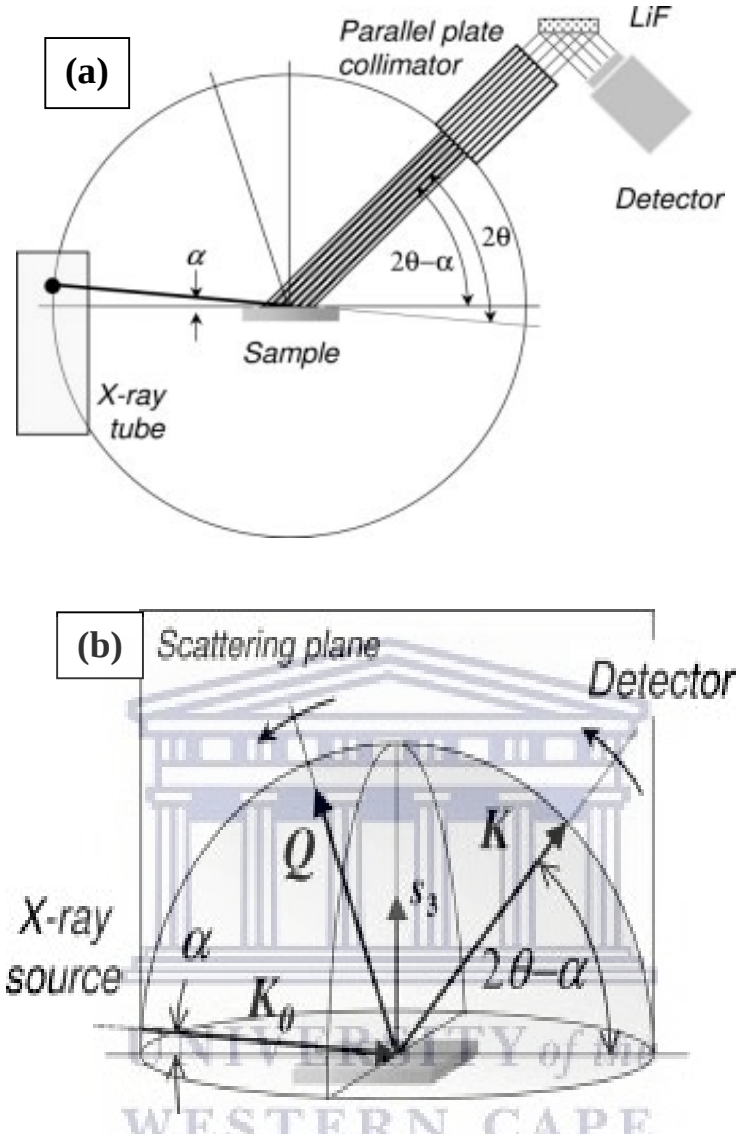

Figure 2. 4: A schematic diagram of (a) the diffractometer configuration and (b) the experimental configuration for GIXRD. [2.10].

As in the symmetric (BB) case, the configuration is still coplanar with wave vectors K_o, K and S_3 all lying in the same plane, where K_o is the incident wave vector, K is the scattered wave vector and Q the scattering wave vector. However, here the incident angle is kept fixed near the critical angle and the detector scans the 2θ circle. The crystalline planes scattering the X-rays are now the planes perpendicular to the Q vector as shown in Figure 2.4 (b). The advantage of using a low and fixed incidence angle is to limit the penetration of the X-ray beams and maximize the diffraction volume within the thin films by increasing the path length as well as foot prints of the X-

ray beam within the thin film specimen. The path length of the X-ray beam within a film of thickness t becomes l = t/sinα which can be multiple times the actual thickness of the film and the foot print (of the X-ray beam with width d) = d/sinα. The penetration depth of X-ray in a material has a linear absorption co-efficient μ given by the equation

$$\tau = \frac{\sin\alpha \sin\beta}{\mu\,(\sin\alpha + \sin\beta)}, \qquad (2.6)$$

where α, β are the incident exit angle of the X-ray respectively. The essence of this depth is that about 63 % of the diffracted beam originates from depth τ below the sample surface.

In GIXRD, the penetration depth varies strongly for values of α near the critical angle according to the above expression, but if α is not too close to the critical angle i.e., if θ_{hkl} is not in the vicinity of 0 or 90°, it can be approximated to the expression

$$\tau = \frac{\sin\alpha}{\mu}. \qquad (2.7)$$

A reliable choice of α is guided by the criteria that the average path length

$$l = \frac{1}{\mu}. \qquad (2.8)$$

2.3.1.4 Experimental set-up

X-ray diffraction (XRD) patterns were collected using a Panalytical Empyrean X-ray powder diffractometer, with reflection geometry at 2θ-values ranging from 10 – 90°, with a step size of 0.02°, operating at 45 kV and 40 mA. Monochromatic Copper (Cu) $K\alpha_1$ radiation with a wavelength of 0.154 nm was used as the X-ray source. Grazing angle x-ray diffraction

was also performed using Cu K alpha radiation, an acceleration voltage of 45 kV and a current of 40 mA with a fixed divergence slits, solar slits and Ni Cu K beta filter. A Parabolic mirror with collimator was used for grazing incidence. All XRD measurements were performed at the National Metrology Institute of South Africa (NMISA, Pretoria). The (hkl) values and the angles at which the peaks for the experimental data were observed were determined by computer software (X'Pert High Score) and compared with patterns from a data base.

2.3.2 High-resolution transmission electron microscopy (HR-TEM)

2.3.2.1 Introduction

The electron microscope utilizes an electron beam that is focused by an assembly of electromagnetic lenses, with the beam only enclosed in an evacuated column. It is an improvement of the light microscope especially as far as resolution is concerned since electrons have much shorter wavelengths (in the range of 10ths of pm depending on the accelerating voltage between the cathode and anode in the electron gun) than light, which is of the order five times longer.

2.3.2.2 Theory

2.3.2.2.1 Basic operation

A basic TEM consists of an electron gun which provides electrons, a series of electromagnetic lenses, a viewing screen coated with a layer of electron-fluorescent material, and a camera which must work in the vacuum within the microscope [2.12, 2.13]. These components are assembled into a vertical microscope column. A typical example is shown in Figure 2.5. The electron gun emits a diverging beam of electrons through the anode aperture. This beam can be deflected to be aligned parallel to the optical axis of the lens

system. The deflector coils are controlled by the gun alignment controls, and the electron beam is focused down to a fairly small spot by the first condenser lens. The setting of this lens controls the ultimate spot size attainable by the condenser system, which is generally less than 1 μm. The second condenser lens projects the beam at the specimen in such a way that the area illuminated and the convergence angle can be controlled. Below this lens is a moveable aperture that cut out any scattered beams, allowing the primary beam to give a clear diffraction image. The best resolution and image sharpness is obtained by working with the smallest condenser lens aperture (<300 μm) while exiting the second condenser lens more strongly. However, this reduces the illumination level considerably.

The condenser stigmator placed below the condenser aperture compensates for astigmatism in the illumination system. In this same region are the wobbler coils for aiding focusing and two sets of alignment coils in order to bring the beam exactly onto the optical axis in the crucial part of the microscope near the specimen. The specimen, objective aperture and objective stigmator coils are all placed inside the objective lens windings. The objective lens focuses on the specimen and forms an intermediate image at a magnification of about 50X. The objective aperture sits in the back focal plane of the objective lens and enables the operator to allow particular groups of electrons to contribute to the final image. In the plane of the first intermediate image is the selected area aperture, which allows a particular part of the image to be selected for examination and diffraction analysis. Below this aperture are three or four lenses whose function is to magnify the image or diffraction pattern and project it into the fluorescent screen. The electronics needed to control the electron gun, six or seven lenses and a vacuum system is quite complex. For this reason, there is a tendency for modern electron microscopes to be controlled by a built-in computer, which results in a reduction in the number of manual controls [2.12, 2.13].

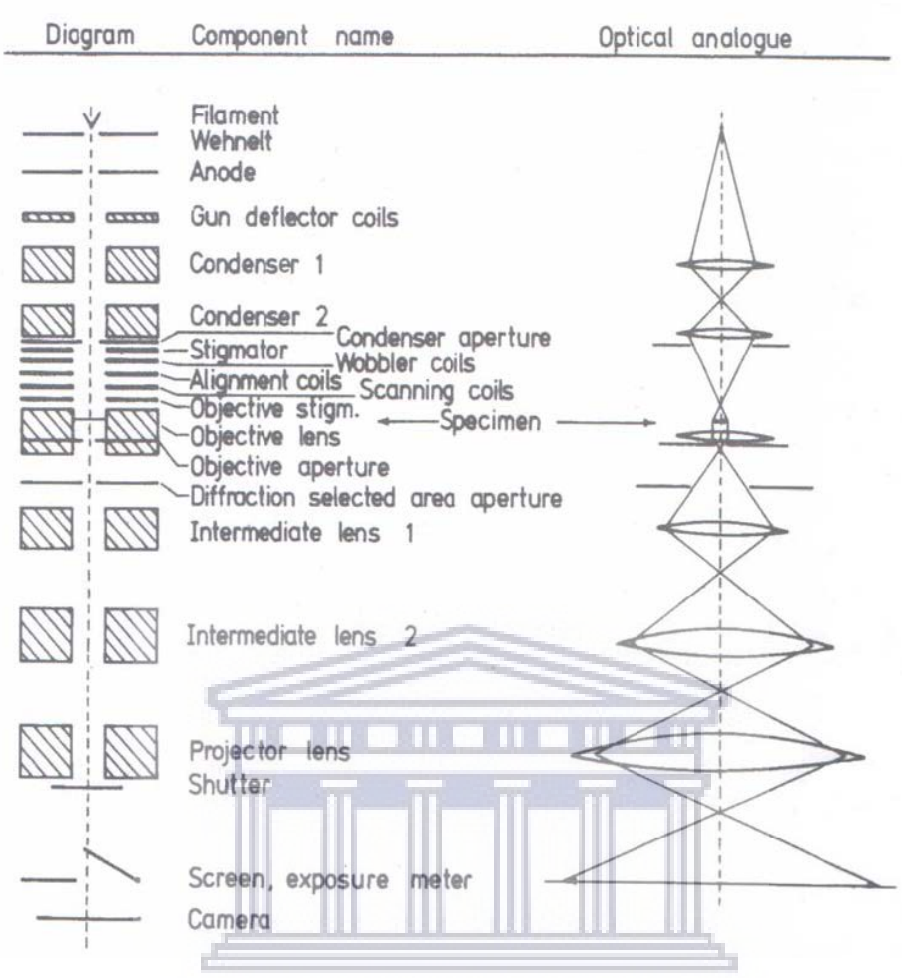

Figure 2. 5: A cross-section of the basic components of HR-TEM. The optical analogue is also provided [2.13].

2.3.2.2.2 Electron Diffraction

In all microscopes, a diffraction pattern of crystalline specimens inevitably forms in the back focal plane of the objective lens. In this plane all parallel rays leaving the specimen in a specific direction pass through a point in the diffraction pattern [2.13].

During normal imaging, the diffraction pattern is unseen because the first intermediate lens is focused on the first intermediate position in Figure 2.5, and the image is what is finally projected onto the screen. In diffraction mode the first intermediate lens diffraction mode is activated so that the projector lens displays the diffraction pattern in the back focal plane of the

objective lens and projects magnified versions of this pattern instead to the projector system. There are two fundamentally different ways of examining the diffraction pattern from a selected area of the specimen. In the selected area diffraction technique, a small area of the specimen is selected, although a larger area is being illuminated. In the alternative micro-diffraction technique, the beam is condensed into a small spot so that the diffraction pattern comes from the whole of the (small) illuminated area. In this case the diameter selected on the specimen is the same as the diameter of the beam at the specimen. This is the only way to obtain a diffraction pattern from a region smaller than 1 μm in diameter (down to a few nanometres). A diffraction pattern is obtained when the electron beam encounters crystalline material, resulting in strong preferential scattering in certain well-defined directions governed by the Bragg's Law in equation (2.10).

The Bragg condition is said to be satisfied when a crystal is orientated in such a way that the incident electron-beam satisfies the diffraction angle for the specific plane. Since most of the diffracted electrons are concentrated in these Bragg directions, a crystal grain will appear bright if the diffracted beams pass through the objective aperture and dark if stopped by the objective aperture. Thus, in a polycrystalline material some grains will appear bright and some dark, depending on their orientation with respect to the electron beam, Figure 2.6(b). Different types of diffraction patterns arise from different specimen microstructure as can be seen in Figure 2.6(a) that shows a single crystal (i.e. a specimen consisting of a single repeating array of atoms) orientated in such a way that several sets of planes are parallel to the beam. This gives rise to a diffraction pattern consisting of a regular array of bright spots. The arrangement of these spots depends upon the orientation of the atomic planes in the electron microscope. If the specimen contains several crystals of different orientations as in Figure 2.6(b), then the diffraction pattern is the sum of the individual patterns. The spots are not randomly distributed but tend to fall on rings of constant radii.

If the specimen consists of a large number of small crystallites (grains) of similar crystal structure, but at different orientations to one another (i.e. a polycrystal as in Figure 2.6 (c)) the diffraction pattern will consist of a series of sharp concentric rings. This pattern evolves from a large number of single crystal diffraction patterns, each rotated by a small amount with respect to one another. In the case of an amorphous material, the constituent atoms are arranged entirely randomly and without any distinct repeating structure. For such materials, the diffraction pattern will contain no discrete maxima. It rather consists of diffuse diffraction rings around the bright central spot of unscattered electrons [2.12, 2.13].

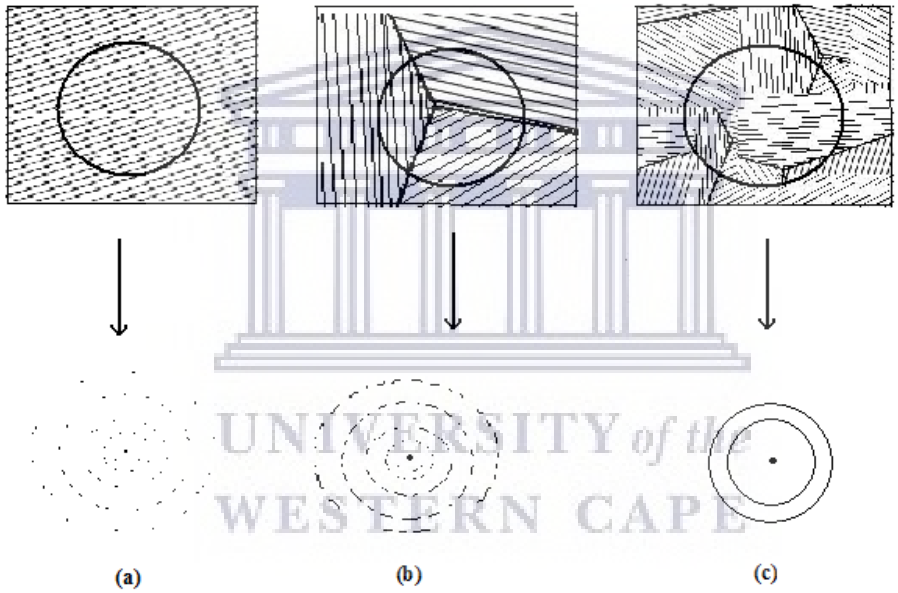

Figure 2. 6: Types of diffraction pattern which arise from different specimen microstructure: (a) A single perfect crystal, (b) A small number of grains – notice that even with three grains, spots begin to form circles, (c) A large number of randomly orientated grains, the spots have now merged into rings [2.13].

Using the standard Miller index notation to define the plane and directions in the crystal, diffraction patterns can be interpreted. Using this notation for a cubic crystal, for example, the interplaner spacing of planes of the type (hkl) is given by:

$$d_{hkl} = \frac{a}{\sqrt{h^2+k^2+l^2}}, \qquad (2.9)$$

where a is the lattice parameter of the unit cell and h, k and l the Miller indices. For first order diffraction i.e. n =1, Bragg's law reduces to:

$$\lambda = 2dsin\theta. \qquad (2.10)$$

For small angles of θ, which is typical of electron diffraction, we can write sin θ = θ, and equation (2.10) further reduces to:

$$\lambda = 2d\theta. \qquad (2.11)$$

Consider now a beam of electrons impinging on a crystalline specimen as in Figure 2.7. Some of the electrons pass through the specimen without interaction and hit the screen or film, which is a distance L from the specimen, at O. Other electrons are diffracted through an angle θ by the crystal planes of spacing d, and these electrons hit the film at A, which is a distance r from 0. From simple geometry, it can be seen that for small angles of diffraction:

$$\frac{r}{L} = 2\theta. \qquad (2.12)$$

Combining equations (2.11) and (2.12), we find:

$$rd = L\lambda, \qquad (2.13)$$

where λL is called the camera constant and is determined by analysing a known crystal. From equation (2.13) it can be seen that the distance of a diffraction spot from the undiffracted spot, r, is therefore inversely proportional to the d spacing of the diffracting planes. A table of the $\lambda L/d_{hkl}$ values for different (hkl) planes can be drawn up. By measuring r directly in

the pattern and comparing it with the values in the table, the pattern can be indexed, i.e. the respective h, k and l values can be determined [2.14].

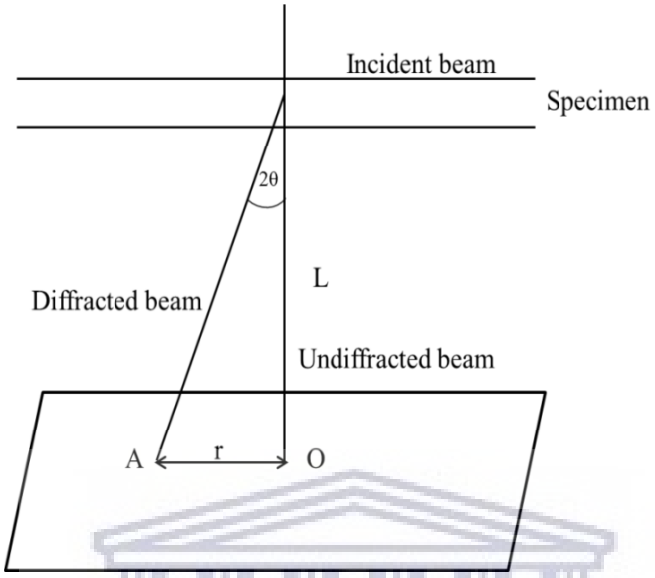

Figure 2. 7: Schematic diagram showing the geometry of diffraction pattern formation [2.12].

The HR-TEM has the edge over other conventional low-resolution transmission electron microscopes because it provides excellent analytical performance pertaining to nanoscale imaging for daily use in a multi-user environment. In addition, modern TEMs takes into account the control and displaying of matter at a scale of 1-100 nm and are operated at intermediate of 200-400kV [2.15]. The utilization of such high accelerating voltages, compared with the 1-30kV utilized in SEM and electromagnetic focal points with adjusted spherical and chromatic distortion coefficient, has improved the resolution to a fraction of a nanometre [2.16]. This allows for the operation of high-resolution TEM, resulting in an imaging tool of thin specimens; whereby the atomic planes can be probed and informative information can be extracted from the transmitted sign. Moreover, TEMs together with modern spectrometers allows for the investigation of elemental analysis by method of electron energy-loss spectroscopy (EELS) as well as investigating the chemical bonding nature utilizing electron energy-loss near edge structure (ELNES) at the nanometre scale. The

precedence of EELS can be ascribed to the fact that the technique can be utilized for the identification of light elements, which are not easily detected by customary examination during EDS. Additional information, for example, the crystal structure and fine structure can be acquired by operating the TEM in selected-area electron diffraction (SAED) mode and by performing EELS imaging combined with scanning TEM (STEM-EELS), respectively [2.16].

2.3.2.3 Experimental set-up

The Focussed Ion beam lamella sample of the prepared device was investigated using an FEI Tecnai G2 20 field-emission gun (FEG) HR-TEM, operated in bright field mode at an accelerating voltage of 200 kV, located at the University of Western Cape (UWC) in the Electron Microscope Unit (EMU).

2.3.3 High-resolution scanning electron microscopy (HR-SEM)

2.3.3.1 Introduction

The SEM is a characterisation tool used to study the surface or near surface structures of samples. This technique is widely utilised in many research fields where the investigation of smaller materials; typically, at the micrometre scale, requires high magnification imaging. The utilization of electrons as a light source in SEM allows for imaging at relatively high magnifications at resolution typically between 1 and 10 nm. The high quality three-dimensional images obtained from SEM can be used to extract useful information at nanometre scale about the morphological and topographical aspect of the specimen surface. In modern SEMs, the incorporation of high-efficient spectrometers allows high spatial resolution chemical analysis by means of energy or wavelength dispersive x-ray spectroscopy (EDS/WDS) [2.15, 2.17].

The basic operation of a SEM is the heating of a cathode, which in turn produces electrons. Tungsten and Lanthanum hexaboride (LaB6) filaments are most commonly used as an electron source due to their relatively low work functions and high melting points [2.18]. The energy of the electrons produced range from a few hundred eV to 40keV. The beams of electrons are accelerated towards an anode with the aid of an applied voltage, and eventually make its way through an aperture in the anode into the vacuum chamber of the microscope. The condenser lens is the primary lens influencing the motion of the beam, as it passes through the pole piece. The beam is deflected by the condenser lens, resulting in the formation of a focused beam through the focal point situated above the condenser aperture [2.18]. Below the condenser aperture, the divergence of the beam occurs once more, thus a final objective lens is introduced to focus the beam even further by converging it to a focal point at the surface of the specimen through an objective aperture. The surface of the specimen is then scanned by an electron beam with scanning coils. With the aid of positioning detectors, the signals that are emitted can be utilized for the formation of an image of the scanned near-surface of the specimen. Figure 2.8 shows the schematic diagram of a SEM [2.18].

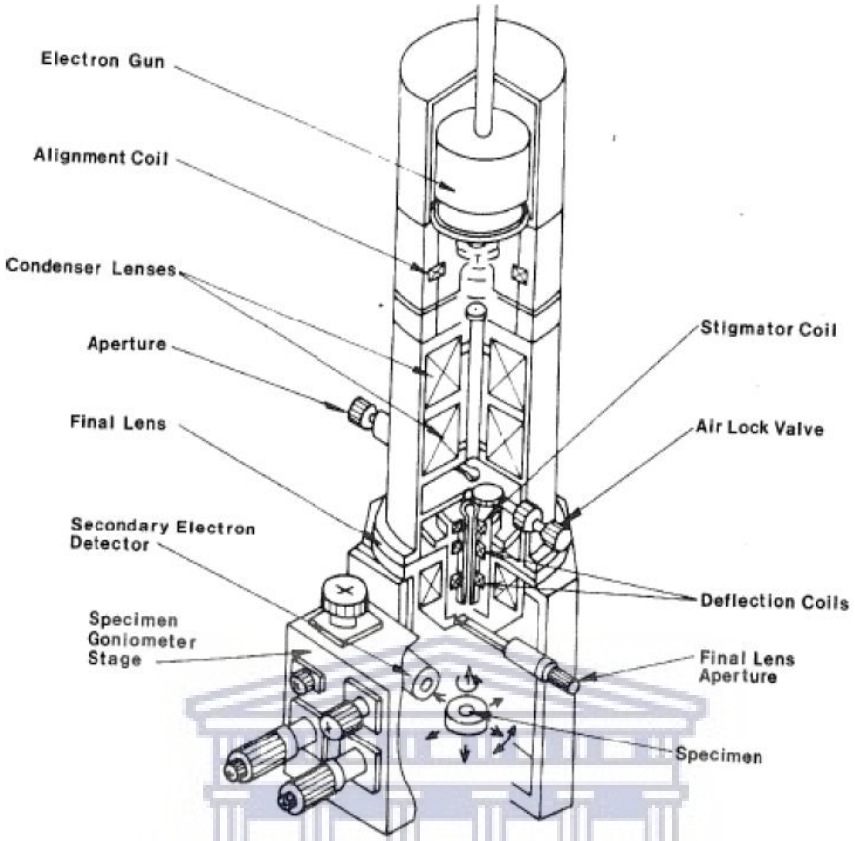

Figure 2. 8: Schematic diagram of a typical scanning electron microscope (SEM) [2.19].

2.3.3.2 Resolution

The concept of resolution can be defined as the closest spacing of two objects which can be seen through the microscope to be separate entities. Obtaining images at high magnifications without adequate resolution is not the desired result when operating the SEM since no additional valuable information can be obtained from the images. The limit of resolution, which is the smallest spacing at which two objects are resolved, can be described mathematically by Abbe's equation [2.13].

$$r = \frac{0.612\lambda}{nSin\alpha}, \qquad (2.14)$$

where r is the limit of resolution, λ is the wavelength of the incident beam, n is the refractive index of the medium between the object and the objective lens, and α is the aperture angle. The best resolution (i.e. the smallest r) can be achieved by decreasing λ or increase n or α.

2.3.3.3 Depth of field and working distance

The depth of field (DOF) can be defined as the range of positions for the objects at which our eye cannot resolve a change in the sharpness of the image. The working distance in the SEM can be defined as the distance between the final condenser lens pole and the top part of the specimen [2.13]. This impacts the DOF for certain samples. A long working distance decreases the angle of the aperture, resulting in greater DOF, whereas a shorter working distance results in the sample being scanned with a wider angle decreasing the DOF (aperture solid angle, α); see Figure 2.9.

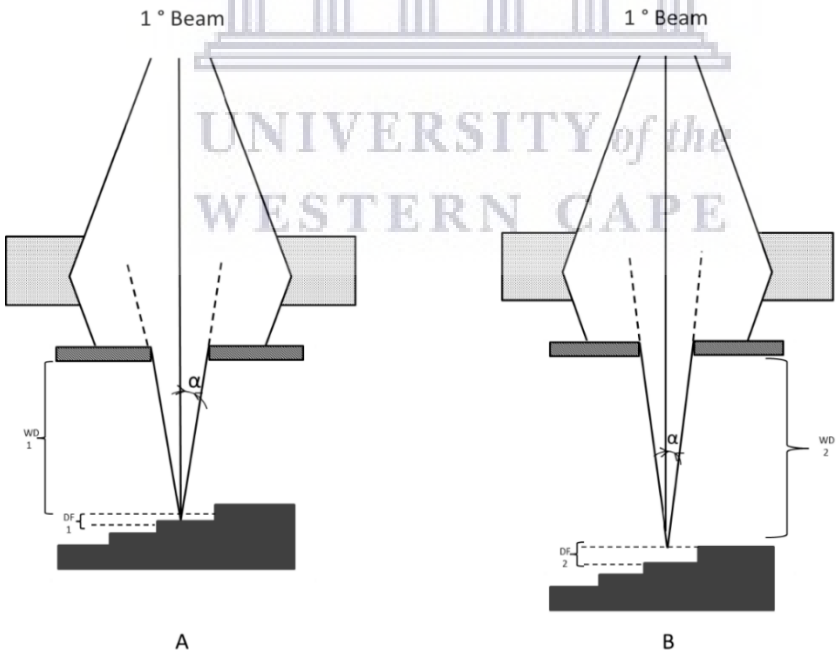

Figure 2. 9: Schematic diagram of the enhancement of the depth of field with an increasing WD, (A) a short working distance (B) a larger WD, showing an increase in in the depth of field (DF) [2.18]

2.3.3.4 Electron beam specimen interaction

In SEM, incident electrons hitting the specimen, might encounter both elastic and inelastic scattering by the atoms in the specimen. Elastic scattering is a process when the electrons trajectory changes, but their incident kinetic energy and velocity remain unchanged. This type of scattering produces backscattered electrons (BE). Another contribution to the backscattered signal arises in the form of low-energy BEs, which are generated by interactions of the incident electrons with the inner atoms of the specimen. Due to a large number of collisions encountered by these inner BEs, electrons emanates from the specimen with little energy, because of the energy transfer to the surrounding atoms; hence secondary electrons (SE) are generated which in turn are easily absorbed by the specimen atoms. In the case of inelastically scattered electrons, energy is lost during interaction with the atoms of the specimen, which gives rise to signals such as SEs, x-rays, auger electrons, and cathodoluminescence. However, some incident electrons, known as transmitted electrons, pass through the specimen; they carry information about the specimen. Such signals are used in TEM. Figure 2.10 below illustrates the signals produced during beam-specimen interaction with signals such as SEs and BEs of importance in the SEM; providing information about the morphology and topography of the sample, whereas the Auger electrons, x-rays and cathode luminescence provide information about the chemical composition of the specimen [2.12, 2.21].

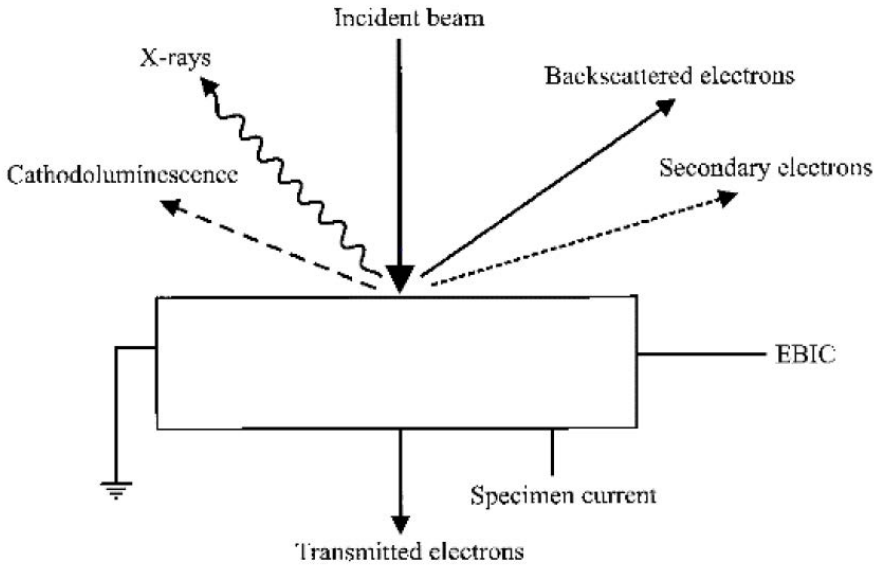

Figure 2. 10: Signals produced during Beam-Specimen Interaction [2.12].

The region into which the primary electrons enter and interact with specimen atoms is known as the interaction volume and is shown in Figure 2.11. Inside the interaction volume, signals are generated at different depths. BEs and SEs generated near the surface are of great importance in image formation since they provide information at good spatial resolution. Illustrated in Figure 2.11 are the three most important SEM signals, used for imaging and chemical analyses, and the different depths in the interaction volume from which they are generated [2.12, 2.21].

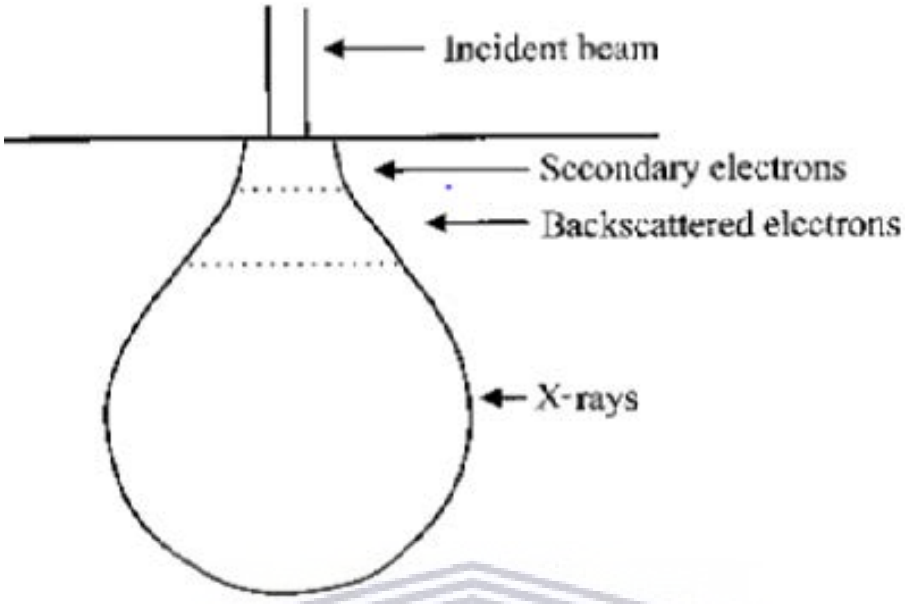

Figure 2. 11: The interaction volume between the electron beam and the specimen [2.12].

2.3.3.5 Detection of secondary and backscattering electrons

In SEM, the most commonly used signal for imaging is SE signals since they have a smaller sampling volume than the BEs which is needed for good spatial resolution. SEs are normally detected by use of a scintillator-photomultiplier known as an Everhart-Thornley detector (ETD). This detector consists of (a) collector which is held at positive bias responsible for collecting SEs from all directions towards the surface of a (b) scintillator that contains phosphor which produces light when electrons fall on it, and is covered with a thin aluminium film held at a potential of a few kV to give electrons excess energy to excite the phosphor, and finally (c) a photomultiplier which amplifies the generated signal into measurable electronic pulses, which are then used to modulate a cathode ray tube with the brightness proportional to the collected SEs [2.12, 2.21]. Figure 2.12 shows a simplified schematic of a typical ETD system [2.12].

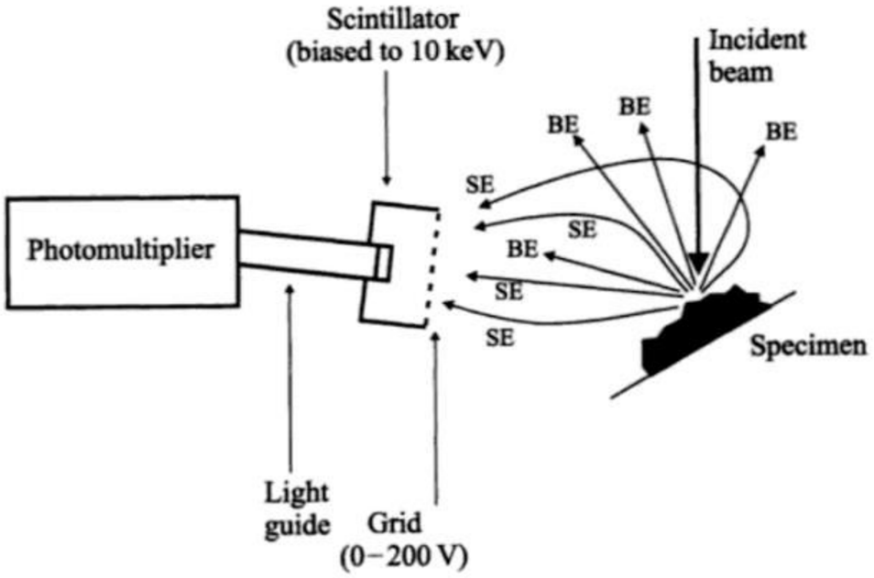

Figure 2. 12: Schematic representation of the components of the Everhart-Thornley detector [2.12].

Evidently, BEs travelling towards the ETD are also detected; BEs contribute to the formation of the image. However, due to the scattering direction of the BEs, a large portion are not detected; hence a scintillation detector with a large cross-sectional area known as a Robinson detector, is placed near the specimen for efficient collection of a large number of BEs as shown in Figure 2.12. For high-resolution SEM a detection system known as the in-lens detector, special for its reduced spherical aberration coefficient, is placed within the strong magnetic field of the objective lens. This allows for the operation at very short working distances (distance from specimen to objective pole piece) owing to the efficient collection ability of both SEs and BEs [2.12, 2.21, 2.22, 2.23]

2.3.3.6 Characteristic X-ray and energy dispersive spectroscopy

Energy Dispersive Spectroscopy (EDS) makes use of the X-ray spectrum emitted by a solid sample bombarded with a focused beam of electrons to obtain a localized chemical analysis. All elements from atomic number 4 (Be) to 92 (U) can be detected in principle, though not all instruments are

equipped for light elements (Z < 10). Qualitative analysis involves the identification of the lines in the spectrum and is fairly straightforward owing to the simplicity of X-ray spectra. Quantitative analysis (determination of the concentrations of the elements present) entails measuring line intensities for each element in the sample and for the same elements in calibration standards of known composition [2.24].

Beam interaction with low accelerating voltages of 5 kV provides more detailed information of the area near to the surface; in comparison with the usage of higher accelerating voltages (15-20 kV) which supplies information of the interior of the sample due to the beam penetrating beneath the specimen surface [2.25].

When an electron in the inner shell is excited to leave an atom or to be promoted into a higher unoccupied level, characteristic X-rays are emitted. The electron will be replaced by one of the electrons in the outer shell by emitting an X-ray photon. If an electron is removed from the K-shell (1s) it can be replaced by an electron from either 2p, 3p or any higher occupied state. The transition energy will be released as X-radiation and the emission lines labelled as Kα, Kβ, etc. [2.26]. The X-ray emission for any specimen can provide an analysis of specimen elements constituents, normally in the regions of 1μm diameter and 1μm depth under normal operating conditions. The Kα and Kβ lines have the highest energy X-ray photons from each atom because the energy is nearly closely equal to the binding energy of the 1s electron (see the representation in Figure 2.13).

Characteristic x-rays can be detected with a wavelength dispersive spectrometer which measures accurately the wavelength and energy of the x-ray and alternatively, modern SEMs use EDS detection systems but these are associated with loss of precision and resolution. An EDS detector consists of a piece of semiconductor material (silicon or germanium) held in a position where many x-rays emitted by a specimen will fall on it. For

efficient collection of x-rays, it is required that the detector must be as close as possible and in the line of sight of the specimen. These x-rays are converted to measurable signals within the detector which forms the EDS spectra.

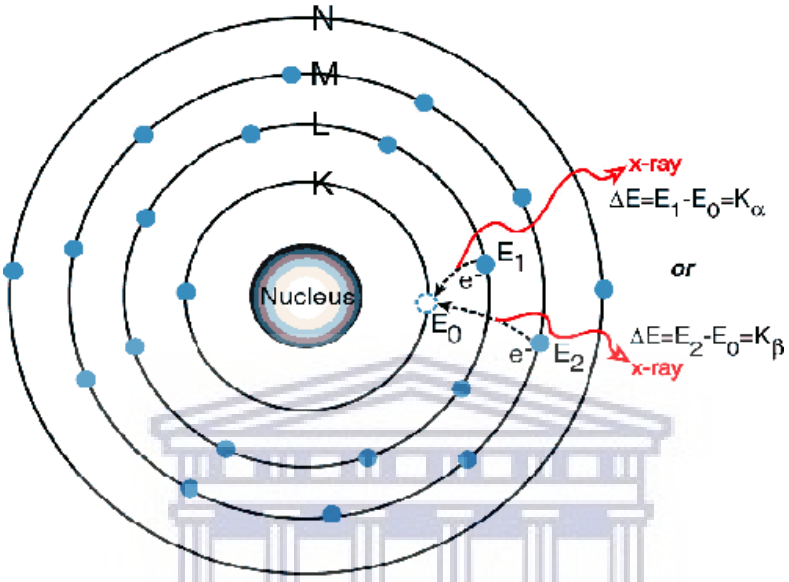

Figure 2. 13: Characteristic x-ray emission by an atom [2.25].

2.3.3.7 Focussed Ion Beam Scanning Electron Microscopy (FIB-SEM).

Focused Ion Beam (FIB) preparation is a method to prepare ultrathin samples by making use of a function called ion milling for the final phase studies with TEM. A beam of focused ions strikes and removes material from the specimen surface by a physical sputtering process. This ion beam is generated by a gallium (Ga^+) ion source at the top of the ion beam column. Ions are emitted as a result of a high excitation field and accelerated down the FIB column towards the specimen. When Ga^+ ions are accelerated towards the specimen they can penetrate beneath the surface up to 10 nm. During ion milling, the SE yield is much higher than secondary ion yield, hence secondary ions are used to image and mill the specimen, as illustrated in Figure 2.14. The FIB is a tool utilized for tasks such as cross-sectioning for interfacial microstructure studies, preferential removal of certain metals or oxides, semiconductor device alterations, site-specific

TEM sample preparation, and grain imaging. By introducing gases or an organic gas compound, the FIB can specifically etch one material much faster than the surrounding materials, or deposit a metal or oxide. The FIB instrument combined with SEM allows simultaneous monitoring of the process. The deposition mechanism is where the accelerated highly energetic gallium ions decompose the precursor gas molecules to metal deposits and volatile products leaving the metal deposits like platinum on the surface of the substrate [2.27-2.30].

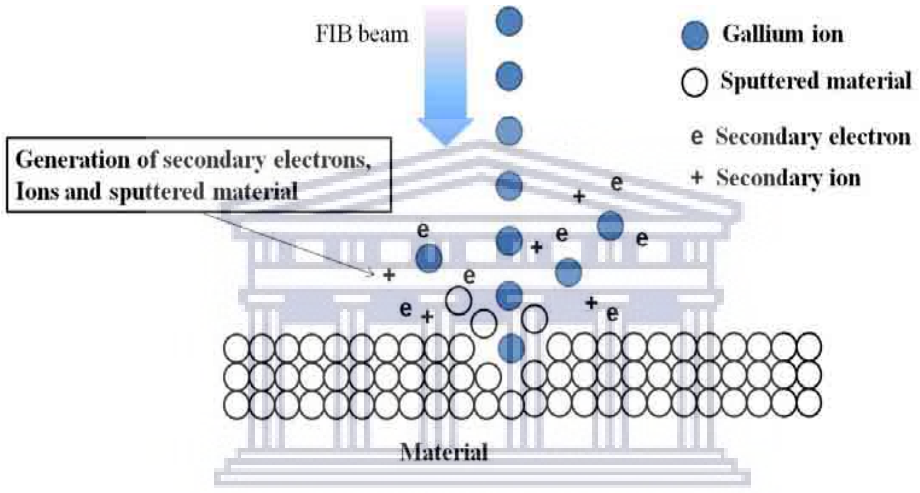

Figure 2. 14: Ga^+ ions upon striking the surface of the material generate electron, ions and sputter material [2.27].

2.3.3.8 Experimental set-up

Scanning electron microscopy (SEM), combined with energy dispersive x-ray spectroscopy (EDS) was used to study the morphology and elemental composition of the thin films. A Zeiss Auriga field-emission gun (FEG) SEM operated at 5kV using an in-lens secondary electron detector was used for high-resolution imaging, whereas an Oxford Instruments X-Max solid-state silicon drift detector was used for the EDS analyses (University of the Western Cape, UWC).

A Zeiss Cross Beam 540 Focused Ion Beam Scanning Electron Microscope (FIB-SEM) operated at acceleration voltages of 1-5 kV (NMISA, Pretoria) was used for the ion milling in preparation of a TEM lamella sample of the devices and also the transfer and mounting of the cut lamella to a FIB TEM grid.

2.3.4 Stylus Profilometry

2.3.4.1 Introduction

The Dektak 6M stylus profilometer was employed to measure the nominal thickness of the various samples discussed in this work. The Dektak 6M stylus profilometer is an advanced thin and thick film measuring tool. It makes use of a 12.5 µm diamond-tipped stylus with a programmable stylus force ranging from 1 mg to 15 mg; allowing for soft or hard surfaces [2.31]. The instrument comes with a high-resolution video camera attached to the scan head. This allows for sample viewing and magnification possibilities during the measuring process. In addition, it comes with software which allows for profile levelling, zero referencing and magnification [2.31].

2.3.4.1.1 Principle of operation

The profilometer takes measurements electromechanically by moving the sample underneath the stylus. Here, a high precision stage moves together with the sample underneath the stylus-based on the user-programmed parameters [2.31]. As the stage moves the sample, the stylus which is mechanically connected to a linear variable differential transformer (LVDT) is translated in the vertical motion relative to the sample surface. The LVDT as depicted in Figure 2.15, detects and produces electrical signals according to the stylus movement by comparing the alternating current (AC) reference signal proportional to the position of change. This analogue signal is then conditioned and digitally converted for imaging and analysis.

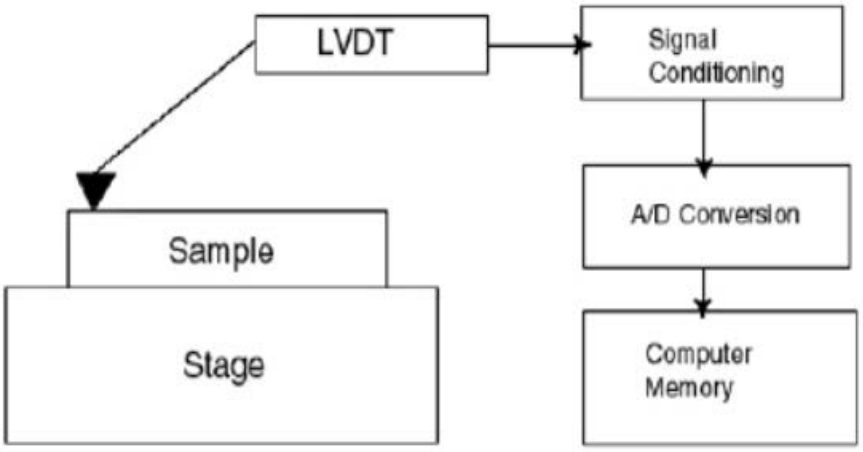

Figure 2. 15: Block Diagram of Dektak 6M Architecture [2.31].

2.3.5 Fourier transform infrared (FTIR) spectroscopy

2.3.5.1 Introduction

FTIR Spectroscopy is a non-destructive analytical technique that uses the photons in the infrared region of the electromagnetic spectrum. These photons have sufficient energy to induce amplified molecular vibrations in the infrared (IR) - active side of the sample's molecules. During this process, there is a change in the dipole moment of the infrared (IR) active molecule, which results in a signature spectrum of the molecule under investigation when measured [2.32].

2.3.5.2 Theory

When a beam of electromagnetic radiation is incident on a material, the beam can be absorbed, transmitted or reflected depending on its frequency, and the molecular structure of the material being irradiated. Beams of different frequency can have different effects on the molecules of the substance that is being irradiated. When a beam of electromagnetic radiation

which has a frequency in the 1.2×10^{13} Hz to 1.2×10^{14} Hz (infrared frequency) band is passed through a sample, it affects a transition from one molecular vibrational energy to the next on the IR active molecule [2.33]. The photons of electromagnetic radiation possess energy, hence when a molecule absorbs electromagnetic radiation it gains energy to make a quantum transition from energy level E_1 to E_2. The frequency υ of the absorbed radiation is associated with the transition energy by Planck's law:

$$E_1 - E_2 = h\upsilon = \frac{hc}{\lambda}. \qquad (2.15)$$

If there exists an allowed transition that is related to the frequency of the incident radiation by Planck's constant, then the radiation will be absorbed; if the transition is forbidden (does not satisfy the Planck's equation) then the incident radiation will be transmitted. When molecules vibrate, they do so with a frequency characteristic to the constituent elements. Only certain molecular vibrational motions are allowed as permitted by quantum mechanics. For example, in the case of thin films of hydrogenated silicon (Si:H) irradiated by an IR radiation, different IR active hydrogen silicon bonding configurations will absorb IR photon energy in different specific regions of the spectrum. The hydrogen atom that is bonded to silicon in the Si matrix produces a local vibrating dipole, this is because of the difference in the electronegativity between the hydrogen atom, which is negatively charged, and the silicon atom which is positively charged [2.33]. In this harmonic oscillator of Si-H, the dynamic dipole moment changes when an IR photon is absorbed by a Si-H oscillator. This result in a vibrational state with a larger vibrational dipole moment; this change in dynamic dipole moment and the concentration of the bonded hydrogen atoms will contribute to the spectral band and its intensity in the IR spectra [2.32]. A similar analogy can be made for IR-active bonds in other materials.

2.3.5.3 Experimental Setup

FTIR transmission spectra were collected from 400 – 4000 cm^{-1} with a spectral resolution of 1 cm^{-1}, using a Perkin-Elmer Spectrum 100 FTIR spectrophotometer (UWC, Chemistry department). Unlike glass, semiconductors like silicon have superior infrared transparency; hence mono-crystalline silicon (mc-Si) wafers are used for characterization. Infrared transmission $T(\omega)$ as a function of vibrational frequency ω was measured by first collecting a background spectrum of the c-Si substrate which is used to correct the background signal; hence the resultant plot is the spectrum obtained for the thin film layer only.

2.3.6 Ultraviolet-visible (UV-Vis) spectroscopy

2.3.6.1 Introduction

UV-Vis spectroscopy is a technique that utilizes visible, near-infrared and near-ultraviolet light for analysis. The region absorbed by the material extends from 190-400 nm which corresponds to the ultraviolet range, whilst ranges from 400-780 nm correspond to the visible range. When this kind of electromagnetic radiation interacts with molecules, the electrons of the molecules undergo transitions [2.34]. Absorption spectroscopy is the process whereby transition occurs from the ground state, whereas in the case of emission spectra the transition occurs from the excited state to the ground state. The optical properties of the light being absorbed by material are crucial to the power conversion efficiency. The optical band gap is particularly studied for solar cell application; since the electronic structure of the material is related to it.

2.3.6.2 Theory

When light impinges on a film, molecules within the film can undergo electronic transitions from the ground state to the excited state. The ratio of the radiation intensity transmitted by the film of thickness x (I_x) to that transmitted by a known reference (I_o) is known as the transmittance (T) of the film and is given by:

$$T = \frac{I_x}{I_o}. \qquad (2.16)$$

In practice, we often measure percent transmittance (%T), because many instruments are calibrated with its very convenient scale of 0 to 100. A more useful quantity is the amount of radiation absorbed, referred to as the absorbance (A), given by:

$$A = ln\left(\frac{I_O}{I_x}\right) = ln\left(\frac{1}{T}\right). \qquad (2.17)$$

There is also a variety of energy absorptions possible depending upon the nature of the bonds within a molecule. For instance, electrons in organic molecules may be in strong sigma (σ) bonds, in weaker pi (π) bonds or non-bonding (n). When energy is absorbed all of these types of electrons can be elevated to excited anti-bonding states that can be presented as in Figure 2.16, the anti-bonding states being represented with an asterisk as σ* and π*. Most σ → σ* absorptions for individual bonds occur below 200 nm in the vacuum/ultraviolet region and compounds containing just the σ bonds are transparent in the near-ultraviolet/visible regions. The π → π* and n → π* absorptions of organic compounds mostly occur in the near-ultraviolet/visible region and result from the presence in molecules of unsaturated groups providing π electrons [2.35].

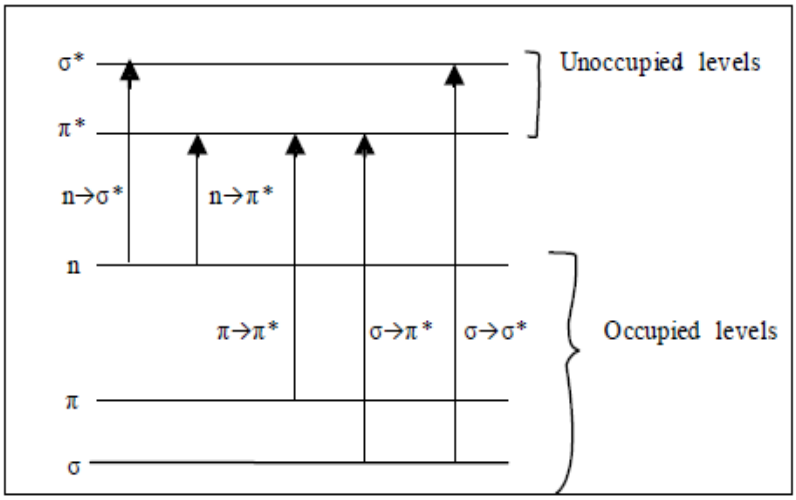

Figure 2. 16: Bonding and anti-bonding energy transitions [2.35].

2.3.6.3 Band gap analysis

The band gap is generally obtained from the absorption edge energy; defined to be the minimum photon energy required to excite an electron from VB to the CB. There are two types of transitions - direct and indirect.

The optical band gap of the thin films was evaluated from the transmission spectra of the thin films coated on quartz glass substrates. Then, the determination of the optical band gap is done by extrapolation of Tauc's plot [2.36] from

$$(\alpha h\upsilon)^{1/n} = B\,(h\upsilon - Eg). \qquad (2.18)$$

In the above equation, n=1/2 for direct allowed transitions, n=2 for indirect allowed transitions, where B is a constant independent of energy and h is Planck's constant, hυ is the photon energy and α is the absorption coefficient. To determine the bandgap by extrapolation of Tauc's plot the value of α should be known. The optical absorption coefficient can be calculated using equation (2.16):

$$\alpha = \left(\frac{1}{\mathrm{t}}\right) ln\left(\frac{1}{T}\right), \qquad (2.19)$$

where t is the film thickness and T is the transmittance. A graph is plotted of $(\alpha h\upsilon)^{1/n}$ versus (hυ), n = 1/2 for direct allowed transitions. The extrapolation yields a good straight-line fit to the absorption edge and provides the optical band gap value from the hυ axis.

2.3.6.4 Diffuse reflectance spectroscopy

Figure 2.17 illustrates the interaction of incident light reacting with optically scattering surfaces which may contain roughness. This incoming light can be partly reflected specularly, partly scattered diffusely, and partly enter the substrate. Some of the incoming light may also be absorbed within the particles, undergo diffraction at grain boundaries, re-emerge at the sample surface and intermingle with reflected parts.

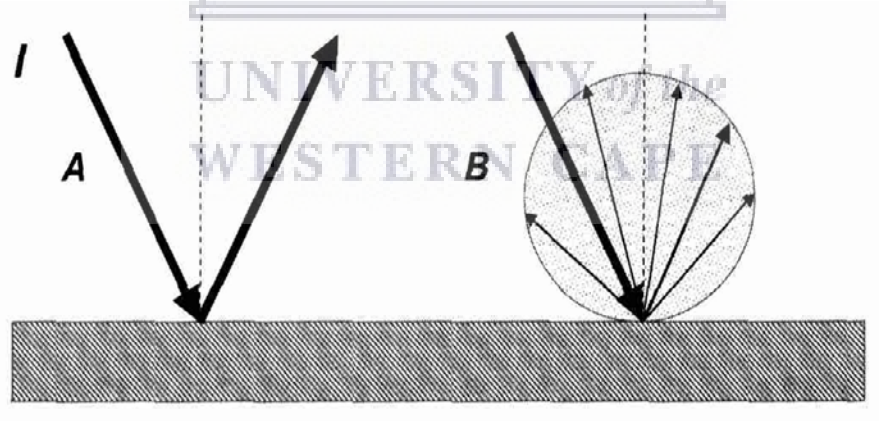

Figure 2. 17: Light scattering at smooth non-absorbing surfaces after irradiating the particle surface with light I: specular reflected light (A) and diffuse reflected light (B) [2.37].

When the dimensions of the particle is smaller than the beam cross-section but relatively larger than the light wavelength, then diffraction phenomena occur due to the incoming rays striking and/or passing by the crystal,

resulting in interference among elementary waves. In powders of randomly oriented particles of such size, part of the incident light goes back at all angles into the hemisphere of provenance of the light. The phenomenon resulting from the reflection, refraction, diffraction, and absorption by particles oriented in all directions is called diffuse (or volume) reflection, in contrast with regular (or directional) reflection from a plane phase boundary. The basic equation for the phenomenological description of diffuse reflection is the radiation transfer equation:

$$\frac{-dI}{\kappa \rho dS} = I - \frac{j}{\kappa}, \qquad (2.20)$$

where I is the incident light intensity of a given wavelength; dI/dS the change of the intensity with the path length dS; ρ the density of the medium; κ an attenuation coefficient corresponding with the total radiation loss due to absorption and scattering and j is the scattering function. Equation (2.20) can be solved by introducing simplifications which are related with easily attainable experimental conditions. These ideas, first suggested by Schuster and further developed by Kubelka and Munk, simplify the solution of the radiative transfer equation (2.20), known as the Schuster-Kubelka-Munk (S-K-M) theory [2.37-2.39]. In this theory, the incident and scattered light flux are approximated by two fluxes I and J perpendicular to the surface of the powdered sample, but in the opposite direction. This is illustrated in Figure 2.18.

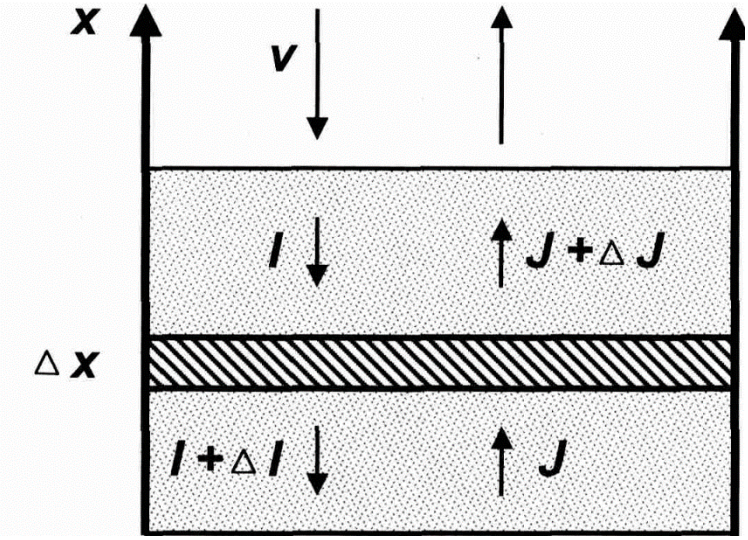

Figure 2. 18: The S-K-M approximation: the incident and remitted light fluxes are approximated by two opposite fluxes I and J, perpendicular to the surface of the infinitely thick sample layer [2.37].

I is the flux of monochromatic diffuse illumination and J is the flux of diffusively scattered light. For an infinitely thick sample, the diffuse reflection is related to an apparent absorption (K) and apparent scattering coefficient (S) via the S-K-M or Kubelka-Munk (K-M) function:

$$F(R_\infty) = \frac{(1-R_\infty)^2}{2R_\infty} = \frac{k}{s}, \quad (2.21)$$

where $F(R_\infty)$ is usually the remission or K-M function. The bandgap can be obtained from the plots of $[F(R_\infty)\ h\upsilon]^{1/2}$ versus $h\upsilon$, as the intercept of the extrapolated linear part of the plot at $[F(R_\infty)\ h\upsilon]^{1/2} = 0$, assuming that the absorption coefficient α is proportional to $F(R_\infty)$. Equation (2.21) is valid under the following conditions [2.37]:

1. diffuse monochromatic irradiation of the powdered sample;
2. isotropic light scattering;
3. an infinite layer thickness;
4. a low concentration of powders;
5. a uniform distribution of powders;
6. absence of fluorescence.

2.3.6.5 Experimental

The absorbance and transmission spectra were recorded with a Semiconsoft UV-vis spectrometer over a spectral range of 200 nm to 800 nm. The spectrometer used has two independent radiation sources, namely UV (deuterium lamp) and visible (halogen lamp). A monochromator is employed to filter the incident radiation of a single wavelength to reach the detector, which then converts the incident electromagnetic radiation into electrical energy. Diffuse reflectance measurements were performed using a Cary 5000 in the range of 200 to 800 nm. Diffuse reflectance makes use of an integrating sphere with a white coating inside to obtain measurements. The light that reaches the detector are scattered diffusely and reflects multiple times inside the integrating sphere.

2.3.7 Current – Voltage characterization

2.3.7.1 Introduction

A solar cell can be summarized as a combination of both, a current source and a voltage source, as shown in Figure 2.19. This device is effectively known as a diode. In an ideal cell the series resistance, R_s, would be zero and the parallel or shunt resistance, R_{sh}, infinitely large. However, in reality this is not the case. The series resistance is composed of the electrical resistances of the different materials in the cell and the interfaces between them; the resistance of the transparent conducting oxide layer is the biggest contributor to the series resistance of the cell. The shunt resistance indicates the resistance between the electrodes through undesirable routes, hence in a highly efficient cell the shunt resistance must be as high as possible [2.40].

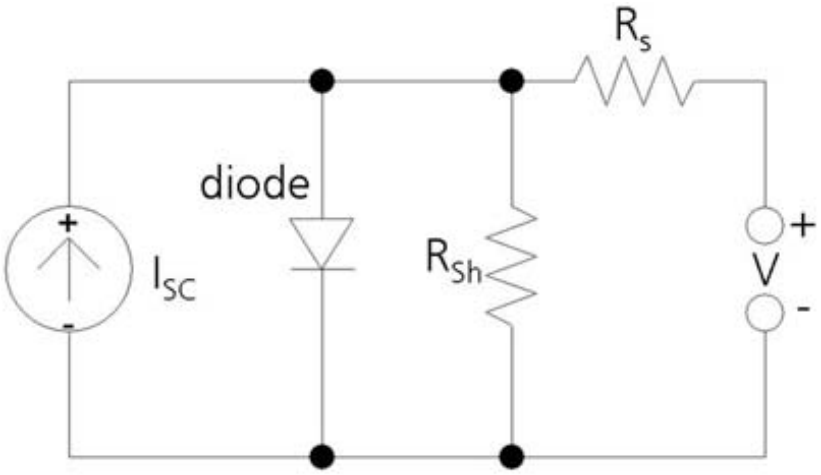

Figure 2. 19: Illustration of an equivalent circuit a solar cell [2.40].

A typical current density - voltage (J – V) curve of a solar cell is shown in Figure 2.20. In general, the current density, defined as the current (I) per unit area, and labelled j, is plotted against the voltage, V. The important features in Figure 2.20 are the short-circuit current density J_{sc}, the open-circuit voltage V_{oc} and the maximum power point P_{max} (or MPP) with its corresponding current-density and voltage (J_{mp}, V_{mp}).

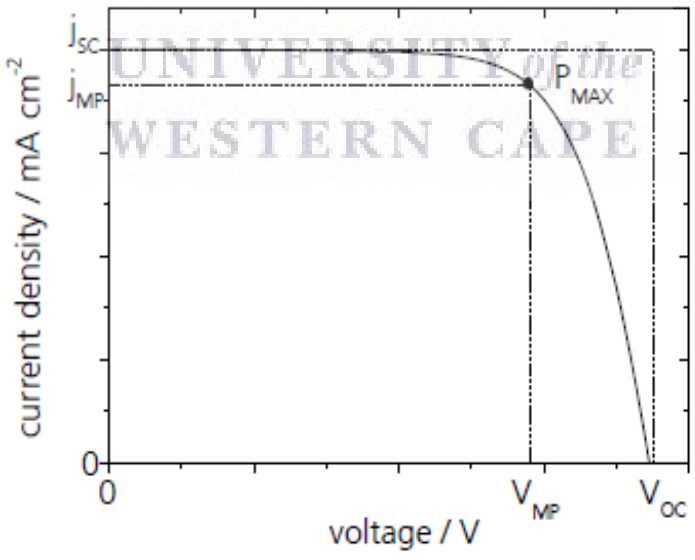

Figure 2. 20: Typical J-V curve of a solar cell [2.40].

The fill factor, FF, of the solar cell is defined as the squareness of the J-V curve and is given by

$$FF = \frac{P_{max}}{J_{sc} \times V_{OC}} = \frac{J_{mp} \times V_{mp}}{J_{sc} \times V_{oc}} \quad (2.22)$$

with P_{max} (maximum power density) given in W/cm^2. The efficiency of the cell, η is given by

$$\eta = \frac{P_{max}}{P_{in}} = FF \left(\frac{J_{sc} \times V_{OC}}{P_{in}} \right) \quad (2.23)$$

where P_{in} (power density) is the power of the incident irradiation given in W/cm^2.

The power output of a solar cell is highly dependent on the power of the incident irradiation. The standard is an incident spectrum of AM 1.5 G, an international standard for incident power density of 100 mW/cm² or 1000 W/m² is used while at room temperature [2.40].

The one - diode model can be modelled by figure 2.19, where the diode equation becomes

$$I(V) = I_{sat} \left[exp \frac{e_0 V}{m_D k_B T} - 1 \right] + I_{sc} \quad (2.24)$$

where I_{sat} = the diode saturation current,
I_{sc} = photocurrent,
e_0 = electron charge,
m_D = diode ideality factor,
k_B = Boltzmann constant and
T = temperature

The diode has an ideality factor of 1 from semiconductor theory. However, real diodes deviate from the ideal diode equation where m_D = 1. In real silicon diodes, the ideality factor is 2 for low currents and 1 for high

currents. The one-diode model is sometimes also called the standard solar cell equation. In a real solar cell, the series, R_s and shunt, R_{sh} resistances have to be taken into account, as shown in Figure 2.20. The current then becomes

$$I(V) = I_{sat}\left[exp\frac{e_0V - e_0R_sI}{m_Dk_BT} - 1\right] + I_{sc} + \frac{V - R_sI}{R_{sh}} \qquad (2.25)$$

with the quantity, $\frac{V-R_sI}{R_{sh}}$ known as the shunt current, I_{sh}. The influence of the series and shunt resistances on the J-V curve of a solar cell is shown in Figure 2.21.

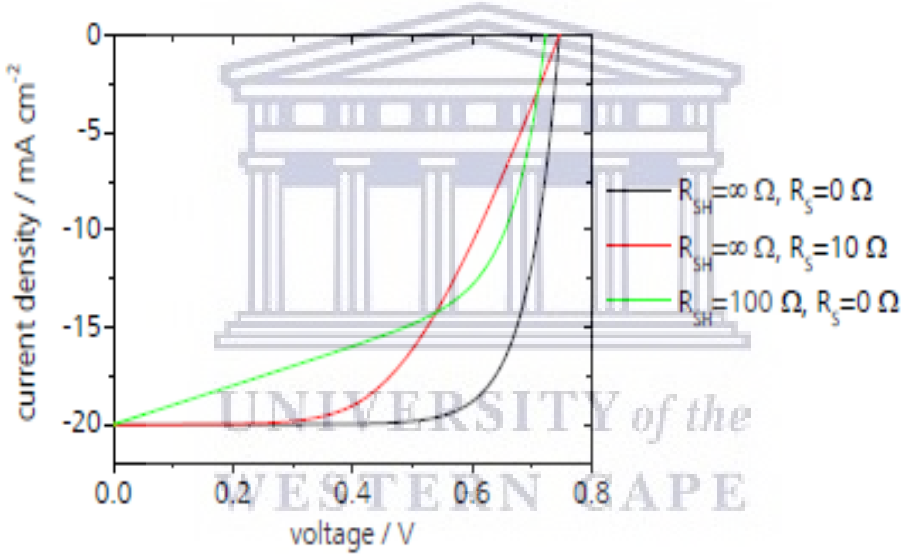

Figure 2. 21: Effect of R_s and R_{sh} on the J-V curve of a solar cell [2.40].

It can be seen from Figure 2.21 that low shunt resistances (typically in the region of 100 Ω) increase the slope of the flat part of the J-V curve, whereas high series resistances decrease the slope of the ascending part of the curve. Hence, a direct measure of these two quantities can be obtained from calculating the inverse of the slope of the tangent line at these two parts of the J – V curve. At infinitely high shunt and zero shunt resistances, I_{sh} in equation (2.25) becomes negligible and the J – V relation tends towards that of the ideal diode, i.e. equation (2.24).

2.3.7.2 Experimental set-up

The I – V characteristics of the OSCs were analysed under the illumination of AM1.5G spectrum. The devices were irradiated at 100 mW/cm^2 using a xenon lamp-based Sciencetech SF150 solar simulator equipped with an AM1.5 filter as the white light source. The power intensity at the sample was measured with a Daystar light meter. A bias voltage is swept from 0 V to 0.8 V, using a Keithley 2420 source meter unit. The dark I-V curve is recorded while the testing device is not under illumination. All the photovoltaic properties were evaluated at room temperature in ambient conditions.

References

[2.1] Ossila spin coater user manual (2018), *System components and overview*.

[2.2] Irzaman, H.S. and Siskandar, R., 2017. Modified Spin Coating Method for Coating and Fabricating Ferroelectric Thin Films as Sensors and Solar Cells. Thin Film Processes: Artifacts on Surface Phenomena and Technological Facets, p.33.

[2.3] Sahu, N., Parija, B. and Panigrahi, S., 2009. Fundamental understanding and modelling of the spin coating process: A review. Indian Journal of Physics, 83(4), pp.493-502.

[2.4] Tyona, M.D., 2013. A theoretical study on spin coating technique. Advances in materials Research, 2(4), pp.195-208.

[2.5] Serway, R. and Jewett, J., 2009. Physics for Scientists and Engineers, Nelson Education.

[2.6] Ohring, M., 2001. Materials science of thin films. Elsevier.

[2.7] West, A. R., (1984). Solid State Chemistry and its Applications, Wiley, New York.

[2.8] Cullity, B. D., (1978). Elements of X-ray diffraction, Addison-Wesley Publishing Company, Reading, Massachusetts.

[2.9] Palanna, O. G., (2009). Engineering Chemistry, Tata McGraw Hill Education Pvt. Ltd., New Delhi.

[2.10] Birkholz, M., 2006. Thin-film analysis by X-ray scattering. John Wiley & Sons.

[2.11] Welzel, U., Ligot, J., Lamparter, P., Vermeulen, A.C. and Mittemeijer, E.J., 2005. Stress analysis of polycrystalline thin films and surface regions by X-ray diffraction. Journal of Applied Crystallography, 38(1), pp.1-29.

[2.12] Goodhew, P. J., Humphrey, Beanland, J. R., (2001). Electron Microscopy and Analysis-Third Edition, Taylor and Francis, London.

[2.13] Chescoe, D. and Goodhew, P. J., 1984. The Operation of the Transmission Electron Microscopy, Royal Microscopical Society and Oxford University Press, New York.

[2.14] Willards, H.H., Merritt Jr L.L., Dean, J.A. and Settle Jr., F.A., (1988). Instrumental Methods of Analysis 7th Edition, Wadsworth Publication. Co.

[2.15] Goodhew, P. J., Humphrey, Beanland, J. R., 2000. Electron Microscopy and Analysis. Taylor & Francis, London and New York.

[2.16] Watt, I., 1997. The principles and Practice of Electron Microscopy, Cambridge University Press. Great Britain.

[2.17] Yao, N. and Whang, Z. L., 2005. Handbook of Microscopy for Nanotechnology, Kluwer Academic Publishers. London.

[2.18] Postek. M, Howard. K, Johnson. H and McMichael. K, (1980). Scanning Electron Microscopy- A student's handbook, Vermont: Ladd Research Industries.

[2.19] Nalwa. H, Handbook of Thin Films Materials, (2002). Academic Press, 5, p.61.

[2.20] Hibbs, A. (2004). Confocal Microscopy for Biologists, Twayne Publishers, Boston.

[2.21] Poster, T. M., Howard, S. K. A., Johnson, H and McMichael, K. L., 2001. Scanning Electron Microscope, Ladd Research Industries. The United States of America.

[2.22] Egerton, R. F., 2005. Physical principles of Electron microscopy. Springer and Business Media Inc, New York.

[2.23] Wischnitzer, S., 1970. Introduction to Electron Microscope, 2nd Edition. Pergamon Press Inc. The United States of America.

[2.24] Russ, J. C., (1984). Fundamentals of Energy Dispersive X-ray Analysis, Butterworths. London.

[2.25] Semwogerere, D. and Weeks, E. R., (2005). Encyclopedia of Biomaterials and Biomedical Engineering Confocal Microscopy, Taylor Francis

[2.26] Sheppard, C., (1997). Confocal Laser Scanning Microscopy, Twayne Publishers, Boston.

[2.27] Jeng, L.F., 2015. Materials development and interface studies of inverted organic solar cells. PhD Thesis, National University of Singapore.

[2.28] Fagerland, S.K., 2014. Investigation of focused ion beam/scanning electron microscope parameters for slice and view and Energy Dispersive X-ray spectroscopy of embedded brain tissue Master's thesis, Norwegian University of Science and Technology.

[2.29] Kuzmin, O.V., 2014. Intrinsic and extrinsic size in metallic glasses Doctoral dissertation, University of Groningen.

[2.30] Kamalakar, M.V., 2011. Synthesis, characterization and investigation of electrical transport in metal nanowires and nanotubes. arXiv preprint arXiv:1110.5260.

[2.31] Dektak 6M manual (2002), System overview, Digital Instruments Veeco Metrology Group.

[2.32] Lau, W.S. Infrared characterization for microelectronics. World Scientific. ISBN 9810223528 (1999).

[2.33] Properties of Amorphous Silicon and its Alloys. Edited by Tim Searle. An INSPEC Publication, Emis Data Review series. ISBN 0852969228.

[2.34] Denney, R.C and Sinclair, R. (1987). Visible and Ultraviolet spectroscopy. Chichester: Published on behalf of ACOL. John Wiley.

[2.35] Thomas, M.J.K. and Ando, D.J. (1996). Ultraviolet and Visible Spectroscopy. 2nd ed. Chichester, England. Wiley & Sons.

[2.36] Aydogu, S., Sendil, O. and Coban, M. B., (2012). The Optical and Structural Properties of ZnO Thin Films Deposited by the Spray Pyrolysis Technique. Chinese Journal of Physics 50, no. 1: 89-100.

[2.37] Weckhuysen, B.M., 2004. Ultraviolet-visible spectroscopy. In-situ spectroscopy of catalysts, p.255.

[2.38] Torrent, J.O.S.E. and Barrón, V.I.D.A.L., 2008. Diffuse reflectance spectroscopy. Methods of soil analysis. Part, 5, pp.367-387.

[2.39] Khoshhesab, Z.M., 2012. Reflectance IR spectroscopy. Infrared spectroscopy-materials science, engineering and technology, 11, pp.233-244.

[2.40] R. Sastrawan, Photovoltaic Modules of Dye Solar Cells, PhD Thesis, Albert-Ludwig University, Freiburg Germany (2006).

CHAPTER THREE

3 Investigation of the influence of annealing treatment on the morphology, structural and optical properties of Zinc Oxide (ZnO) thin film layers.

3.1 Introduction

This chapter provides a general review of the experimental procedures used for the preparation and characterization of the ZnO thin films based on two post annealing treatment processes. Two types of annealing, conventional annealing and ramp-annealing have been investigated, respectively. In addition to the ramp-annealing, adjustments to the ZnO precursor concentration are also discussed as it exhibits additional changes in the formation of nanostructures on the surface of the ramp-annealed thin films.

Previous studies on ZnO showed it to be a versatile semiconducting material, with a vast variety of applications in electronics such as optoelectronic devices, thin film transistors, sensors and solar cell technology [3.1, 3.2]. In addition, ZnO thin films, with a wide band gap of (3.37 eV) and a large excitonic binding energy of (60 meV) allows efficient exciton emission even at room temperature; which can ensure high-efficiency photonic devices [3.3, 3.4]. ZnO possesses a unique position amongst materials owing to its superior and diverse combination of interesting properties such as excellent chemical, physical and thermal stability in different environments, nontoxicity, high transparency in the VIS/near IR spectral region, good electrical properties, excellent substrate adherence, good contacts to the active semiconductors, chemical stability and it is abundant and inexpensive [3.1-3.12]. Moreover, thin films of ZnO can be prepared by various techniques; amongst them are sputtering [3.5],

chemical vapour deposition (CVD) [3.6], molecular beam epitaxy [3.7], sol-gel process [3.1, 3.2, 3.3], and spray pyrolysis [3.8].

Owing to the previously mentioned advantages of the sol-gel spin coating method in (chapter 2.2.1.1), sol-gel ZnO thin films are customarily used as the ETL [3.12]. However, the quality of the ZnO thin film is still affected by many factors [3.4], hence in this work, the effects of the ZnO precursor concentration and the post annealing procedure on the ZnO thin film were studied for its application in organic/ hybrid solar cells. The effects of annealing on the surface, structural and optical properties were investigated to establish to which extent the light scattering from the conventionally annealed and ramp-annealed ZnO thin films affects the efficiency of the organic/ hybrid OSC device.

3.2 Experimental details

3.2.1 Sample preparation

The ZnO precursor solution was prepared using Zinc acetate dihydrate (ZAD), 2-methoxyethanol and ethanolamine (MEA) as the starting material, solvent and stabilizer, respectively. All the materials were purchased from Sigma Aldrich.

In this work, ITO coated on a 1 mm-thick glass substrate, with a resistance of 8 – 12 Ω/square, and 300 μm-thick single-side polished <111> crystalline silicon (c-Si), with a resistivity of 1-30 Ω.cm, as well as quartz glass were used as substrates. This allows for the execution of various characterisation techniques. These substrates were cut into the desired dimensions prior to the spin coating process and then ultrasonically cleaned with organic solvents to rid their surfaces of impurities. The cleaning sequence was as follows: 10 minutes in acetone followed by 10 minutes in ethanol. Lastly, deionised water was used to rinse off the substrates to remove any traces of the solvents and subsequently dried using compressed air.

3.2.2 Preparation of ZnO thin film by conventional annealing.

This study employed the commonly used conventional annealing process to produce a compact crystalline ZnO thin film layer. We adopted and modified the deposition method developed and reported in the literature [3.13, 3.14, 3.23]. In a typical process, 658 mg of ZAD is dissolved in 5 ml of 2-methoxyethanol. Then, the mixture is magnetically stirred for 1 min, resulting in a milky solution. This is followed by adding 180 µl of MEA dropwise in the solution until it turns clear. The molar ratio of MEA and ZAD was maintained at 1 and the obtained concentration of zinc acetate was 0.6 M; the optimal concentration suggested by Kim et al. [3.13] for growing ZnO thin films. The resulting solution was then vigorously stirred using a magnetic stirrer operated at room temperature for the duration of 12 hours to yield a clear and homogenous solution. Thereafter, the prepared solution was allowed to age for 24 hours at room temperature. This mixture served as the coating solution.

Following the cleaning of the substrate, 200 µl of the ZnO precursor solution was dropped on the ITO substrate until the entire surface was covered. The substrate was then rotated using an Ossila spin coater; the spin coater reached 4000 rpm which was maintained for 40 seconds.

After coating, the coated thin film was placed on a Chemat hot plate that was pre-heated at 250 °C for 10 min in order to evaporate the residual solvent completely and decompose the zinc acetate, resulting in the formation of the thin film. After the deposition and drying procedure, the resulting thin film was placed into a tube furnace where it was annealed in air at 500 °C for 1 hour to form crystalline ZnO. During the annealing process, the furnace was ramped up at 10 °C/ min to the desired 500 °C and dwelled there for 1 hour before cooling. The thin film sample was then removed.

3.2.3 Preparation of ZnO thin film by ramp-annealing

We proposed a fundamental and complete study of the surface, structural and optical properties of the ZnO thin film based on a slightly modified version of the commonly used annealing process and compare it with the ramp-annealed ZnO thin film. Thermal annealing treatment is a common process to achieve a modified surface morphology for improving surface roughness and enhancing the thin film properties by changing their microstructures. In addition, the preparation of the ZnO thin films was carried out in three different concentration regimes to control the morphology. A total volume of 5 ml of 2 – methoxyethanol solution was used for each concentration. The chemical composition for the ZnO precursor solution with different concentration parameters is summarised in table 3.1 below.

Table 3. 1: Chemical composition for the ZnO precursor solution with different concentration determined by the various volume of MEA and different mass of ZAD.

ZAD (mg)	**MEA (µl)**	**2 – methoxyethanol (ml)**
494	137	5
658	180	5
832	229	5

The first solution was prepared by dissolving 494 mg (0.45 M) of ZAD in 5 ml of 2-methoxyethanol before adding 137 µl of MEA. The second solution consisted of 658 mg (0.60 M) of ZAD, 180 µl of MEA and 5 ml of 2-methoxyethanol. Lastly, the third solution consisted of 832 mg (0.75 M) of ZAD, 229 µl of MEA and 5 ml of 2-methoxyethanol.

The resulting solution was vigorously stirred with the hot-plate magnetic stirrer for the duration of 3 hours at an elevated temperature of 60 °C to

yield viscous, clear and homogenous solution in accordance with the work done by Ohyama et al. [3.15], The solution was then cooled down to room temperature and served as the coating solution.

Initially, 5 drops of the ZnO precursor solution is dropped on the substrate until the surface is covered. The substrate is then rotated using an Oscilla spin coater; the spin coater reached 2000 rpm which is maintained for 40 seconds while continuously dropping 21 drops of the solution.

After coating the substrate, the coated film is placed on a Chemat hot plate furnace that was initially at room temperature while the spin-coated substrate is still wet. The spin-coated substrate is dried by ramping up the temperature to 275°C, with a ramping rate of 25°C/ min. The prepared samples were subsequently removed when the hotplate reached the final temperature. After the completion of the deposition and drying, the resulting film was then left to cool down to ambient temperature.

3.3 Results and discussion

3.3.1 Morphological analysis of the ZnO thin film layers.

It is well known that the performance of OSCs is highly dependent on the surface morphology. Therefore, surface morphologies were observed by a SEM in order to evaluate the effect of the annealing procedures on the ETLs prepared on an ITO substrate. The SEM micrograph of the ZnO thin film is shown in Figure 3.1 and the presence of small tightly packed grains with a relatively smooth and transparent surface can be discerned similar to those observed by Kadem et al. [3.16].

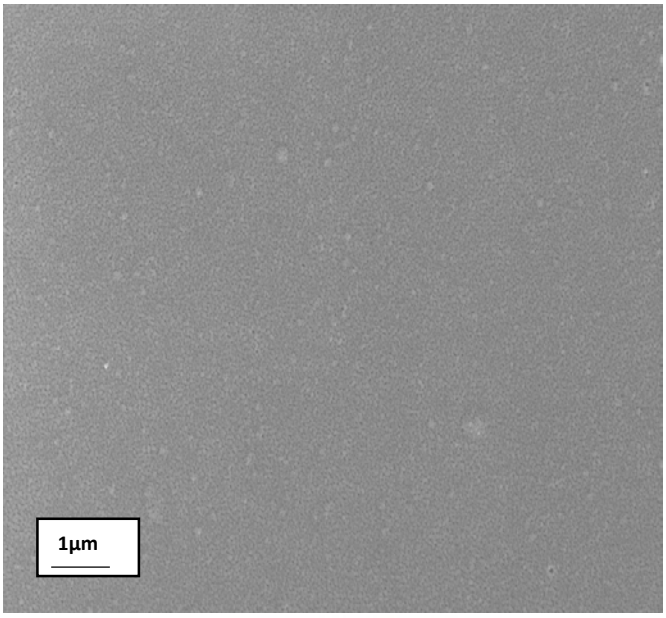

Figure 3. 1: SEM micrograph of ZnO thin film conventionally annealed.

The surface morphologies for the ZnO thin films for the 3 prepared samples reveals a more ridge-like structure, as shown in Figure 3.2. The surface of the spin-coated samples appears to be relatively uniform. It was explained by Sekine et al. [3.17] that due to the slow drying process, the ramp-annealing increased the surface roughness forming ZnO nano-ridges with thickness ranging from 130 nm (0.45 M concertation) to 670 nm (0.75 M concentration). These features are formed during the slow drying due to the structural relaxation and reformation of the particles of ZAD [3.16]. The decomposition of the Zn precursor and evaporation of the solvent occurs at different heating conditions, hence the morphology of the solution-processed ZnO thin film can be sensitive to the rate of annealing as well as the annealing temperature. The formation of different thicknesses in ridges for each sample is also attributed to the concentration of the ZnO precursor material. It is fundamental for the ridges to be as thin as possible to increase the light scattering capability which in turn may enhance photon absorption of the incident light, thus improving the photocurrent of the solar cell [3.18]. The ZnO nano-ridge film in figure 3.2 (c) showed ripple-shaped morphology of thicknesses ranging from 130 nm to 160 nm; due to the formation of these ridges on the ZnO thin film the light–scattering capability

of the thin film is thus enhanced compared to the conventionally annealed ZnO thin film as well as the ramp-annealed ZnO thin films with precursor concentration greater than 0.45 M. The ZnO nano-ridge film thus functions as light trapping structures; enhancing the optical path and photon absorption probability of the incident light and prevent the formation of shunt paths [3.19].

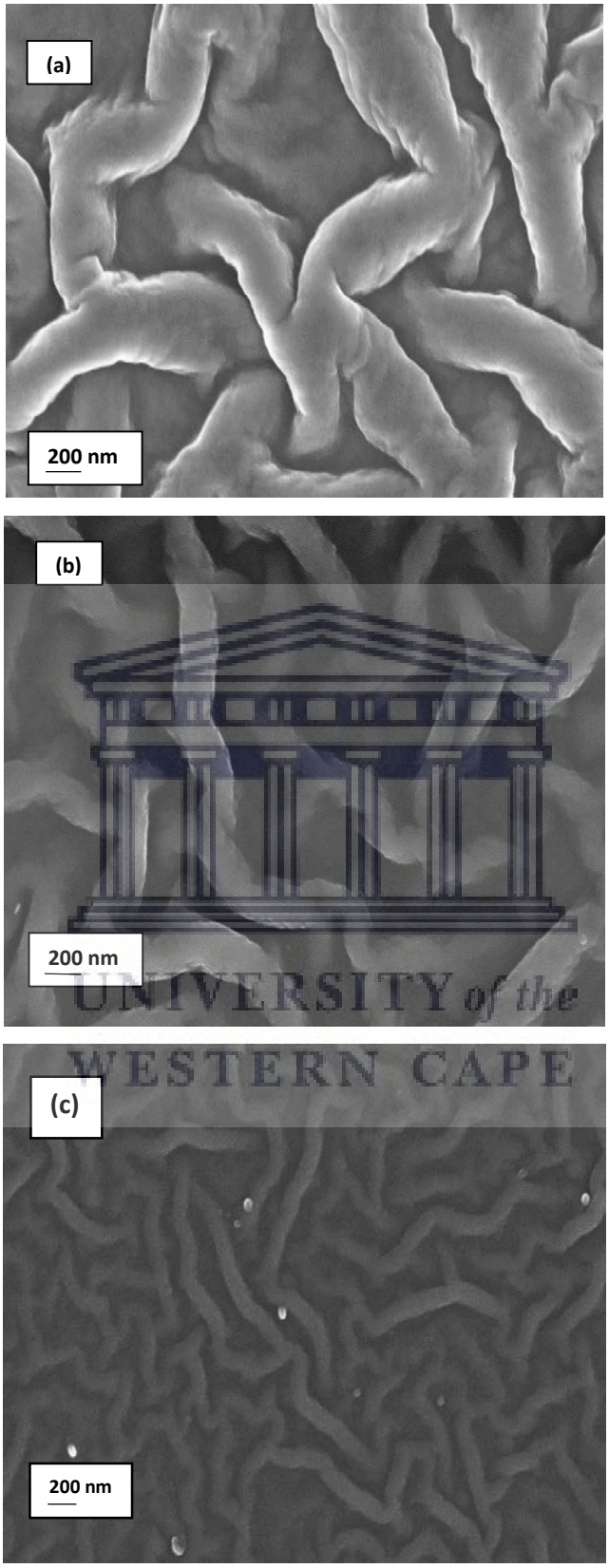

Figure 3. 2: SEM images of ZnO thin films ramp-annealed for different concentration of (a) 0.75 M, (b) 0.60 M and (c) 0.45 M.

EDS analysis was used to confirm the chemical composition of the prepared thin films. The presence of ZnO was observed for both annealing conditions of the ZnO thin films. The energy peaks for the Zn element and oxygen could be seen as presented in Figure 3.3(a) and 3.3(b). The EDS indeed confirmed the purity of ZnO and also confirmed that there were no undesirable chemical residues in the prepared samples. The signal presence of sodium (Na), calcium (Ca), potassium (K), silicon (Si), indium (In) and tin (Sn) were from the substrate. Due to some peak broadening of the In signal in Figure 3.3(b), no potassium signal was detected. The detected carbon is related to the carbon coating sputtered on the surface of the sample in preparation for SEM analysis. The sample has to be carbon coated prior to being inserted into the SEM in order for the sample to be conductive to avoid charge build-up during analysis. In Figure 3.3(a) the signal for sodium was not detected, this might be due to the EDS detection limits of the instrument.

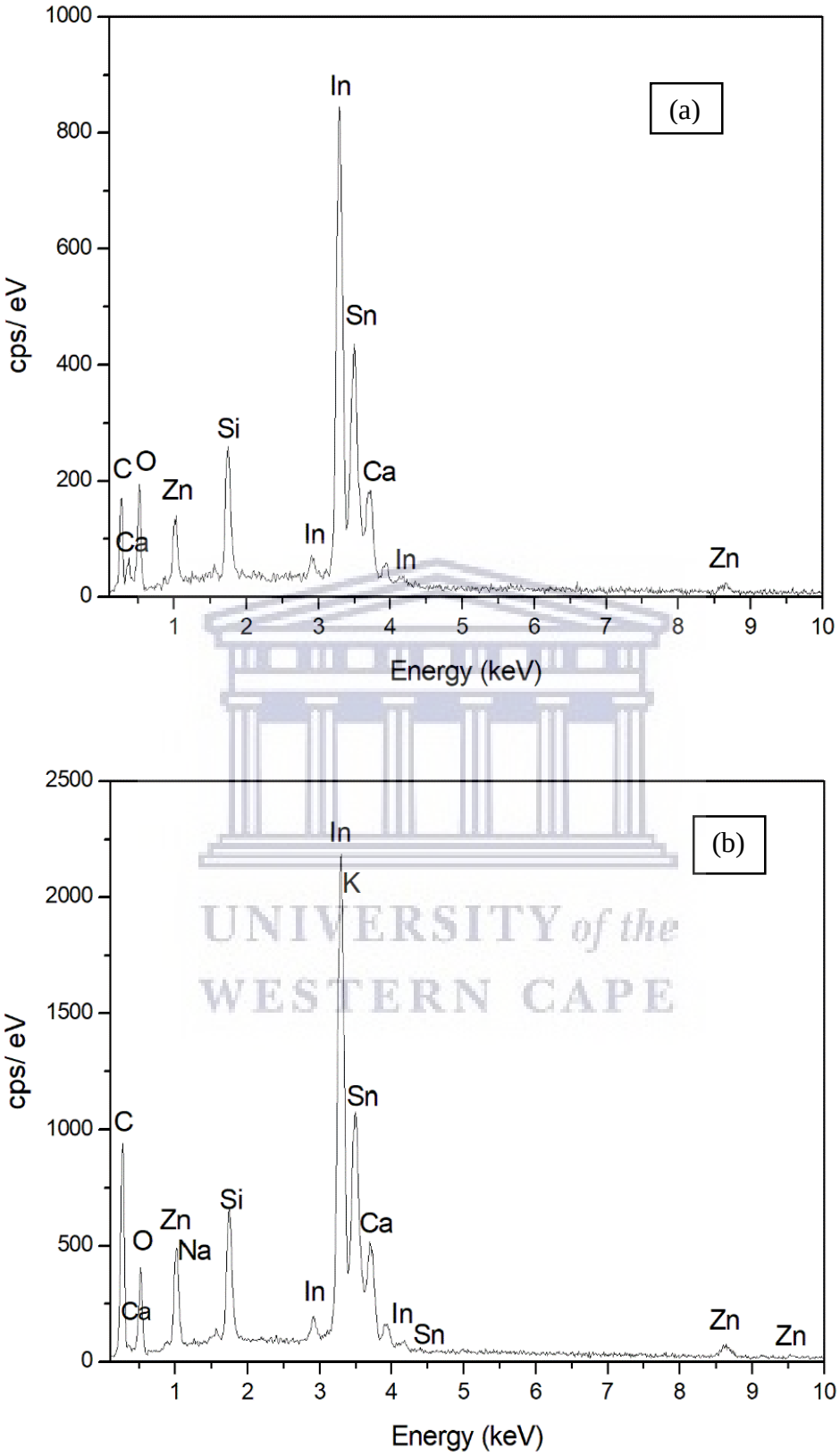

Figure 3. 3: EDS of (a) ZnO thin film conventionally annealed and (b) ZnO thin film ramp-annealed.

3.3.2 Structural analysis of the ZnO thin film layers.

The samples were studied with GIXRD, using an Empyrean diffractometer with Cu Kα radiation (wavelength λ = 1.542Å). The GIXRD patterns were taken for the analysis of the phase and crystalline structure. For the ZnO thin films the GIXRD pattern in Figure 3.4(a), exhibits diffraction peaks (100), (002), (101), (110) and (103) which compares well to the peaks of the reference code (01-079-2205). For the ZnO thin films the GIXRD pattern in Figure 3.4(b), exhibits diffraction peaks (100), (002), (101), (102), (110), (103) and (112) which compares well to the diffraction database peaks of the reference code (01-079-2205). Previous studies revealed that the ZnO thin film has a hexagonal wurtzite crystal structure [3.8]. The analysis of both patterns indicates that the ZnO thin film represented in Figure 3.4 have sharp and narrow diffraction peaks indicating a pure and crystalline material [3.1]. The shaper peaks are due to grain growth with the annealing temperature.

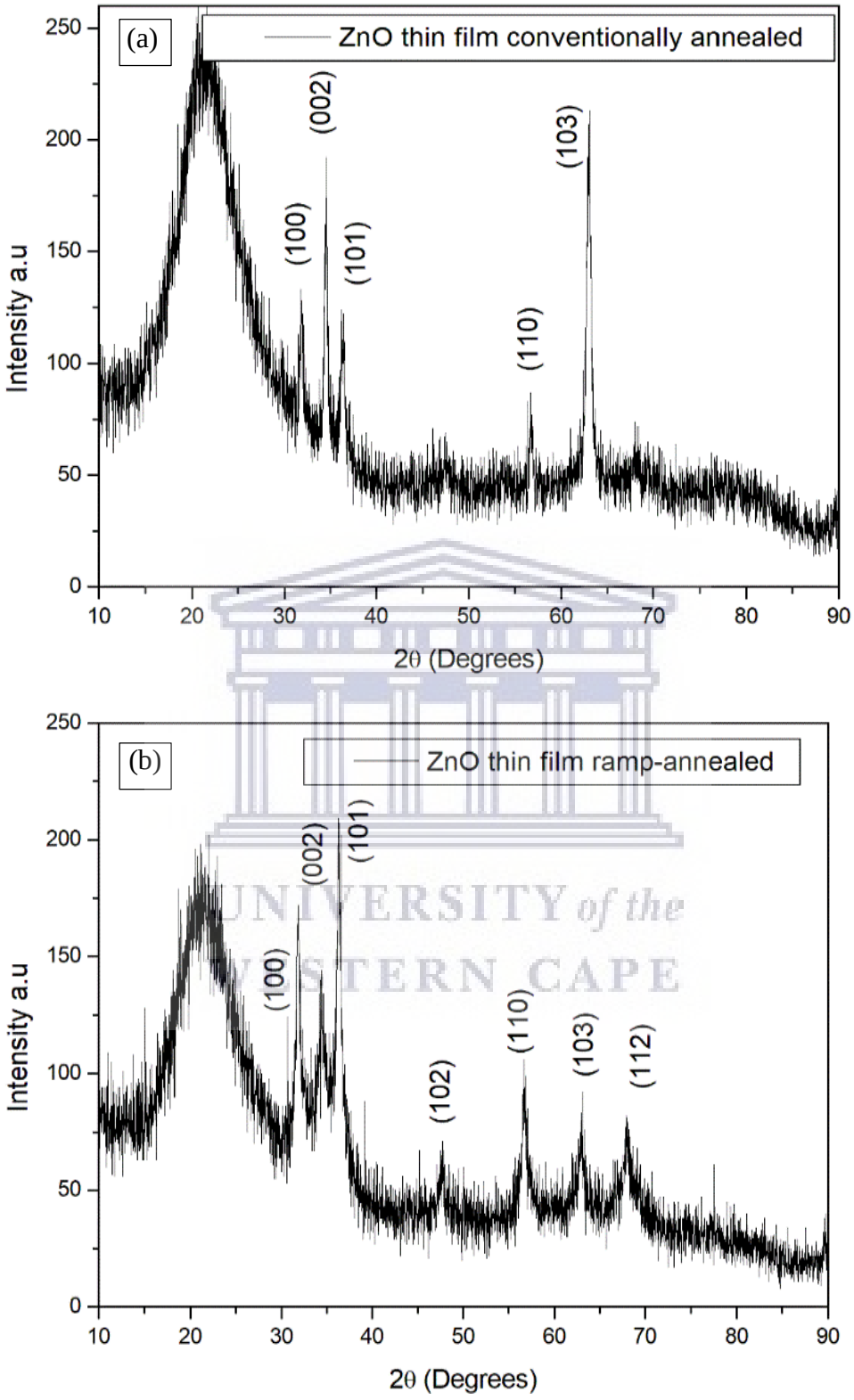

Figure 3. 4: GIXRD of (a) ZnO thin film conventionally annealed and (b) ZnO thin film ramp-annealed.

The average crystallite sizes were calculated using the Debye–Scherrer's formula:

$$D = \frac{K\lambda}{\beta_{hkl}\, Cos\theta}, \qquad (3.1)$$

where D = crystalline size, K = shape factor (0.9), and λ = 1.542Å and β_{hkl} = corrected broadening in radians. By applying the Williamson-Hall (W-H) analysis a plot is drawn with equation (3.2) [3.20, 3.21]:

$$\beta_{hkl} Cos\theta = \frac{K\,\lambda}{D} + 4\varepsilon\, Sin\theta. \qquad (3.2)$$

From the linear fit of the data, the crystalline size D was estimated from the y-intercept, and the strain ε calculated, from the slope of the fit.

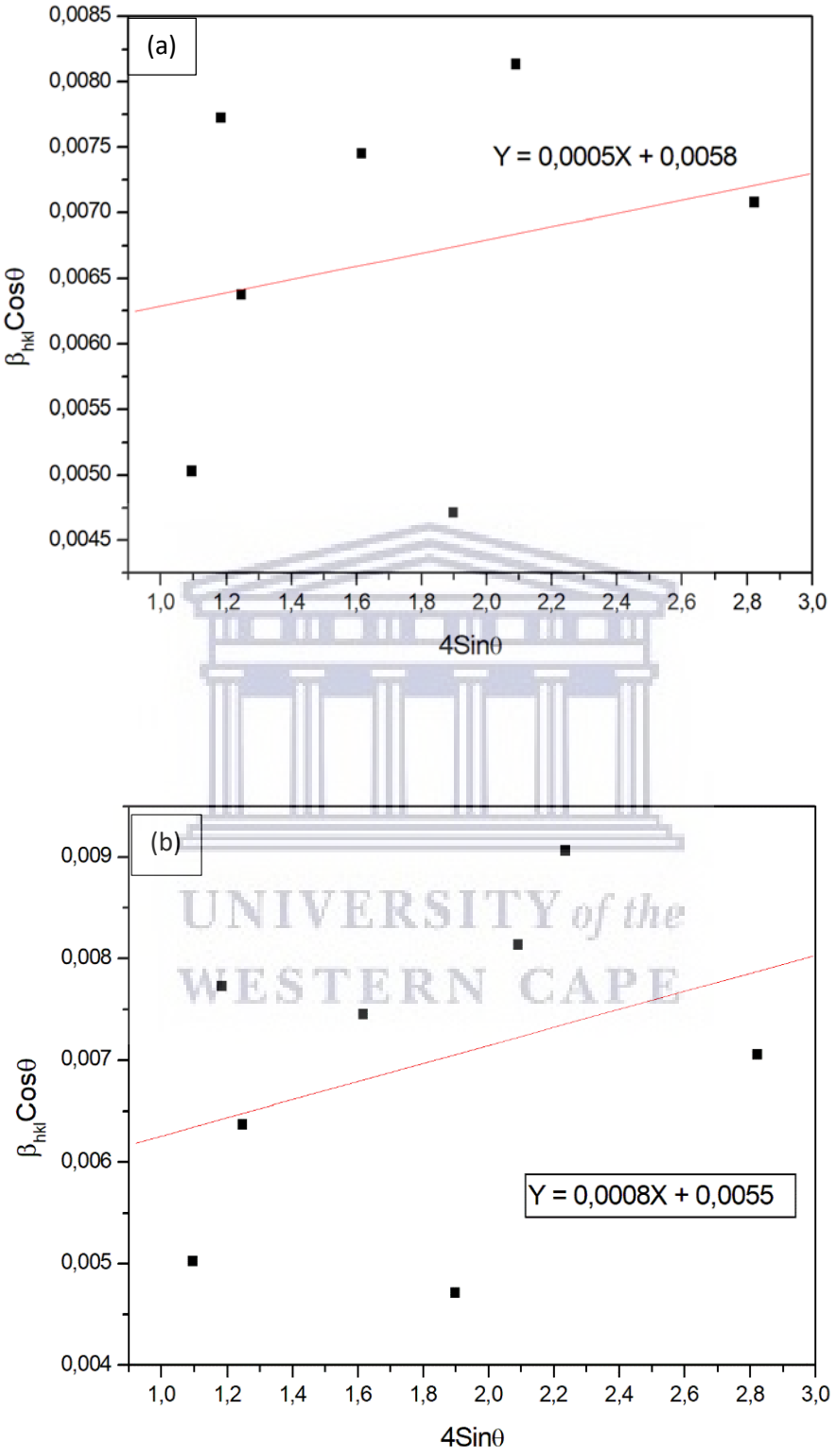

Figure 3. 5: Plot of β_{hkl}Cosθ vs 4Sinθ of ZnO sample (a) ramp-annealed and (b) conventionally annealed.

The crystalline sizes and lattice strain is shown in Table 3.2 below.

Table 3. 2: Crystalline sizes and lattice strain by the Williamson-Hall (W-H) analysis.

	Calculated	
ZnO	**D (nm)**	**ε ($\times 10^{-4}$)**
Conventionally annealed	29.07	9.00
Ramp-annealed	23.91	5.00

It is clear from the table that for conventionally annealed ZnO thin film there is an increase in both grain size and strain compared to the ramp-annealed ZnO thin film. The increased grain growth with temperature contributes to the sharper peaks seen in Figure 3.4(a). As is seen from the W-H analysis, the strain is very small and thus their effect can be negligible on the broadening.

From the interplanar spacing and the set of lattice parameters (hkl), the lattice constants for a hexagonal wurtzite structure a and c was calculated from [3.2]:

$$\frac{1}{d^2} = \frac{4}{3}\left(\frac{h^2+hk+k^2}{a^2}\right) + \frac{l^2}{c^2}. \qquad (3.3)$$

The values of the experimental parameters were compared to the standard parameters as shown in Table 3.3.

Table 3. 3: Summary of the lattice constants of ZnO thin films.

	Calculated		Ref. code: 01-079-2205	
ZnO	**a (Å)**	**c (Å)**	**a (Å)**	**c (Å)**
Conventionally annealed	3.2487	5.2102	3.2501	5.2071
Ramp-annealed	3.2495	4.9537		

The difference in the c-axis lattice constant has to be attributed to the occurrence of stress in the films [3.3].

3.3.3 Chemical analysis of the ZnO thin film layers.

FTIR has been identified as the technique of choice to obtain more insight into the transformation in the chemical structure of ZnO ETLs. The raw (untreated) FTIR transmission spectra of the ZnO thin films prepared via conventional annealing and ramp-annealing are depicted in Figure 3.6. In addition, Table 3.4 gives a summary of the absorption bands for the ZnO thin films. The FTIR measurements were performed on layers spin-coated on silicon substrates.

The first spectrum for the conventionally annealed sample was characteristic of ZnO, see Figure 3.6. After the samples were thermally annealed it could be observed that a conversion from the ZAD precursor to ZnO has occurred since the absorption band in the 400 to 500 cm^{-1} wavelength range were visible; this may be attributed to the stretching modes of Zn-O [3.22]; similarly, for the ramp-annealed sample. The band positions and the number of absorption peaks observed are not only depending on crystalline structure and chemical composition but also on the thin film morphology attributed to the variation in stress acting on the thin films [3.23].

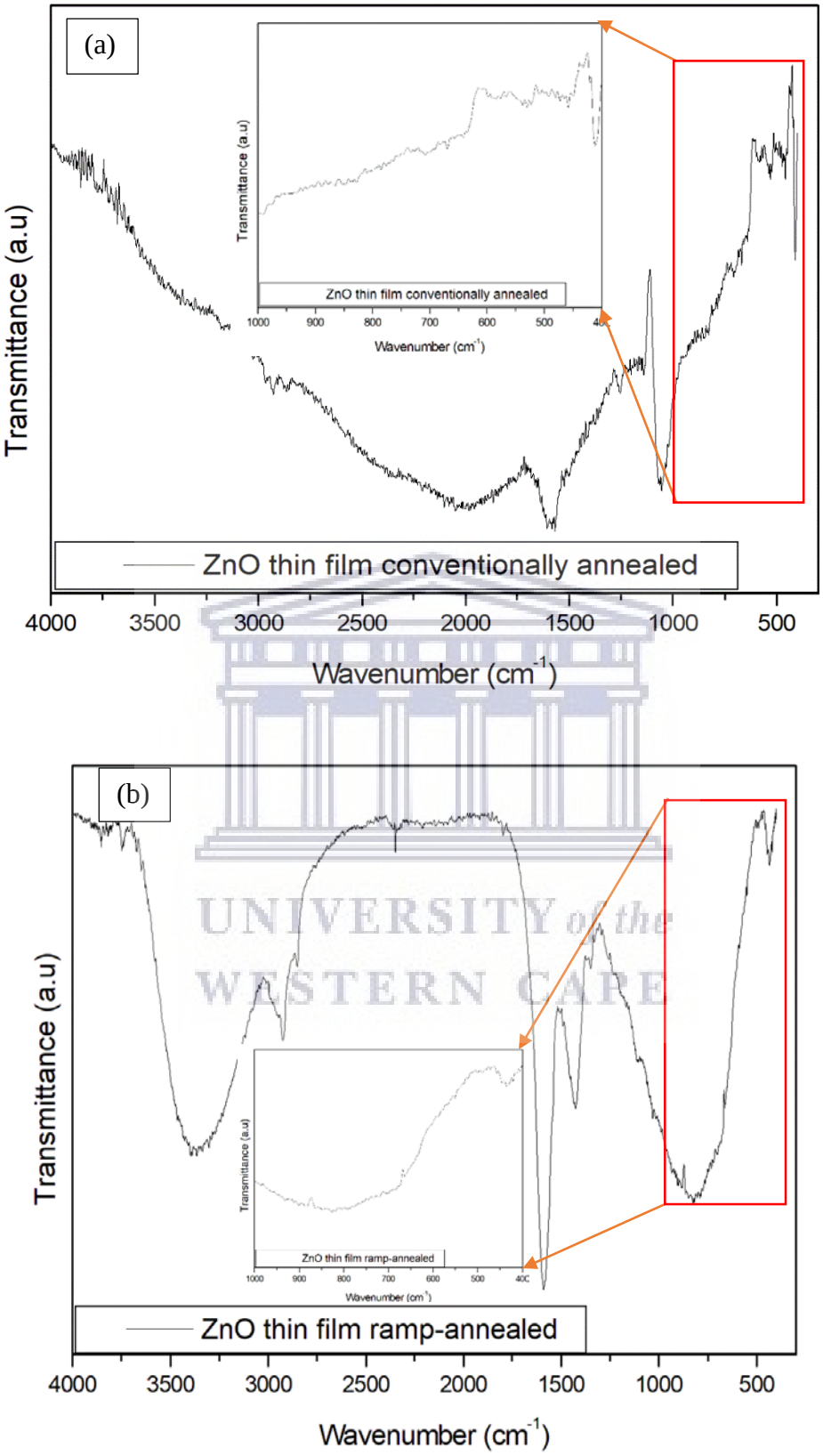

Figure 3. 6: FTIR spectra of ZnO solution spin-coated on Si-substrate (a) conventionally annealed and (b) ramp-annealed ZnO thin films.

Table 3.4 shows a summary of the absorption bands for the ZnO thin films. The IR spectra for the conventionally annealed sample shows a characteristic ZnO absorption feature at 409.98 cm^{-1} (see inset of Figure 3.6(a)) corresponding to the wurtzite structure which is theoretically confirmed [3.23], whereas the ramp-annealed sample shows band at 436.66 cm^{-1} which corresponds to Zn-O bonds [3.24]. The band attributed to ZnO exhibits a more intense band for the conventionally annealed ZnO thin film also showing improved crystallinity. The rest of the peaks seem to dominate compared to peaks observed for the ZnO information. The peak around 1053.43 cm^{-1} for the ramp-annealed sample is assigned to the C-O stretching vibrations [3.25]. The bands in the spectral range from 1423.91 cm^{-1} – 1586.77 cm^{-1} are attributed to C=O stretching mode [3.26]. The peaks around 2913.46 cm^{-1} and 2919.38 cm^{-1} are due to the existence of C-H bonds in the thin film [3.27]. Lastly we observe O-H stretching bonds around 826.19 cm^{-1} and 3373.60 cm^{-1} [3.28, 3.29]. It can be noted that the O-H stretching bond is not visible for the conventionally annealed ZnO thin film. Also, it is evident that the conventionally annealed thin film shows weaker absorption bands for the C=O stretching mode and the C-H bonds. These are vibrations due to organic residuals and water which becomes less apparent due to higher temperature annealing.

Table 3. 4: FTIR absorption bands and assignments of ZnO.

Peak wavenumber (cm^{-1})	**Assignment**
409.98	Wurtzite ZnO
436.66, 826.19	Zn-O stretching mode
1053.43	C-O stretching mode
1423.91	C=O stretching mode
1585.53, 1586.77	O-H bending mode
2913.46, 2919.38	C-H stretching modes
3373.60	O-H stretching mode

Evidently the FTIR spectroscopy measurements confirms that the ZnO precursor was completely converted into crystalline ZnO; supporting the results obtained from the XRD analysis.

3.3.4 Optical properties of the ZnO thin film layers.

Generally, the high optical transmittance of the ZnO layers is suitable for the preparation of organic solar cells. Since the photoactive layer of the P3HT: PCBM blend exhibits good absorption in the visible range the optical properties of the ZnO ETL is crucial to ensure that incoming light crossing the ETL is absorbed in the photoactive layer. The transparency of the ZnO ETL layers on glass/ITO were thus probed by UV-vis spectroscopy. The transmittance of the two metal oxide thin films acting as ETLs were measured and their spectra are shown in Figure 3.7. Both thin films show good average transparency in the visible range, where the highest transmittance is for the conventionally annealed ZnO thin film. The ZnO ramp-annealed thin film is less transparent with respect to the conventional annealed thin film which is consistent with the white foggy appearance of the thin film which shows a light scattering effect. The other difference is the shift in the absorption edge for the ZnO thin film for the two contrasting annealing methods. It is well known that the absorption edge is closely related to the properties of the material. Generally, a narrower band gap for metal oxides indicates a higher degree of crystallinity [3.30], which may be the case for our ZnO thin film when it is conventionally annealed compared to ramp-annealed.

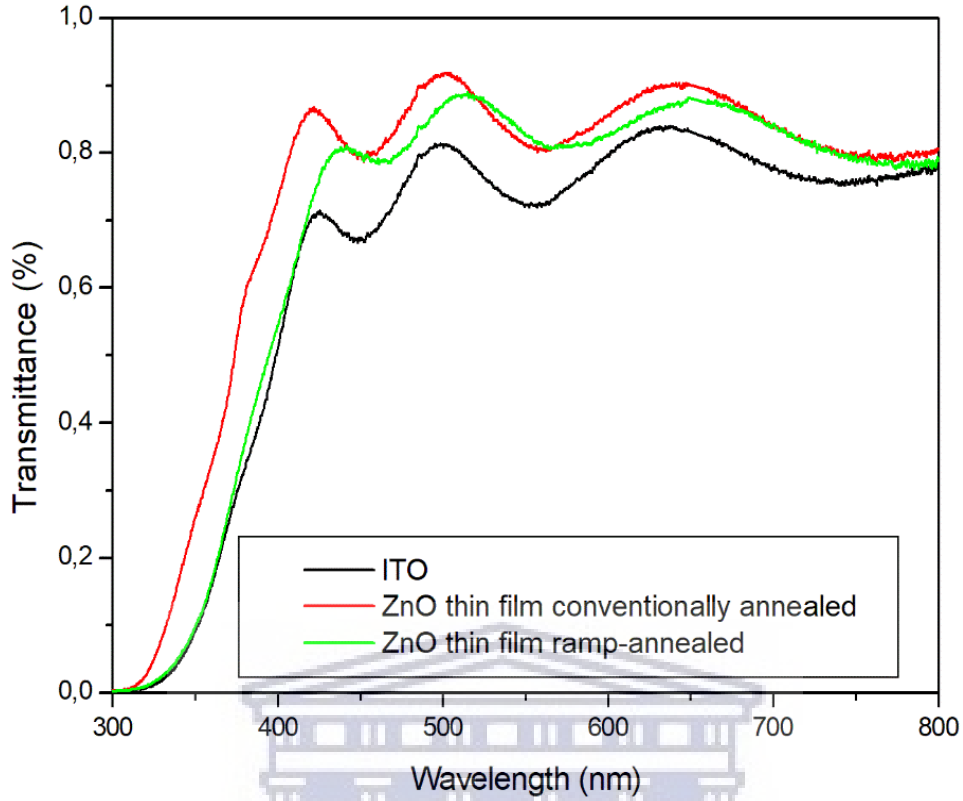

Figure 3. 7: Transmission spectra of ZnO thin film conventionally annealed and ZnO thin film ramp-annealed on ITO substrate and bare ITO on the glass.

Absorbance measured from the glass side of the sample with the active layer deposited on the ETLs indicates that the polymer films with the ramp-annealed ZnO and thin film showed increased absorption in the visible range of the spectrum, which is indicated with the light blue curve in Figure 3.8. This measurement was performed to probe whether the active layer behaves differently for the different ETLs when incident light crosses the ETL and is absorbed by the active layer.

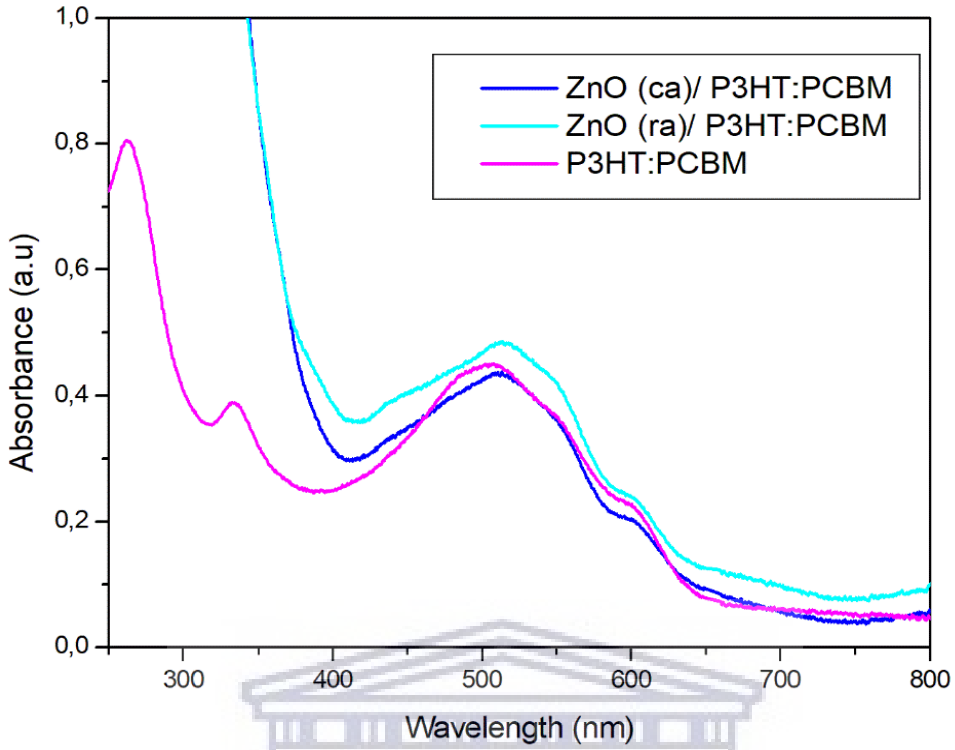

Figure 3. 8: Absorbance spectra of the active layer on ZnO layers (ca – conventionally annealed, ra – ramp-annealed) from the glass side.

The optical band gap of the thin films was evaluated from the transmission spectra of the thin films coated on quartz glass substrates. Then, by extrapolating the linear portion of the curve presented by $(\alpha h\upsilon)^2$ as a function of $(h\upsilon)$ one can estimate the optical band E_g (Tauc's model [3.31]) from

$$(\alpha h\upsilon)^2 = A\,(h\upsilon - E_g), \qquad (3.4)$$

where A is a constant independent of energy and h is Planck's constant, $h\upsilon$ is the photon energy and α is the absorption coefficient. A plot of $(\alpha h\upsilon)^2$ vs $(h\upsilon)$ yields a good straight-line fit to the absorption edge and provides the optical band gap from the $h\upsilon$ axis.

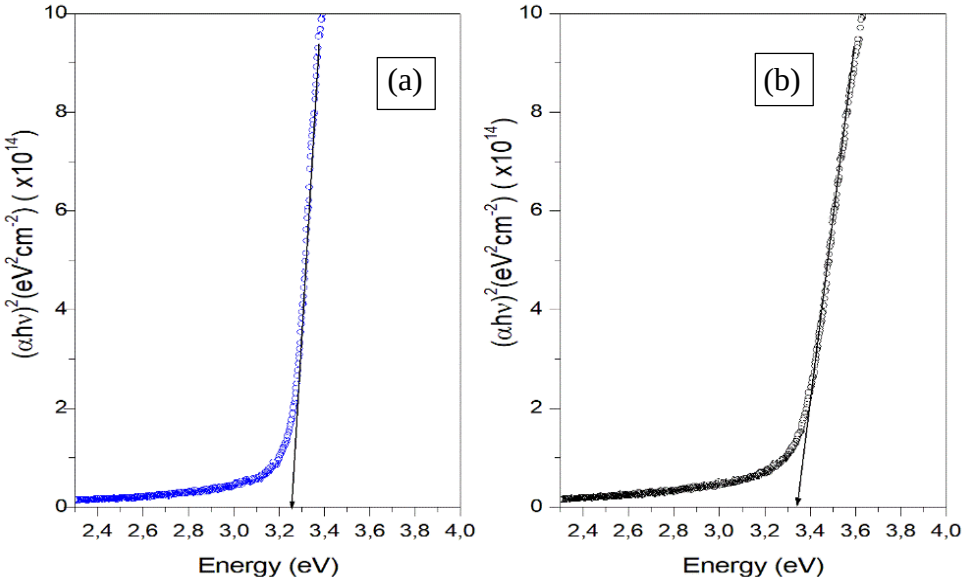

Figure 3. 9: $(\alpha h\upsilon)^2$ versus photon energy ($h\upsilon$) plot of (a) ZnO thin film conventionally annealed and (b) ZnO thin film ramp-annealed.

A good linear relationship was obtained and fitted by means of equation (3.4); the results are shown in Figure 3.9. The optical band gap for ZnO is 3.25eV and 3.35 eV, respectively, which indicates a direct band gap. The band gap in the present study is in fair agreement with the E_g value of bulk ZnO of 3.37 eV [3.32]. The discrepancy in the band gap values for ZnO thin films could come from the different film preparation methods used or variations in annealing type and annealing temperature [3.33], yielding different microstructures [3.34]. The optical band gap for both ZnO thin films red shifted from 3.37 eV to 3.35 eV and 3.25 eV for the ramp and conventionally annealed ZnO thin films, respectively. This red shift is due to decreasing quantum confinement with increasing crystallite size as temperature increases [3.35]. The changes in the optical band gaps with respect to the ZnO morphology leads to the band gaps smaller than its bulk value. Overall, the modification of the band gap can be attributed to improved crystallinity of the conventionally annealed thin film, due to reduction of strain and defects, as well as crystallite sizes [3.36]

Reflectance spectroscopy was used to probe the ZnO thin films; specifically, diffuse reflectance. An integrating sphere in combination with a spectrometer was used to capture and measure the reflected and scattered light from the surface of each sample. On a rough and irregular surface, the collection of the back reflected and diffusely scattered light are commonly collected. Figure 3.10 presents the diffuse reflectance plots for the conventionally annealed and ramp-annealed ZnO thin film. Evidently, the diffuse reflectance for the conventionally annealed ZnO thin film is much less than that for the ramp-annealed ZnO thin film. We observed that the maximum diffuse reflectance is largely dependent on the roughness of the thin film. This directly relates to the differences in the growth morphologies observed in the SEM analysis. Decreased roughness leads to less diffuse reflection.

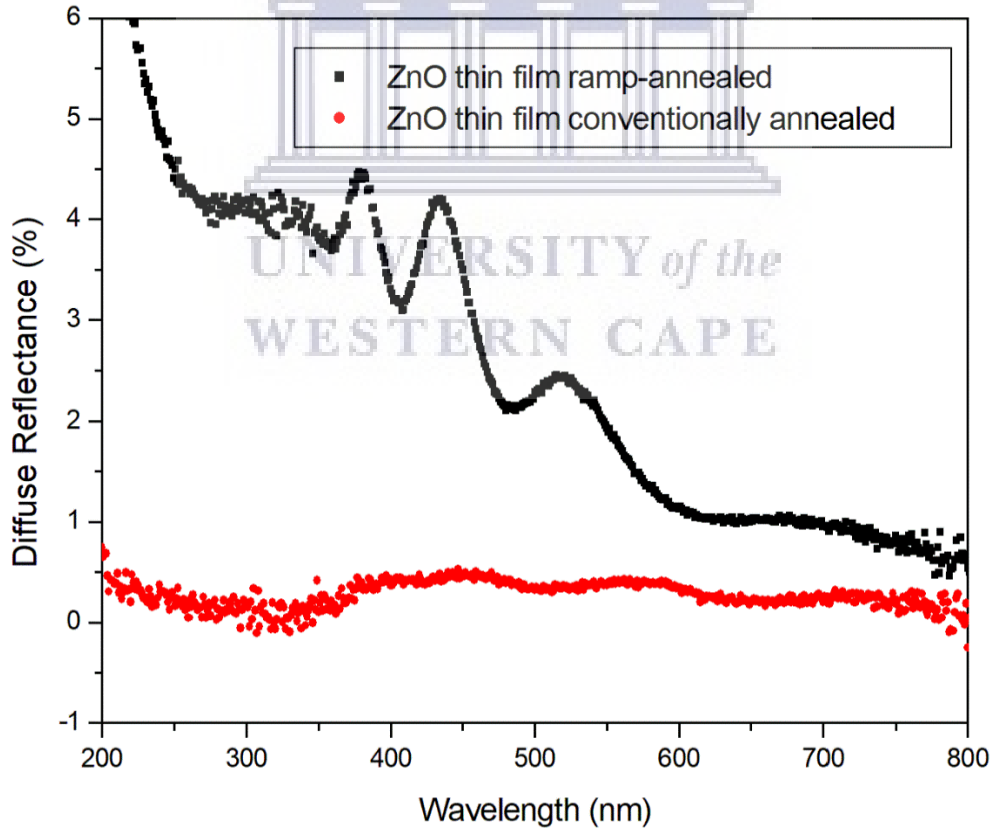

Figure 3. 10: Diffuse reflection spectroscopy of the ZnO thin films.

3.4 Conclusion

The structural and optical properties of ZnO were investigated using, high-resolution scanning electron microscopy (HR-SEM), x-ray diffraction (XRD) and ultraviolet-visible (UV-vis) spectroscopy.

The SEM results have shown that the ridge structures are dependent on the concentration of the precursor materials. The morphology of the thin films prepared using a sol-gel method can be easily controlled through adjusting the concentration of the precursor solution as well as the post thermal treatment. XRD results confirmed that the thin films are ZnO without any impurities and have a hexagonal wurtzite structure. UV-vis absorption spectra showed that the absorption band of the ZnO is around 320 - 360 nm, which red-shifted relative to the bulk exciton absorption (373 nm). This red-shift is due to film strain during the annealing procedure. The optical properties of ZnO thin films make it suitable to serve as ETL in an inverted OSC device. Furthermore, electrical characterization will be explored in the operation of inverted solar cells with an ITO/ ZnO in chapter 5.

References

[3.1] Kamaruddin, S.A., Chan, K.Y., Yow, H.K., Sahdan, M.Z., Saim, H. and Knipp, D., 2011. Zinc oxide films prepared by sol-gel spin coating technique. *Applied Physics A, 104*(1), pp.263-268.

[3.2] Dahnoun, M., Attaf, A., Saidi, H., Yahia, A. and Khelifi, C., 2017. Structural, optical and electrical properties of zinc oxide thin films deposited by sol-gel spin coating technique. *Optik, 134*, pp.53-59.

[3.3] Zhang, Y., Lin, B., Fu, Z., Liu, C. and Han, W., 2006. Strong ultraviolet emission and rectifying the behavior of nanocrystalline ZnO films. *Optical Materials, 28*(10), pp.1192-1196.

[3.4] Li, Y., Xu, L., Li, X., Shen, X. and Wang, A., 2010. Effect of ageing time of ZnO sol on the structural and optical properties of ZnO thin films prepared by sol-gel method. *Applied Surface Science, 256*(14), pp.4543-4547.

[3.5] Chiou, W.T., Wu, W.Y. and Ting, J.M., 2003. Growth of single-crystal ZnO nanowires using sputter deposition. *Diamond and Related Materials, 12*(10-11), pp.1841-1844.

[3.6] Purica, M., Budianu, E., Rusu, E., Danila, M. and Gavrila, R., 2002. Optical and structural investigation of ZnO thin films prepared by chemical vapor deposition (CVD). *Thin Solid Films, 403*, pp.485-488.

[3.7] Ohtomo, A., Kawasaki, M., Sakurai, Y., Yoshida, Y., Koinuma, H., Yu, P., Tang, Z.K., Wong, G.K. and Segawa, Y., 1998. Room temperature ultraviolet laser emission from ZnO nanocrystal thin

films grown by laser MBE. *Materials Science and Engineering: B*, *54*(1-2), pp.24-28.

[3.8] Andrade, E. and Miki-Yoshida, M., 1999. Growth, structure and optical characterization of high-quality ZnO thin films obtained by spray pyrolysis. *Thin Solid Films*, *350*(1-2), pp.192-202.

[3.9] Ivanova, T., Harizanova, A., Koutzarova, T. and Vertruyen, B., 2010. Study of ZnO sol-gel films: effect of annealing. *Materials Letters*, *64*(10), pp.1147-1149.

[3.10] Ali, M.M. and Meshari, S.M., 2014. Structural and optical characterization of ZnO thin films by sol-gel technique. *Journal of Basrah Researches (Sciences)*, *40*(1A), pp.39-48.

[3.11] Park, H.J., Lee, K.H., Kumar, B., Shin, K.S., Jeong, S.W. and Kim, S.W., 2010. Inverted organic solar cells with ZnO thin films prepared by sol-gel method. *Journal of Nanoelectronics and Optoelectronics*, *5*(2), pp.135-138.

[3.12] Barrera, D., Lee, Y.J. and Hsu, J.W., 2014. Influence of ZnO sol-gel electron transport layer processing on BHJ active layer morphology and OPV performance. *Solar Energy Materials and Solar Cells*, *125*, pp.27-32.

[3.13] Kim, Y. and Leem, J.Y., 2016. Effects of Precursor Concentration on Structural and Optical Properties of ZnO Thin Films Grown on Muscovite Mica Substrates by Sol–Gel Spin-Coating. Journal of nanoscience and nanotechnology, 16(5), pp.5186-5189.

[3.14] Kamaruddin, S.A., Chan, K.Y., Yow, H.K., Sahdan, M.Z., Saim, H. and Knipp, D., 2011. Zinc oxide films prepared by sol-gel spin coating technique. Applied Physics A, 104(1), pp.263-268.

[3.15] Ohyama, M., Kouzuka, H. and Yoko, T., 1997. Sol-gel preparation of ZnO films with extremely preferred orientation along (002) plane from zinc acetate solution. Thin solid films, 306(1), pp.78-85.

[3.16] Kadem, B., Banimuslem, H.A. and Hassan, A., 2017. Modification of morphological and optical properties of ZnO thin film. Karbala International Journal of Modern Science, 3(2), pp.103-110.

[3.17] Sekine, N., Chou, C.H., Kwan, W.L. and Yang, Y., 2009. ZnO nano-ridge structure and its application in inverted polymer solar cell. Organic Electronics, 10(8), pp.1473-1477.

[3.18] Tsai, C.Y., Lai, J.D., Feng, S.W., Huang, C.J., Chen, C.H., Yang, F.W., Wang, H.C. and Tu, L.W., 2017. Growth and characterization of textured well-faceted ZnO on planar Si (100), planar Si (111), and textured Si (100) substrates for solar cell applications. Beilstein journal of nanotechnology, 8(1), pp.1939-1945.

[3.19] Lim, D.C., Shim, W.H., Kim, K.D., Seo, H.O., Lim, J.H., Jeong, Y., Kim, Y.D. and Lee, K.H., 2011. Spontaneous formation of nanoripples on the surface of ZnO thin films as a hole-blocking layer of inverted organic solar cells. Solar Energy Materials and Solar Cells, 95(11), pp.3036-3040.

[3.20] Mote, V.D., Purushotham, Y. and Dole, B.N., 2012. Williamson-Hall analysis in estimation of lattice strain in nanometer-sized ZnO particles. Journal of Theoretical and Applied Physics, 6(1), p.6.

[3.21] Tan, S.T., Chen, B.J., Sun, X.W., Fan, W.J., Kwok, H.S., Zhang, X.H. and Chua, S.J., 2005. The blueshift of optical band gap in ZnO thin films grown by metal-organic chemical-vapor deposition. Journal of Applied Physics, 98(1), p.013505.

[3.22] Li, X., He, G., Xiao, G., Liu, H. and Wang, M., 2009. Synthesis and morphology control of ZnO nanostructures in microemulsions. Journal of Colloid and Interface Science, 333(2), pp.465-473.

[3.23] Babu, K. Sowri, A. Ramachandra Reddy, Ch Sujatha, K. Venugopal Reddy, and A. N. Mallika. "Synthesis and optical characterization of porous ZnO." Journal of Advanced Ceramics 2, no. 3 (2013): 260-265.

[3.24] Kooti, M. and Naghdi Sedeh, A., 2012. Microwave-assisted combustion synthesis of ZnO nanoparticles. Journal of Chemistry, 2013.

[3.25] Hsieh, C.H., 2007. Spherical zinc oxide nano particles from zinc acetate in the precipitation method. Journal of the Chinese Chemical Society, 54(1), pp.31-34.

[3.26] Kumar, K.B. and Raji, P., 2011. Synthesis and characterization of nano zinc oxide by sol gel spin coating. Recent research in science and technology, 3(3).

[3.27] Nimbalkar, A.R. and Patil, M.G., 2017. Synthesis of ZnO thin film by sol-gel spin coating technique for H2S gas sensing application. Physica B: Condensed Matter, 527, pp.7-15.

[3.28] Prkić, A., Vukušić, T., Mitar, I., Giljanović, J., Sokol, V., Bošković, P., Jakić, M. and Sedlar, A., 2019. New sensor based on AgCl

containing Iron Oxide or Zinc Oxide Nanoparticles for Chloride Determination. International Journal of Electrochemical Science, 14(1), pp.861-874.

[3.29] Khan, M., Naqvi, A.H. and Ahmad, M., 2015. Comparative study of the cytotoxic and genotoxic potentials of zinc oxide and titanium dioxide nanoparticles. Toxicology reports, 2, pp.765-774.

[3.30] Lin, Z., Chang, J., Jiang, C., Zhang, J., Wu, J. and Zhu, C., 2014. Enhanced inverted organic solar cell performance by post-treatments of solution-processed ZnO buffer layers. Rsc Advances, 4(13), pp.6646-6651.

[3.31] Amari, R., Mahroug, A., Boukhari, A., Deghfel, B. and Selmi, N., 2018. Structural, Optical and Luminescence Properties of ZnO Thin Films Prepared by Sol-Gel Spin-Coating Method: Effect of Precursor Concentration. Chinese Physics Letters, 35(1), p.016801.

[3.32] Janotti, A. and Van de Walle, C.G., 2009. Fundamentals of zinc oxide as a semiconductor. Reports on progress in physics, 72(12), p.126501.

[3.33] Tsay, C.Y., Fan, K.S., Wang, Y.W., Chang, C.J., Tseng, Y.K. and Lin, C.K., 2010. Transparent semiconductor zinc oxide thin films deposited on glass substrates by sol-gel process. Ceramics International, 36(6), pp.1791-1795.

[3.34] Xue, S.W., Zu, X.T., Zhou, W.L., Deng, H.X., Xiang, X., Zhang, L. and Deng, H., 2008. Effects of post-thermal annealing on the optical constants of ZnO thin film. Journal of Alloys and Compounds, 448(1-2), pp.21-26.

[3.35] Soosen Samuel, M., Lekshmi Bose, and K. C. George. "Optical properties of ZnO nanoparticles." Academic Review (2009): 57-65.

[3.36] Soleimanian, V. and Aghdaee, S.R., 2011. The influence of annealing temperature on the slip plane activity and optical properties of nanostructured ZnO films. Applied Surface Science, 258(4), pp.1495-1504.

CHAPTER FOUR

4 Investigation of the influence of annealing treatment on the morphology, structural and optical properties of Titanium Dioxide (TiO_2) thin film layers.

4.1 Introduction

This chapter provides experimental findings for the TiO_2 thin films prepared with conventionally annealed and ramp-annealed treatments. Initially, these conditions are investigated to observe and control the morphological induced changes; here different nanostructures are observed. These differences observed on the surface of the TiO_2 thin films from conventionally annealed and ramp-annealed treatments are characterized to study their influences.

TiO_2 is an attractive n-type semiconducting material, with a variety of applications such as gas sensors, dye-sensitized solar cells, photocatalysis, photoelectrochemical cells, self-cleaning glasses, paints and wave guiding [4.1, 4.2]. Many of these important applications of TiO_2 depends on its unique structural, optical and electrical properties owing to the biocompatibility, chemical and physical stability, non-toxicity and long term photo-stability [4.1-4.3]. TiO_2 possesses attractive properties; some of them are high refractive index, high dielectric constant and high transparency to the visible and near-infrared light [4.3]. There are several factors such as particle size, crystallinity and morphology which determine important properties in the performance of TiO_2 [4.4, 4.5].

TiO_2 exists in three crystalline forms which are anatase (tetragonal), rutile (tetragonal) and brookite (orthorhombic) phases. Due to these different

phases, TiO_2 exhibit a wide band gap (3-3.3 eV) [4.6, 4.7]. Moreover, thin films of TiO_2 can be prepared by various techniques; amongst them are sputtering [4.8], chemical vapour deposition (CVD) [4.9], molecular beam epitaxy [4.10], hydrothermal [4.11] and sol-gel process [4.4-4.6].

The properties of most metal oxides depend on the chemical synthesis method employed for fabrication. Thus, the material can be modified for the final application. The sol-gel technique has emerged as a new processing route due to its many advantages like, ease to obtain high-quality thin films and homogenous nanostructures [4.5, 4.12, 4.13]. However, the quality of the TiO_2 thin film is still affected by many factors [4.14]; hence in this work the objective of the investigation is to study the effects of the concentration on the thin film properties by preparing it using the sol-gel technique in order to deposit the precursor material of TiO_2 on ITO substrates, followed by two different post-annealing treatments. The influence of the nanostructured thin films will be investigated by utilizing them for application in organic/ hybrid OSC to establish to which extent the device efficiency is affected.

4.2 Experimental details

4.2.1 Preparation of TiO_2 thin film by conventional annealing.

The TiO_2 sol-gel was prepared using Titanium (IV) Isopropoxide (TTIP), Acetic Acid (AA) and Ethanol (all from Sigma Aldrich) as the starting material, catalyst and solvent, respectively.

TiO_2 thin films based on the conventional annealing have attracted much attention as a promising ETL since it has good transparency in the whole visible region. Post-annealing treatment is required to achieve optimum quality and morphology after spin coating. In this work the traditional compact TiO_2 thin film was prepared by adopting a procedure by Senthil et

al. and Ranganayaki et al. [4.13, 4.16]. Traditionally the compact TiO_2 thin films are prepared using the following procedure. Initially, 1.5 ml of TTIP is dissolved into 10 ml of ethanol and 0.1 ml of AA added dropwise into the mixture at room temperature. The mixed solution is magnetically stirred for 4 hours at room temperature to obtain a transparent solution. The final composition of the solution in volume ratio is TTIP:Ethanol:AA = 1:10:0.1 ml. This mixture served as the coating solution.

After cleaning the substrate using the sample preparation method discussed in chapter 3.2.1, a volume of 200 µl of the resulting solution is carefully dropped on top of the ITO substrate until the surface is covered. The substrate is then rotated using an Ossila spin coater; the spin coater reached 4000 rpm which is maintained for 40 s.

After coating, the coated film is removed and dried at 100°C for 10 min on a pre-heated Chemat hot plate. Thereafter, the resulting film is inserted into a tube furnace and annealed in air at 500°C for 1 hour. The tube furnace was ramped up to 500 °C at a ramping rate of 10 °C/ min, where it dwelled for 1 hour before being cooled down to ambient temperature.

4.2.2 Preparation of TiO_2 thin film by ramp-annealing.

In the previous chapter a strong dependence of the ZnO thin film properties could be attributed to the ramping rate with which the film was annealed. Here in this chapter we replaced the ZnO thin film with a TiO_2 thin film to investigate whether the same effects can improve the conversion efficiency, thus enhancing the overall efficiency. In order to achieve the aforementioned, we changed from the traditional furnace annealing to the controlled ramp-annealing procedure for the TiO_2 thin film preparation. The morphology of TiO_2 the thin was also manipulated using different solution concentrations. The TiO_2 thin films were fabricated using TTIP as a precursor material. The concentration of the prepared solution was prepared

for different proportions of AA. Initially, TTIP is dissolved into ethanol and then AA was added dropwise into the mixture at room temperature. The final composition of TTIP:Ethanol:AA for the precursor solution is summarized in Table 4.1. The first solution was prepared by adding 1.5 ml of TTIP into 10 ml of ethanol and then adding 0.1 ml of AA to make the final solution. The second solution consisted of a volume ratio of 1.5:10:0.2 ml.

Table 4. 1: Chemical composition for the TiO_2 precursor solution with different concentration determined by various volumes of acetic acid.

TTIP (ml)	**AA (ml)**	**Ethanol (ml)**
1.5	0.1	10
1.5	0.2	10

Both of the mixed solutions were magnetically stirred for 4 hours at room temperature to obtain a transparent solution. This mixture served as the coating solution. Then the precursor solution is carefully pipetted on top of an ITO substrate initially dropping 5 drops on the surface until it is covered. The substrate is then rotated using an Ossila spin coater; the spin coater reached 2000 rpm which is maintained for 40 s while continuously dropping 21 drops of the precursor solution.

After coating, the coated film is placed onto the Chemat hot plate and dried by ramping up it from room temperature to 275 °C, with a ramping rate of 25 °C / min. When the hot plate reaches the desired temperature of 275 °C, the resulting film is immediately removed and left to cool down to ambient temperature. The low-temperature procedure used minimizes inter-diffusion between the Ti (titanium) and the In (indium) at the ITO/TiO_2 interface; maintaining the conductivity of the ITO substrate [4.17].

4.3 Results and discussion

4.3.1 Morphological analysis of the TiO_2 thin film layers.

SEM is a very important tool to study the surface morphology and the crystals of sample since the organic solar cell performance is highly dependent on the surface morphology. Therefore, SEM was used to investigate the effect of the annealing procedures on the ETLs prepared on ITO substrate. The conventionally annealed TiO_2 ETL shows a crack-free film with superior surface flatness, well defined fine structure and small grains as shown in Figure 4.1, covering the whole surface without any visible pin holes.

Figure 4. 1: SEM micrograph of the TiO_2 thin film conventionally annealed.

From Figure 4.2 we surmise that TiO_2 mesoporous structures were obtained during the ramp-annealed process. Mesoporosity refers to sponge-like structures with partially interconnected pores formed by the accumulation of particles. We surmise that the slow evaporation of the TiO_2 solution results in self-assembly and structural transformation, leading to the formation of porous structures. Light diffusion efficiencies within the interconnected

mesopore network is thus enhanced due to the multiple scattering of light in the interpenetrated mesopores [4.18]. Mesoporous TiO_2 thin films with different morphologies by adjusting the solution concentration are shown in Figure 4.2. Different concentrations (a) 0.1 ml and (b) 0.2 ml are deposited by spin coating. Both samples were ramp annealed to 275 °C. From Figure 4.2(a) and (b) it can be seen that the TiO_2 thin film has a morphology with porous structures covering the substrate. It was found that the thin film in Figure 4.2(a) is denser due to the concentration of acetic acid. The size of the pores in Figure 4.2 (a) ranges from 100 nm to 600 nm. The pore size of the TiO_2 thin film significantly increases in diameter reaching approximate sizes up to 1µm in diameter due to conventional annealing. The porous nature of the thin film is thus proportional to the concentration of the precursor solution. The high porosity and high pore volume is favourable to improve light absorption. Larger pore sizes provide a more favourable pathway for the exciton diffusion at the interface when applied to OPVs which contributes toward enhanced efficiency [4.19].

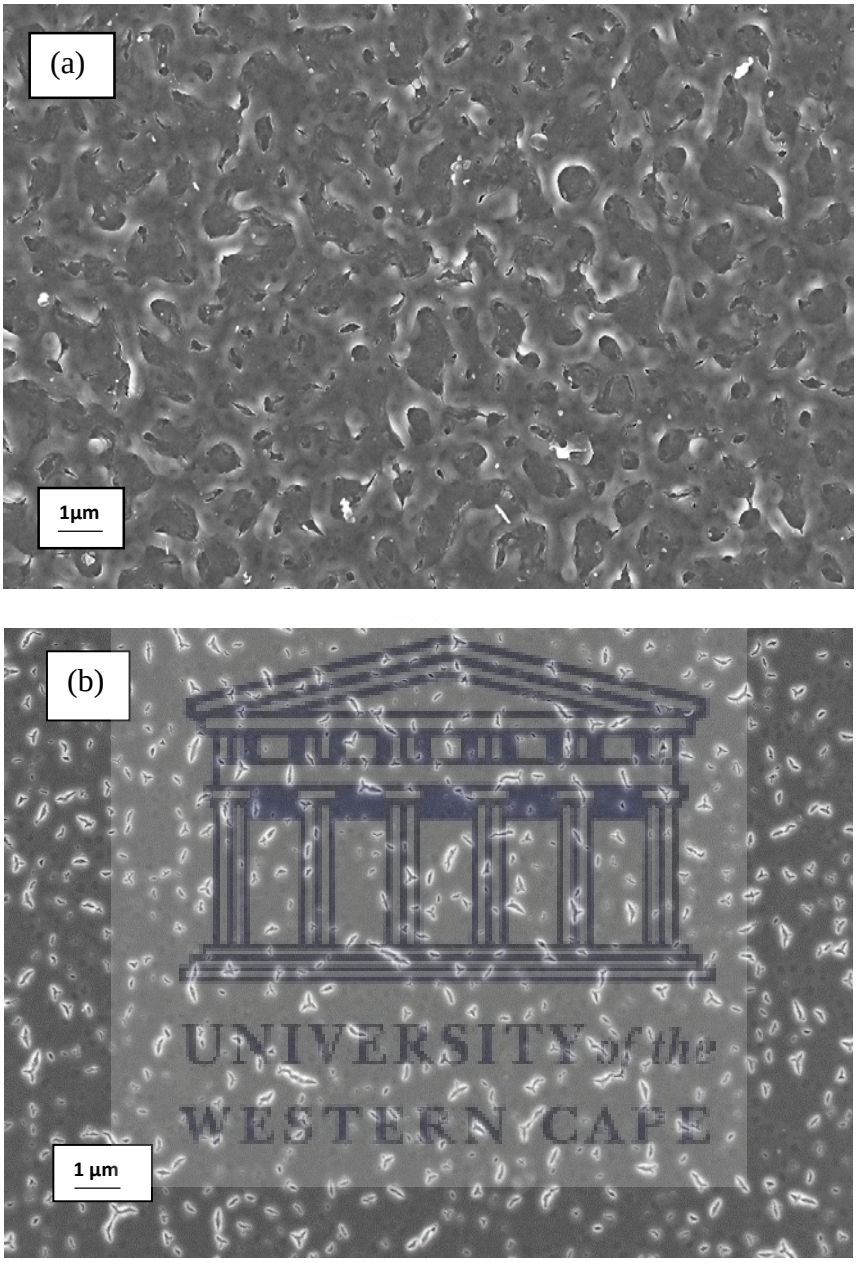

Figure 4. 2: SEM images of TiO_2 thin films ramp-annealed for different acidic acid concentrations of (a) 0.1 ml and (b) 0.2 ml.

EDS was used to confirm the presence of TiO_2 and to confirm that there were no undesirable chemical residues in the sample. The EDS indeed confirmed the purity of TiO_2 represented by the presence of Ti and O elements. The presence of Sn, Ca, In and Si are from the substrate that was used. The detected carbon is from the carbon coating used during the preparation of the sample.

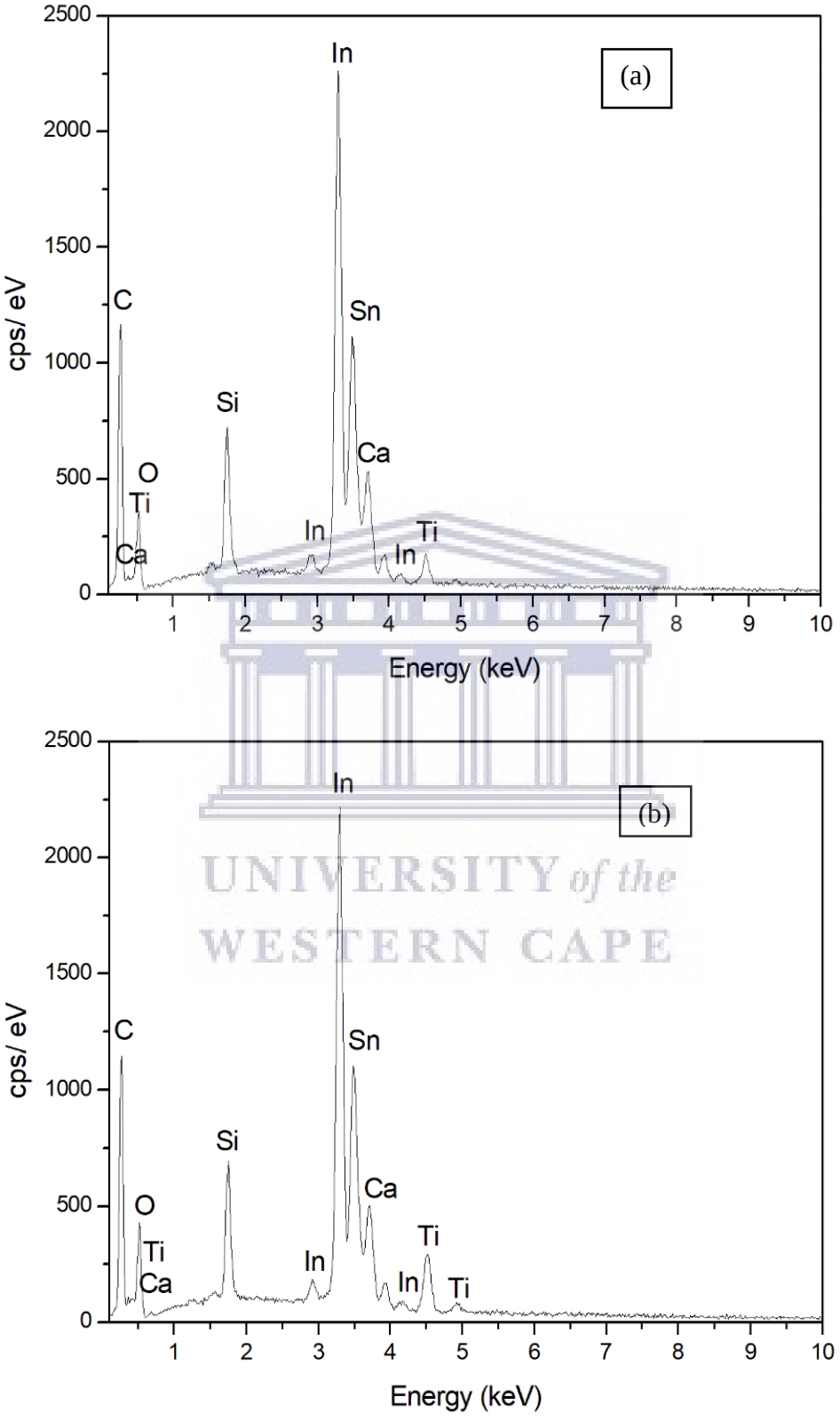

Figure 4. 3: EDS of (a) TiO_2 thin film conventionally annealed (b) TiO_2 thin film ramp-annealed on ITO substrate.

4.3.2 Structural analysis of the TiO_2 thin film layers.

X-ray diffraction (XRD) patterns of the samples were taken and analysed for phase and crystalline structure, using an Empyrean diffractometer with Cu Kα radiation (wavelength λ = 1.542Å). For the TiO_2 thin film annealed at 500 °C the x-ray diffraction pattern in Figure 4.4, exhibits diffraction peaks (101), (004), (211), (204) which compares well to the peaks of (JCPDS 21-1272) and (101), (111), (200) which compares well to the peaks of (JCPDS 21-1276). The prepared film shows a mix of rutile and anatase phases represented by r (JCPDS 21-1276) and a (JCPDS 21-1272), respectively. The presence of both anatase and rutile phases indicates high crystallinity and also exhibits improved photocatalytic performance that was investigated by Hurum et al. [4.20] to explain this enhancement. The peaks marked by a (*) are due to the presence of ITO from the substrate. In Figure 4.4(b) no crystalline peaks are observed for the TiO_2 material, only ITO peaks are visible, this may be due to the method of producing the thin film as well as the film being too thin to be detected. Another explanation might be that the ramp-annealed thin film is still in the amorphous state due to the low processing temperature.

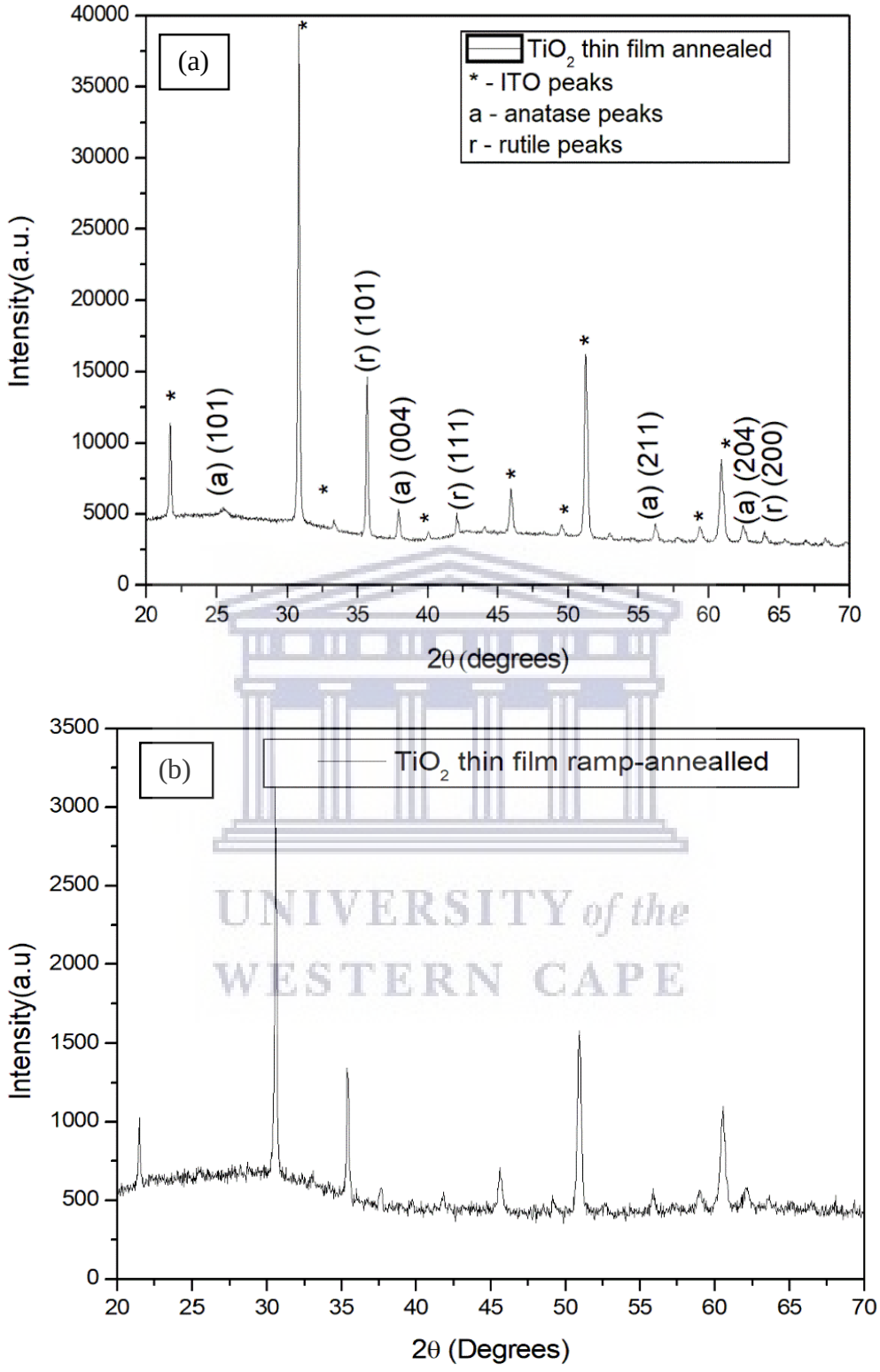

Figure 4. 4: XRD of TiO_2 thin film (a) conventionally annealed and (b) ramp-annealed.

The average crystallite sizes were calculated using Debye–Scherrer's formula:

$$D = \frac{K\lambda}{\beta_{hkl} Cos\theta}, \qquad (4.1)$$

where D = crystalline size, K = shape factor (0.9), and λ = 1.542Å and β_{hkl} = corrected broadening in radians. The average crystal size D calculated for each anatase and rutile phases are shown in Table 4.2.

Table 4. 2: Crystallite size, phase composition of the conventionally annealed sample.

	Calculated
TiO_2 thin film	**D (nm)**
Anatase	45.84
Rutile	56.80

From the interplanar spacing and the set of lattice parameters (hkl), the lattice constants for a tetragonal structure a and c was calculated from [4.11]:

$$\frac{1}{d^2} = \left(\frac{h^2 + k^2}{a^2}\right) + \frac{l^2}{c^2} \qquad (4.2)$$

The values of the experimental parameters are compared to the standard parameters in Table 4.3.

Table 4. 3: The values of the experimental parameters will be compared to the standard parameters.

	Calculated		Ref. code: 21-1272		Ref. code: 21-1276	
TiO_2 thin film	**a (Å)**	**c (Å)**	**a (Å)**	**c (Å)**	**a (Å)**	**c (Å)**
Conventionally annealed (anatase)	3.7583	9.4892	3.7852	9.5139	-	-
Conventionally annealed (rutile)	4.1159	3.1802	-	-	4.5933	2.9592

4.3.3 Chemical analysis of the TiO_2 thin film layers.

The chemical structure of the deposition of TiO_2 thin films were analysed using FTIR spectroscopy. Figure 4.5 shows the FTIR spectra of thin films spin coated on Si substrates after conventional and ramp-annealing.

As can be seen in Figure 4.5, the features in the band range 400-900 cm^{-1} is characteristic of TiO_2 [4.21]. It can also be observed that the 400-500 cm^{-1} peak becomes sharper due to the higher deposition temperature used for the conventionally annealed treatment.

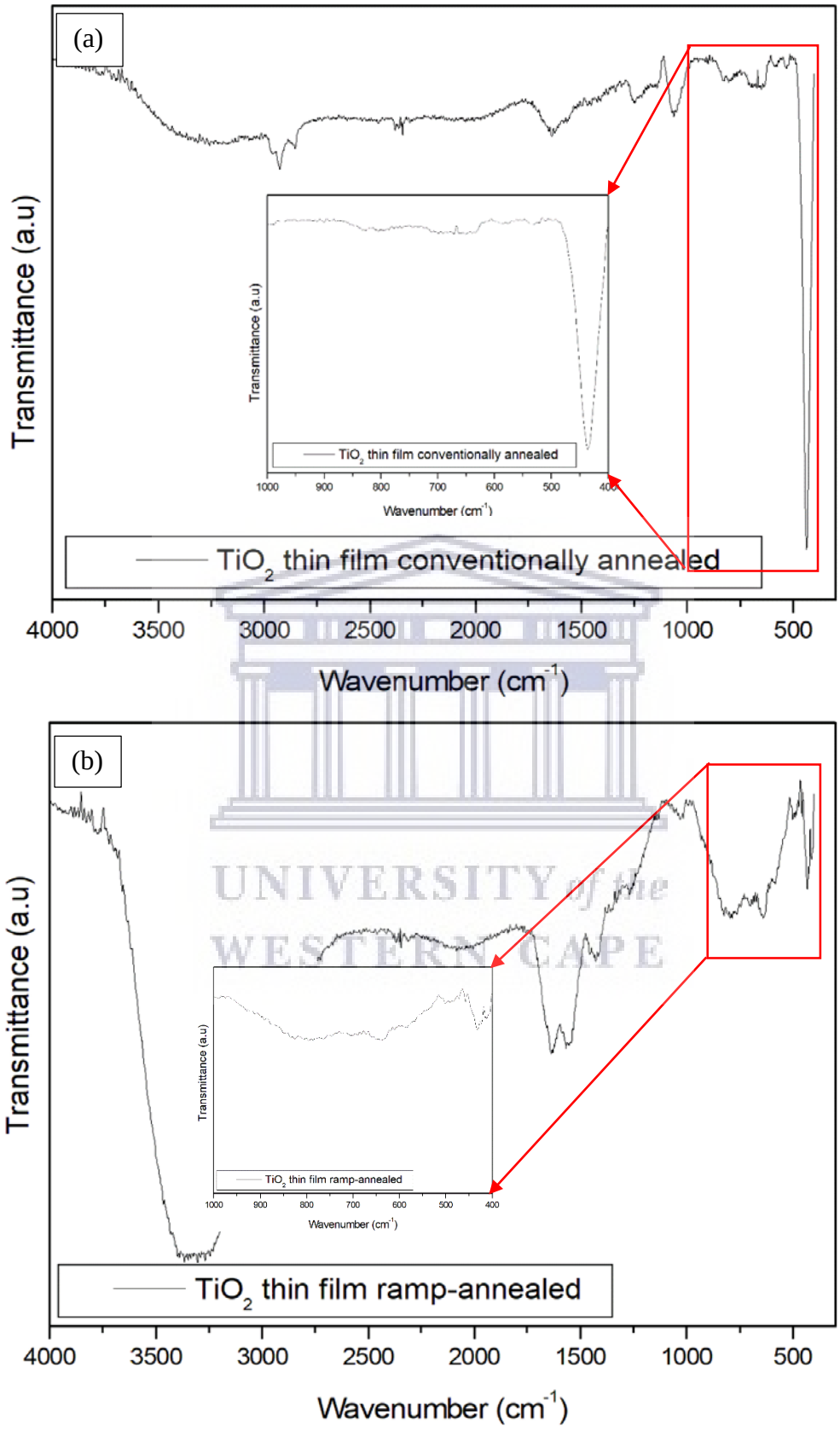

Figure 4. 5: FTIR spectra of TiO_2 solution spin-coated on Si-substrate (a) conventionally annealed and (b) ramp-annealed TiO_2 thin films.

From the inset of Figure 4.5 the weak bands around 431.45 cm^{-1} and 437.25 cm^{-1} may be assigned to the Ti-O-Ti stretching vibration [4.22]. The 796.04 cm^{-1} peak is related to the titanium isopropoxide which is ascribed to the Ti-O stretching mode [4.22]. The bands at 1053.14 cm^{-1} and 1561.55 cm^{-1} are due to the respective C-O and C-C stretching modes [4.23]. Weak bands in a region 2937.16 cm^{-1} can be assigned to the C-H stretching of hydrocarbon contamination at the TiO_2 surface, which could not be removed by the heat treatment at 500 °C in air [4.24]. The 1639.26 cm^{-1} band is assigned to the O-H stretching mode and finally the broad absorption band centred at 3319.90 cm^{-1} (also O-H stretching mode) is only observed in the ramp-annealed sample due to lower annealing temperature [4.25].

Table 4. 4: FTIR absorption bands and assignments of TiO_2.

Peak wavenumber (cm^{-1})	**Assignment**
431.45, 437.25	Ti-O-Ti stretching modes
796.04	Ti-O stretching modes
1053.14	C-O stretching mode
1561.55	C-C stretching mode
2937.16	C-H stretching mode
1639.26, 3319.9	O-H stretching mode

4.3.4 Optical properties of the TiO_2 thin film layers.

The TiO_2 ETL is crucial to ensure that incoming light crossing the ETL is absorbed in the photoactive layer. The transparency of the TiO_2 ETL layers on glass/ITO were thus probed by UV-vis spectroscopy. From the spectra, it was observed that the two metal oxide thin films acting as ETLs were transparent in the visible region and showed absorption in the UV region. The highest transmittance is for the TiO_2 thin film conventionally annealed. The TiO_2 ramp-annealed thin film is less transparent with respect to the conventional annealed thin film. The change in transmittance might be

attributed to differences in the surface microstructure. It is also consistent with the hazy appearance of the thin film which shows a light absorption and light scattering effect. The other change in the transmittance can also be due to the two contrasting annealing methods. The maximum transmittance for the two samples ranges between 75% to 85% in the visible range. As can be seen in Figure 4.6, an increase in annealing temperature improves the film's optical transmission. Ahmed et al. [4.26] showed that the ITO thin film exhibits enhanced crystallinity with increasing temperature. From this statement the optical transmittance increase can be correlated with improved crystallinity of both the ITO substrate and the TiO_2 thin film [4.27]. Moreover, the TiO_2 thin film indicates an improvement in the crystalline quality when conventionally annealed.

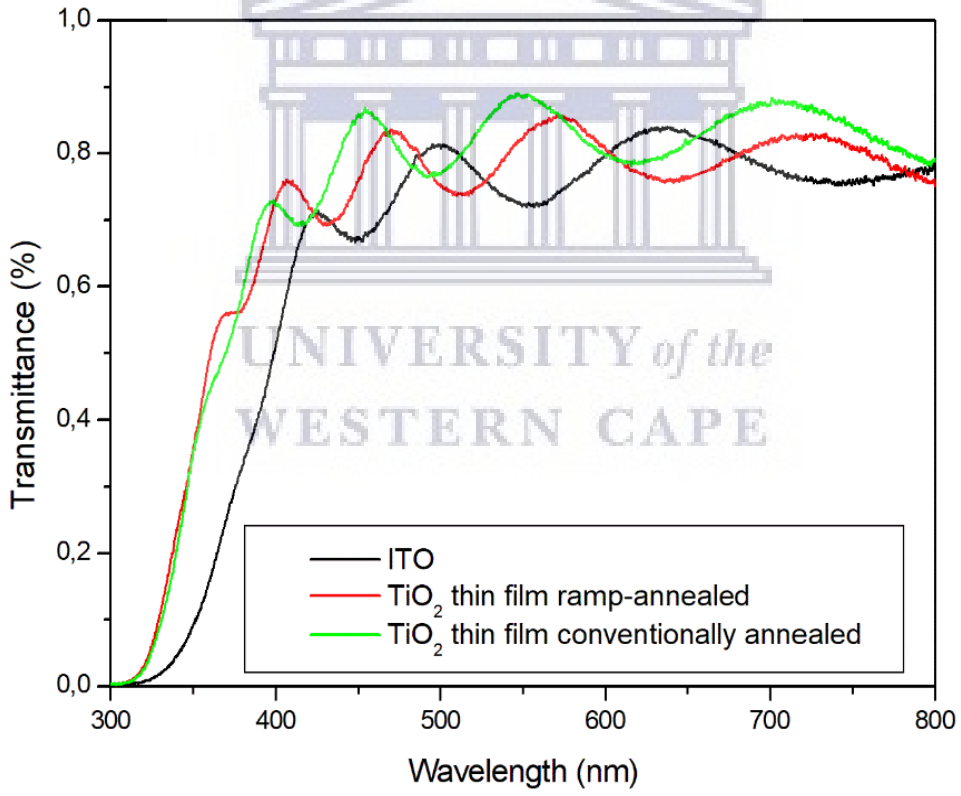

Figure 4. 6: Transmission spectra of TiO_2 thin film conventionally annealed and TiO_2 thin film ramp-annealed on ITO substrate and bare ITO on glass.

We used absorbance measured from the glass side of the sample with the active layer deposited on the ETLs that indicates that the polymer films with

the ramp annealed TiO_2 thin film showed increased absorption, which is indicated with the orange curve in Figure 4.7. This measurement was performed to probe whether the active layer behaves differently for the different ETLs when incident light crosses the ETL and is absorbed by the active layer.

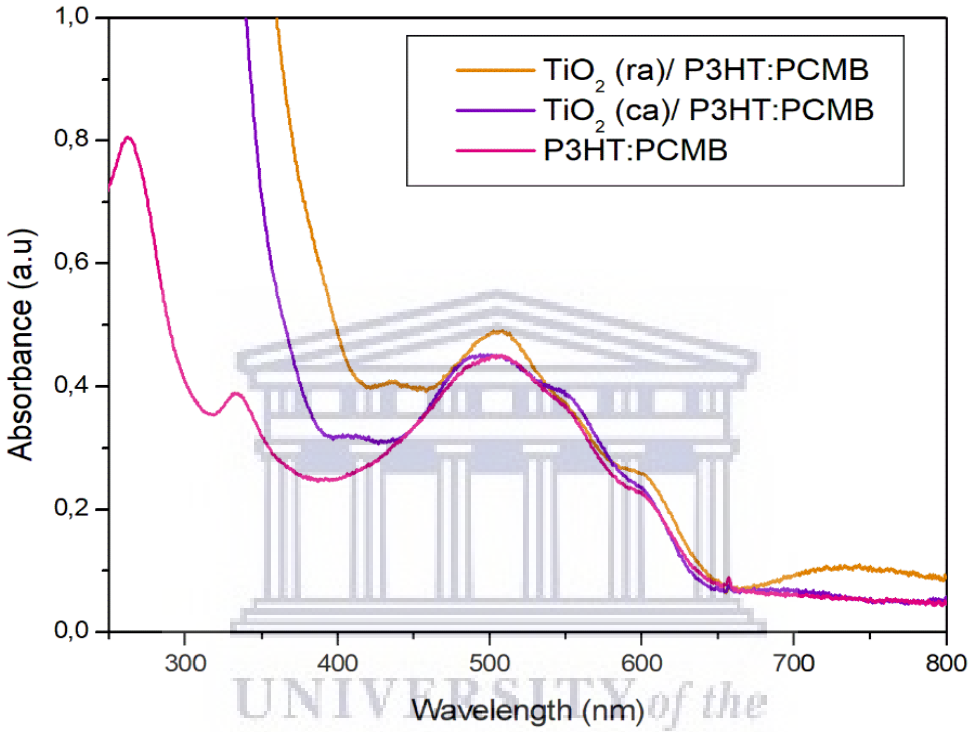

Figure 4. 7: Absorbance spectra of the active layer on TiO_2 layers (ca – conventionally annealed, ra – ramp-annealed) from glass side.

The optical band gap of the thin films was evaluated from the transmission spectra of the thin films coated on quartz glass substrates. The extrapolation of the optical band gap was performed using $(\alpha h\upsilon)^{1/n} = B(h\upsilon - E_g)$ (Tauc's model described in chapter 3.3.4).

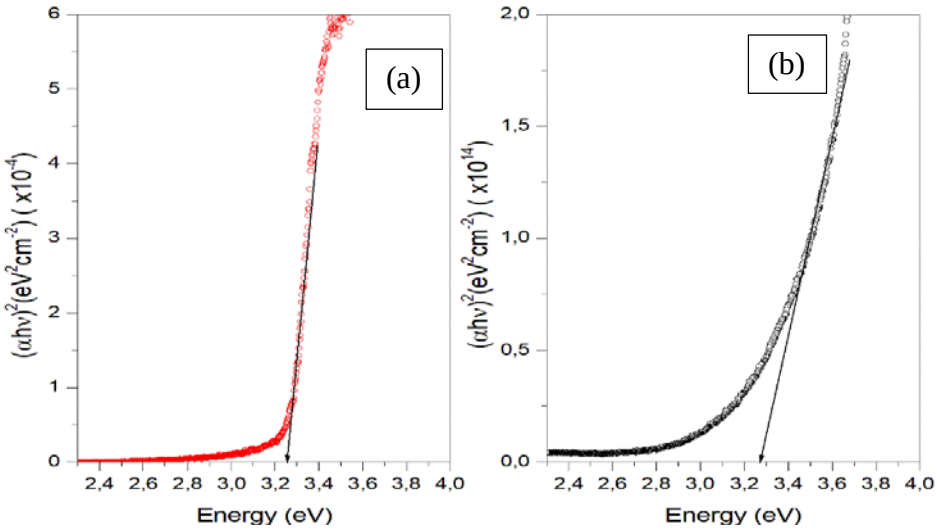

Figure 4. 8: $(\alpha h\upsilon)^2$ versus photon energy ($h\upsilon$) plot of (a) TiO_2 thin film ramp annealed and (b) TiO_2 thin film conventionally annealed.

A good linear relationship was obtained and fitted by means of equation (3.4); the results are shown in Figure 4.8. Indication of a direct band gap of 3.27 eV and 3.29 eV for TiO_2 is also in fair agreement with the literature value of 3.20 eV [4.2]. The optical band gap for both TiO_2 thin films blue-shifted from 3.20 eV to 3.27 eV and 3.29 eV, respectively [4.28]. Overall, the modification of the band gap can be attributed to improved crystallinity of the thin films [4.29].

In order to confirm the effect of different annealing methods diffuse reflectance spectroscopy (DRS) were carried out. Figure 4.9 shows plots of the diffuse reflectance (DR) spectroscopic investigations to give further insight into the scattering properties of the TiO_2 thin films. It was observed that compared to the conventionally annealed TiO_2 thin film, the DR was higher for the ramp-annealed TiO_2 thin film. The low reflectance as observed for the conventionally annealed thin film suggests most of the visible light is transmitted through the film, clearly shown in Figure 4.6. The ramp-annealed thin film exhibits nearly 20% improved DR compared to the conventionally annealed thin film due to a higher amount of light scattering; this can be ascribed to multiple-reflection by the mesoporous structure.

Consequently, optical pathways can be increased in the photo-cathode layer by the repeated reflection. Moreover, the probability of enhanced light-harvesting/ absorption can facilitate improved exciton generation. In turn the increase in photo-generated excitations could lead to improved short-circuit current [4.30].

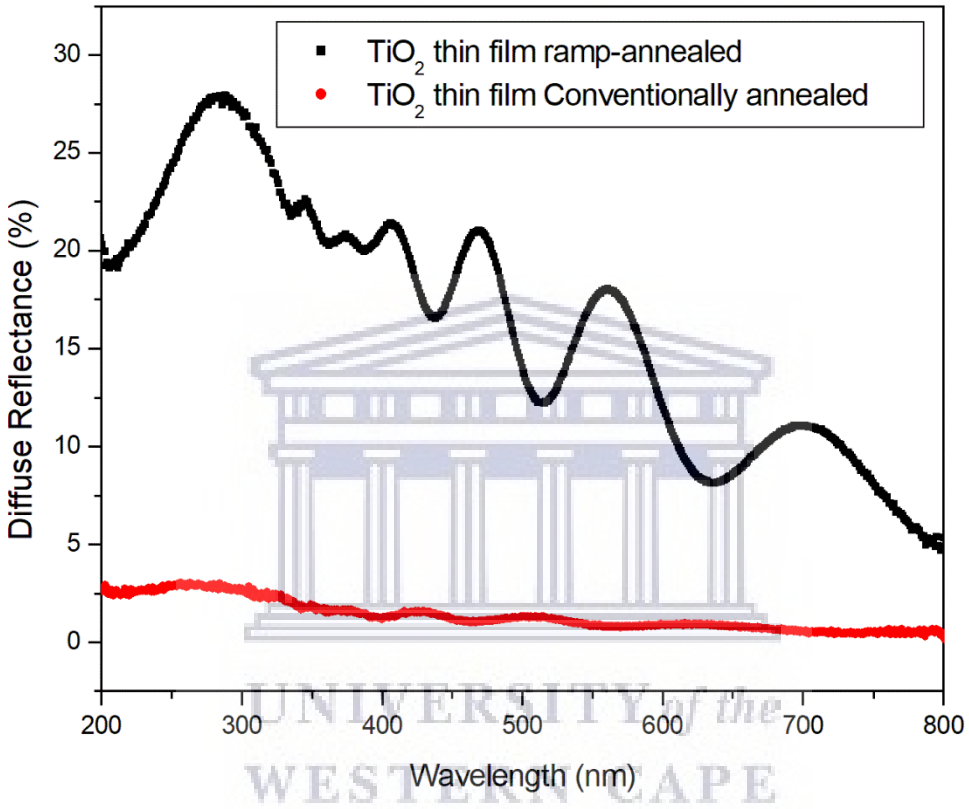

Figure 4. 9: Diffuse Reflectance Spectra of TiO_2 thin film.

4.4 Conclusion

The structural and optical properties of TiO_2 were investigated using ultraviolet-visible (UV-VIS) spectroscopy, high-resolution scanning electron microscopy (HR-SEM) and x-ray diffraction (XRD).

We have successfully fabricated the TiO_2 layer by spin coating the precursor onto the substrate, followed by annealing. The behaviour of the thin films is found to be dependent on the post deposition annealing. A

correlation between the morphology and the solution concentration was established. XRD results confirmed that the thin films are TiO_2 without any impurities and have both anatase and rutile phases; additional support to confirm this came from FTIR analysis. UV-vis transmission spectra showed an average of around 80% transmission that was observed for the TiO_2 thin films. The optical properties of TiO_2 thin films make it suitable to serve as an ETL in an inverted OSC device, which is explored in chapter 5.

References

[4.1] Reyes-Coronado, D., Rodríguez-Gattorno, G., Espinosa-Pesqueira, M.E., Cab, C., de Coss, R.D. and Oskam, G., 2008. Phase-pure TiO_2 nanoparticles: anatase, brookite and rutile. *Nanotechnology*, *19*(14), p.145605.

[4.2] Senthil, T.S., Thambidurai, M., Muthukumarasamy, N. and Balasundaraprabhu, R., 2010. Structural and optical investigations on nanocrystalline TiO_2 thin films prepared by sol-gel spin coating technique. *International Journal of Nanoscience*, *9*(04), pp.355-358.

[4.3] Vishwas, M., Sharma, S.K., Rao, K.N., Mohan, S., Gowda, K.A. and Chakradhar, R.P.S., 2010. Influence of surfactant and annealing temperature on optical properties of sol-gel derived nanocrystalline TiO_2 thin films. *Spectrochimica Acta Part A: Molecular and Biomolecular Spectroscopy*, *75*(3), pp.1073-1077.

[4.4] Wu, C.Y., Lee, Y.L., Lo, Y.S., Lin, C.J. and Wu, C.H., 2013. The thickness-dependent photocatalytic performance of nanocrystalline TiO_2 thin films prepared by sol-gel spin coating. *Applied Surface Science*, *280*, pp.737-744.

[4.5] Ranganayaki, T., Venkatachalam, M., Vasuki, T. and Shankar, S.L., 2014. Preparation and characterization of nanocrystalline TiO_2 thin films prepared by a sol-gel spin coating method. *J. Innovative Res. Sci*, *3*(10), p.16.

[4.6] Bakri, A.S., Sahdan, M.Z., Adriyanto, F., Raship, N.A., Said, N.D.M., Abdullah, S.A. and Rahim, M.S., 2017, January. Effect of annealing temperature of titanium dioxide thin films on structural

and electrical properties. In *AIP conference proceedings* (Vol. 1788, No. 1, p. 030030). AIP Publishing.

[4.7] Yoon, K.H., Noh, J.S., Kwon, C.H. and Muhammed, M., 2006. Photocatalytic behavior of TiO_2 thin films prepared by sol-gel process. *Materials Chemistry and Physics*, *95*(1), pp.79-83.

[4.8] Heo, C.H., Lee, S.B. and Boo, J.H., 2005. Deposition of TiO_2 thin films using the RF magnetron sputtering method and study of their surface characteristics. Thin Solid Films, 475(1-2), pp.183-188.

[4.9] Wu, J.J. and Yu, C.C., 2004. Aligned TiO_2 nanorods and nanowalls. *The Journal of Physical Chemistry B*, *108*(11), pp.3377-3379.

[4.10] Janisch, R., Gopal, P. and Spaldin, N.A., 2005. Transition metal-doped TiO_2 and ZnO—present status of the field. *Journal of Physics: Condensed Matter*, *17*(27), p. R657.

[4.11] Dongale, T.D., Shinde, S.S., Kamat, R.K. and Rajpure, K.Y., 2014. Nanostructured TiO_2 thin film memristor using hydrothermal process. Journal of Alloys and Compounds, 593, pp.267-270.

[4.12] Hanini, F., Bouabellou, A., Bouachiba, Y., Kermiche, F., Taabouche, A., Hemissi, M. and Lakhdari, D., 2013. Structural, optical and electrical properties of TiO_2 thin films synthesized by sol-gel technique. *IOSR Journal of Engineering (IOSRJEN)*, *3*(11), pp.21-28.

[4.13] Senthil, T.S., Muthukumarasamy, N., Agilan, S., Thambidurai, M. and Balasundaraprabhu, R., 2010. Preparation and characterization of nanocrystalline TiO_2 thin films. *Materials Science and Engineering: B*, *174*(1-3), pp.102-104.

[4.14] Ahmad, M.K., Halid, M.L.M., Rasheid, N.A., Ahmed, A.Z., Abdullah, S. and Rusop, M., 2010. Effect of annealing temperatures on surface morphology and electrical properties of titanium dioxide thin films prepared by sol-gel method. *Journal of Sustainable Energy & Environment*, *1*, pp.17-20.

[4.15] Noh, H., Oh, S.G. and Im, S.S., 2015. Preparation of anatase TiO_2 thin film by low-temperature annealing as an electron transport layer in inverted polymer solar cells. *Applied Surface Science*, *333*, pp.157-162.

[4.16] Ranganayaki, T., Venkatachalam, M., Vasuki, T. and Shankar, S.L., 2014. Preparation and characterization of nanocrystalline TiO_2 thin films prepared by sol-gel spin-coating method. *J. Innovative Res. Sci*, *3*(10), p.16.

[4.17] Huang, J.H., Wei, H.Y., Huang, K.C., Chen, C.L., Wang, R.R., Chen, F.C., Ho, K.C. and Chu, C.W., 2010. Using a low-temperature crystallization process to prepare anatase TiO_2 buffer layers for air-stable inverted polymer solar cells. *Energy & Environmental Science*, *3*(5), pp.654-658.

[4.18] Kaune, G., Memesa, M., Meier, R., Ruderer, M.A., Diethert, A., Roth, S.V., D'Acunzi, M., Gutmann, J.S. and Muller-Buschbaum, P., 2009. Hierarchically structured titania films prepared by polymer/colloidal templating. *ACS applied materials & interfaces*, *1*(12), pp.2862-2869.

[4.19] Zhang, J., Pazoki, M., Simiyu, J., Johansson, M.B., Cheung, O., Häggman, L., Johansson, E.M., Vlachopoulos, N., Hagfeldt, A. and Boschloo, G., 2016. The effect of mesoporous TiO_2 pore size on the

performance of solid-state dye-sensitized solar cells based on photoelectrochemically polymerized Poly (3, 4-ethylenedioxythiophene) hole conductor. *Electrochimica Acta*, *210*, pp.23-31.

[4.20] Hurum, D.C., Agrios, A.G., Gray, K.A., Rajh, T. and Thurnauer, M.C., 2003. Explaining the enhanced photocatalytic activity of Degussa P25 mixed-phase TiO_2 using EPR. *The Journal of Physical Chemistry B*, *107*(19), pp.4545-4549.

[4.21] Kumar, P.M., Badrinarayanan, S. and Sastry, M., 2000. Nanocrystalline TiO_2 studied by optical, FTIR and X-ray photoelectron spectroscopy: correlation to presence of surface states. Thin solid films, 358(1-2), pp.122-130.

[4.22] Vasconcelos, D.C.L., Costa, V.C., Nunes, E.H.M., Sabioni, A.C.S., Gasparon, M. and Vasconcelos, W.L., 2011. Infrared spectroscopy of titania sol-gel coatings on 316L stainless steel.

[4.23] Khan, M., Naqvi, A.H. and Ahmad, M., 2015. Comparative study of the cytotoxic and genotoxic potentials of zinc oxide and titanium dioxide nanoparticles. Toxicology reports, 2, pp.765-774.

[4.24] Nakamura, R., Imanishi, A., Murakoshi, K. and Nakato, Y., 2003. In situ FTIR studies of primary intermediates of photocatalytic reactions on nanocrystalline TiO_2 films in contact with aqueous solutions. Journal of the American Chemical Society, 125(24), pp.7443-7450.

[4.25] Sher Shah, M.S.A., Park, A.R., Zhang, K., Park, J.H. and Yoo, P.J., 2012. Green synthesis of biphasic TiO_2–reduced graphene oxide

nanocomposites with highly enhanced photocatalytic activity. ACS applied materials & interfaces, 4(8), pp.3893-3901.

[4.26] Ahmed, N.M., Sabah, F.A., Abdulgafour, H.I., Alsadig, A., Sulieman, A. and Alkhoaryef, M., 2019. The effect of post annealing temperature on grain size of indium-tin-oxide for optical and electrical properties improvement. *Results in Physics*, *13*, p.102159.

[4.27] Kars, I., Çetin, S.Ş., Kınacı, B., Sarıkavak, B., Bengi, A., Altuntaş, H., Öztürk, M.K. and Özçelik, S., 2010. Influence of thermal annealing on the structure and optical properties of dc magnetron sputtered titanium dioxide thin films. *Surface and Interface Analysis*, *42*(6-7), pp.1247-1251.

[4.28] Reddy, K.M., Manorama, S.V. and Reddy, A.R., 2003. Bandgap studies on anatase titanium dioxide nanoparticles. *Materials Chemistry and Physics*, *78*(1), pp.239-245.

[4.29] Soleimanian, V. and Aghdaee, S.R., 2011. The influence of annealing temperature on the slip plane activity and optical properties of nanostructured ZnO films. *Applied Surface Science*, *258*(4), pp.1495-1504.

[4.30] Wan, J., Tao, L., Wang, B., Zhang, J., Wang, H. and Lund, P.D., 2019. A facile method to produce TiO_2 nanorods for high-efficiency dye solar cells. *Journal of Power Sources*, *438*, p.227012.

CHAPTER FIVE

5 Performances of the inverted solar cells based on TiO_2 and ZnO blocking layers

5.1 Introduction

In this chapter the device preparation for metal oxides in organic/ hybrid solar cell is described. The impact of the spin coated and thermally evaporated MoO_x thin films on the device performance is investigated and described. It has been found that the efficiency of the device is critically affected by the MoO_x hole transport layer. The ZnO and TiO_2 electron transport layers are utilized in an inverted geometry and a comparative study is discussed. Finally, a Ag contact has been deposited. Knowing that surface texturing leads to enhanced optical path lengths the modified ETLs combined with the inverted OSCs can significantly influence the device performance, thus I-V characteristics of the various OSCs are discussed.

OSCs have been attracting much attention over the past decade and are nowadays considered a promising PV technology for solar energy harvesting. This is mainly due to the possibility of low-cost solution process capability and compatibility with flexible substrates [5.1, 5.2]. Due to its known functionality and processability over the years, attention was focused on conventional devices made of an active layer sandwiched between ITO/PEDOT: PSS and a low work function metal, typically aluminium. However, the acidic nature of PEDOT:PSS causes erosion of the ITO substrate and degrades the solar cell due to In diffusion into the active layer [5.3]. In addition, the diffusion of oxygen and moisture through the pinholes and grain boundaries of the Al electrode into the active layer was also found to degrade the device performance and reduce its lifetime [5.3]. This led to the implementation of alternative architecture, the so-called an inverted

design. As schematically shown in Figure 5.1, this architecture can be employed to improve the lifetime and stability of such devices by replacing the low work function metal Al with a high work function metal, which is less air-sensitive. The inverted configuration of OSCs also avoids the need for PEDOT:PSS at the ITO interface. Nowadays, this polymer is replaced with transition metal oxides such as ZnO or TiO_2 to form ETLs due to their superior atmospheric stability [5.5]. The purpose of these ETLs in an inverted OSC is to exploit their hole-blocking capabilities and to provide a low resistive path for efficient electron collection [5.6]. The HTLs are usually metal oxides such as MoO_3, V_2O_5, NiO and WO [5.4]. High work function metals such as Ag or Au were used as the electrode [5.6].

The sol-gel method for deposition of metal oxide thin films is used widely due to its simplicity and the ability to optimize the morphology of the film, which depends amongst others on the annealing temperature. This process offers customizable microstructure, excellent stoichiometry control of precursor solution and possible coating over large areas [5.7]. In this work, our study aims to optimize the solution processing of metal oxide thin films for use as ETL (ZnO & TiO_2) and HTL (MoO_x) in OSCs. The performance of devices constructed from a solution-processed MoO_x HTL is compared with those deposited via a more conventional method, namely thermal evaporation of MoO_x. For ETLs, we have prepared ZnO and TiO_2 by solution processing, and post-deposition treatment included a significant reduction in conventional high annealing temperature treatment. The influence of this approach on the morphology of the ETLs is investigated. The electrical characteristics of solar cell devices (glass/ ITO/ ETL/ P3HT: PCBM/ MoO_x/ Ag) were measured and compared.

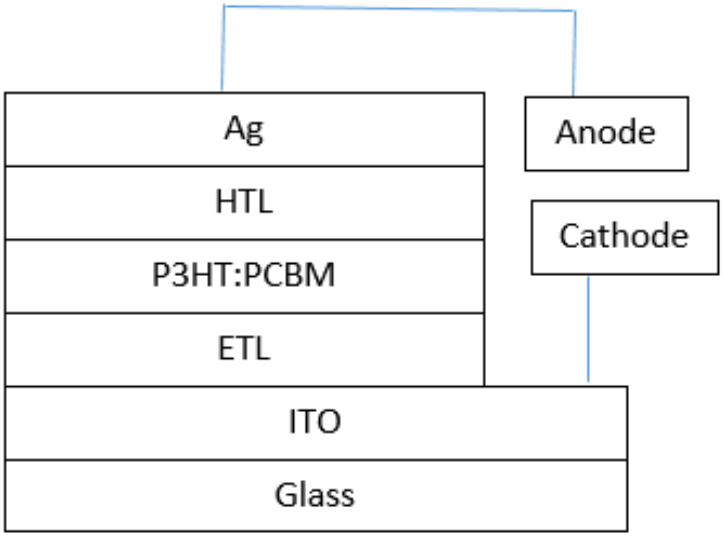

Figure 5. 1: Schematic of an inverted device structure.

5.2 Experimental details

5.2.1 Fabrication of the hole transport layer (HTL)

The Molybdenum (IV) oxide and Ammonium hydroxide (28 -30%) were all purchased from Sigma Aldrich and used as the starting material for the MoO_x HTL.

The MoO_x thin film was deposited by thermally evaporating the MoO_3 powder. The powder was placed in a molybdenum boat and loaded into the Vacutec vacuum chamber. The chamber was pumped down to a base pressure of 6.5×10^{-5} mbar before the evaporation started and the working pressure was maintained at 1×10^{-5} mbar throughout the process. The evaporated MoO_x thin film was deposited at an evaporation rate of 0.5 Å /s. The nominal thickness of the deposited film was measured to be 10 nm, using the Veeco Dektak profilometer. This was in close agreement with the quartz-crystal monitor that is part of the Vacutec vacuum system. The distance between the substrate and the source was approximately 12 cm in order to obtain a homogeneous thin film.

For the spin coated MoO_x thin film preparation, 50 mg of Molybdenum (iv) oxide was dissolved in 1 ml of Ammonium hydroxide (28-30%) in preparation of the precursor solution. The solution was magnetically stirred at 50 °C for 1 hour until the solution turned clear. Thereafter, the solution was cooled down to room temperature. The solution-processed MoO_x thin film was deposited by drop casting 200 µl of solution onto the surface of the prepared structure of glass/ITO/ETL/P3HT:PCBM. This was deposited at a spinning rate of 3000 rpm for 60 seconds, yielding a nominal thickness of 10 nm, as measured by the Veeco Dektak profilometer. The sample was then placed on the pre-heated Chemat hot plate for curing at 150°C for 10 minutes.

5.2.2 Device structures and device fabrication.

Pre-pattered ITO glass substrates (8-pixel) from Osilla were used for the OSC fabrication and testing. The ITO patterned substrates were placed in a rack to start the cleaning process. A small amount of Hellmanex (1 ml) were mixed in boiling DI-water (50 ml). The rack containing the ITO-substrates was placed in the Hellmanex solution and sonicated for 10 min. The ITO-substrates were then thoroughly rinsed consecutively in boiling DI-water, twice. Thereafter the ITO-substrates were sonicated in IPA for 10 minutes. This was followed by a second rinsing in boiling DI-water. When the cleaning was finished the ITO substrates were dried with compressed air/ nitrogen gun.

To fabricate the OSC devices as described in Table 5.1, after cleaning the substrates, the conventionally annealed ZnO and the ramp-annealed ZnO ETLs (refer to chapter 3) and the conventionally annealed TiO_2 and ramp-annealed TiO_2 ETLs (refer to chapter 4) were spin-coated on the patterned ITO using the Ossila spin coater. Subsequently, an optimal weight ratio of P3HT: PCBM of 1:1 and optimum annealing temperature of 150 °C was used as reported by Chirvase et al. [5.8] and Reyes-Reyes et al. [5.9],

respectively. The precursor material was prepared by stirring P3HT (15 mg/ ml) and PCBM (15 mg/ ml) which was dissolved in a solvent of 1, 2 dichlorobenzene at 60°C overnight using a Lasec digital hot plate stirrer at a rotational speed of 400 rpm. The as-prepared P3HT/ PCBM blend solution was deposited on top of the ITO/ ETL structure at 900 rpm for 100 seconds and then dried at 150 °C on a Chemat hot plate for 30 minutes. The resulting blended film was ∼100 nm thick as determined by profilometry. This was followed by the deposition of a Molybdenum (IV) oxide precursor both by thermal evaporation and spin coating methods. Finally, a 100 nm Ag layer was sequentially thermally evaporated at a deposition rate of 0.5 Å /s and base pressure of 6.5×10^{-5} mbar. The thermal evaporation of MoO_x and Ag were obtained using the Vacutec vacuum system in the CADAR (Cluster Apparatus for Device Application Research) situated in the Department of Physics and Astronomy at the University of the Western Cape (UWC). The device configurations are given in Table 5.1.

Table 5. 1: Device configurations based on the preparation method of the ETL and HTL.

	ETL conventionally-annealed	**ETL ramp-annealed**
MoO_x solution-processed	glass/ ITO/ ZnO/active layer/ MoO_x/ Ag.	glass/ ITO/ ZnO/active layer/ MoO_x/ Ag.
	glass/ ITO/ TiO_2/active layer/ MoO_x/ Ag	glass/ ITO/ TiO_2/active layer/ MoO_x/ Ag
MoO_x thermally evaporated	glass/ ITO/ ZnO/active layer/ MoO_x/ Ag.	glass/ ITO/ ZnO/active layer/ MoO_x/ Ag.
	glass/ ITO/ TiO_2/active layer/ MoO_x/ Ag	glass/ ITO/ TiO_2/active layer/ MoO_x/ Ag

5.2.3 Stages of lamella preparation by FIB-SEM.

In this section the different stages of TEM lamella preparation are explained, as depicted in Figure 5.2 below. Figure 5.2(a) illustrates the deposition of carbon either by Ga^+ ions or by electrons. This process is done to protect and stabilize the lamella sample and prevent it from breaking in the following stages. The next step is trench milling to remove the material at a desired location, shown in Figure 5.2(b). This is followed by the

separation of the lamella from the bulk of the material. Here the sample must be tilted as in Figure 5.2(c), such that the sides and the bottom can be cut by ion beam. Just before the lamella is cut free, a micromanipulator is fixed and welded to it for easy removal and transfer of the lamella from the sample to the TEM lift-out grid, Figure 5.2(d) and (e), respectively. Now the lamella is welded on the TEM transfer grid and separated from the micromanipulator. The last step, in Figure 5.2(f), is the cleaning process which is used to flatten or thin the lamella with an accelerating voltage of 5 kV and then post treat it with Ar^+ ions of low energy of 900 eV to reduce artifacts; thus enhancing the quality of the sample for high-resolution imaging.

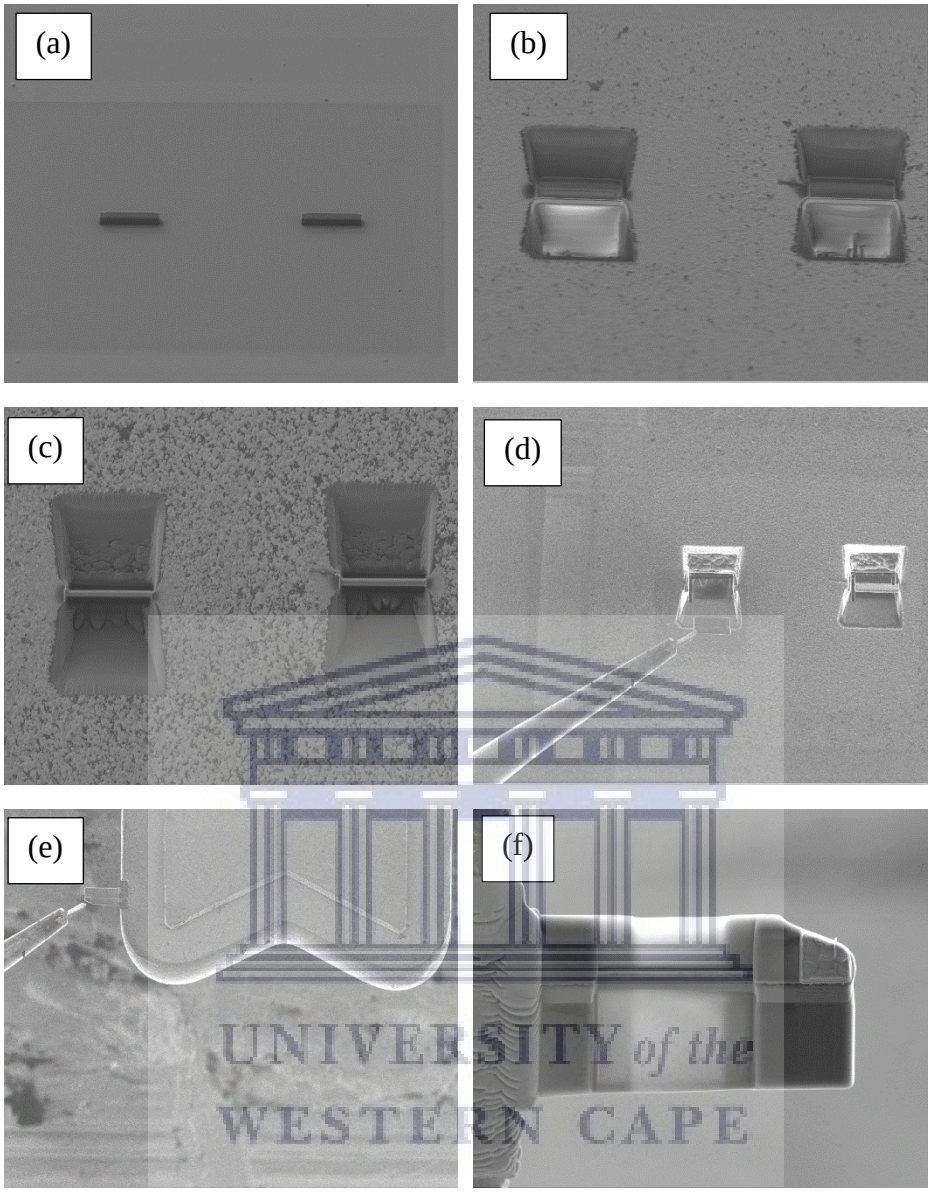

Figure 5. 2: Preparation of HR-TEM lamella by FIB milling (a) Carbon protection layer, (b) trench milling, (c) separation of lamella from bulk material, (d) removal of lamella, (e) welding on TEM transfer grid, (f) cleaning/ thinning process.

5.3 Results and discussion

5.3.1 High Resolution TEM analysis of the device.

In order to investigate more closely the individual layers within the inverted OSC device, we used FIB-SEM to slice the device and characterize it by

using HR-TEM. We investigated the cross-section of two inverted OSC devices with both ZnO ramp annealed ETL and with a thermally evaporated MoO_x HTL and solution-processed MoO_x HTL, respectively. Figure 5.3 below shows the HR-TEM image of the prepared cross-section where the individual layers of a complete device can be clearly identified. A thin layer of carbon was deposited on top of the device to protect it from damage by the FIB ion beam and this can clearly be identified by the dark grey contrast on the top. The cross-section also shows a dark contrast for the ITO, a slightly darker contrast for the Ag, a grey contrast for the organic material and a bright contrast for the ZnO and MoO_x. Figure 5.3(a) reveals that the thermally evaporated MoO_x acts as a separation layer between the P3HT:PCBM active layer and Ag electrode keeping them from diffusing into each other. It appears that there is an integration of the Ag and MoO_x layers at first; in fact, probing closer to the surface it becomes evident that there is an overlap of the Ag layer on the MoO_x layer, which may be caused by the milling process. The image also shows enhanced contact surface between the ZnO and ITO, which is essential to achieve high efficiency of extracting and transporting photogenerated electrons into the electrode and minimizing the charge recombination. Figure 5.3(b) presents the cross-section of the inverted OSC, similar to the cross-section in Figure 5.3(a). The bright contrast representing the MoO_x layer is absent here; hence we infer there is no buffer layer present. It is known that the MoO_x precursor solution has a hydrophobic nature [5.10], which can cause the diffusion of the silver into the P3HT:PCBM layer.

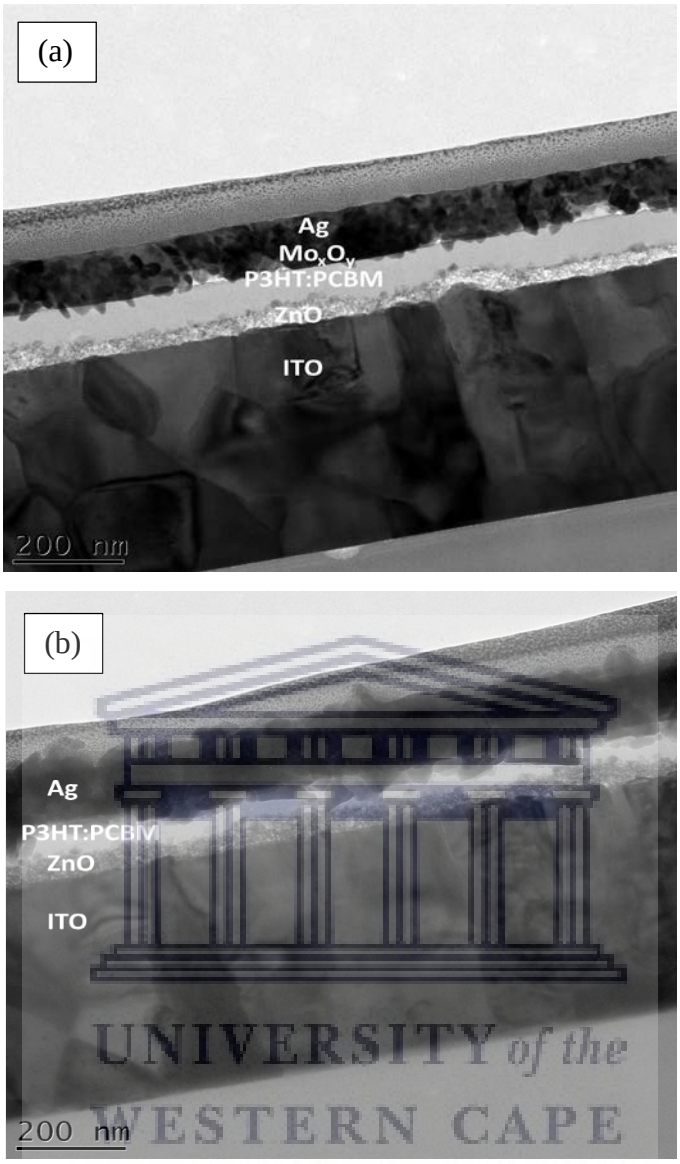

Figure 5. 3: HR-TEM cross-section view (a) representing an inverted device configuration with thermally evaporated MoO_x and (b) representing an inverted device configuration with solution-processed MoO_x.

5.3.2 High Resolution SEM analysis of the device.

Figure 5.4 illustrates the EDS line scan of the cross-section for the inverted OSC indicated by the yellow line. Five distinct zones can be observed, corresponding to the individual thin films that were successfully deposited. The EDS line scan verified the interpretation of various elemental compositions detected on the HR-TEM cross-section; confirming the

formation of layers composed of Zn, Ag, Sn, Mo and C. These elements are distributed uniformly across the whole device structure. However, a slight increase in the line scan reveals Sn signals from the ITO substrate, indicated by Layer 1. An increase in mainly Zn signals occurs as the scan reaches Layer 2, suggesting the layer is primarily ZnO. The content of carbon traces on Layer 1 may have been left behind by the Isopropanol solvent used in the cleaning procedure of the ITO substrate. The increase of the carbon signal at Layer 3 is a confirmation of the P3HT:PCBM photoactive layer; moreover the EDS line scan does not show any signal for possible sulphur detected from the P3HT. The further increase of carbon signal at the top of Layer 5 is from the carbon deposition which was formed to protect the device for the FIB milling process; no gallium was detected from this process. Layer 5 is the signal for the silver metal contact which is in good agreement with the experimental design. The EDS barely picks up the signal for Molybdenum as it may be approaching the EDS detection limit. The Zeiss EDS detector makes use of Berillium which produce a detection limit in the range of 1000-3000 parts per million (ppm). This is not useful for light element determination. Meanwhile the WDS has a detection range of 30-300 ppm; hence Molybdenum with an average of 1.5 ppm is difficult to detect efficiently.

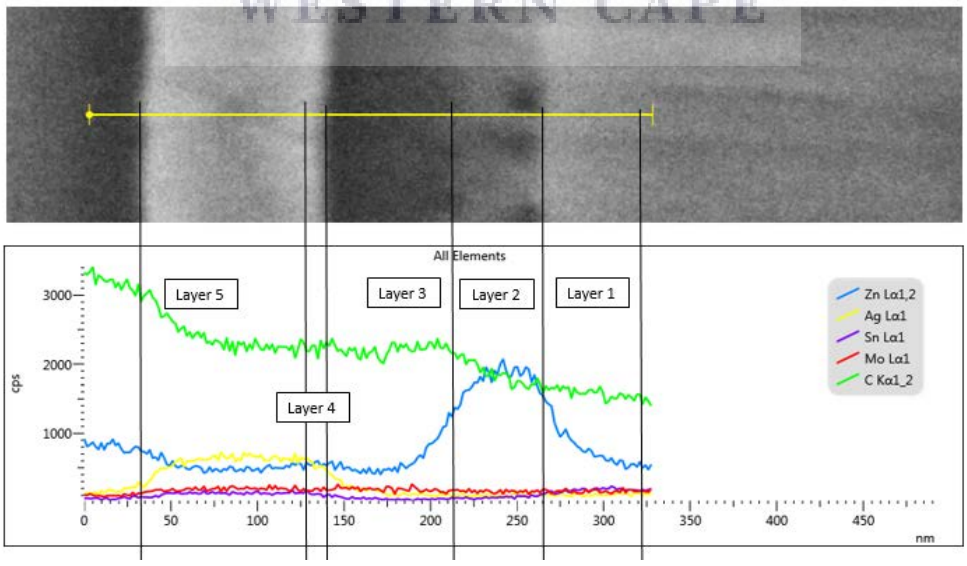

Figure 5. 4: EDS line scan analysis through a cross section of the inverted OSC with ZnO ETL showing the element distribution on every layer.

5.3.3 Current - voltage (I - V) characterization

The I-V characteristics of the solar cell devices with four different metal oxide ETLs are shown in Figure 5.5 and Figure 5.6. The un-encapsulated device of area 0.0256 cm^2 was characterized under simulated AM 1.5 illumination with an intensity of 100mW/cm^2. From Figure 5.5(a), the dark current plots for the inverted devices show diode behavior for all the devices. When the devices with solution-processed MoO_3 HTL, confirmed by comparing the JCPDS (05-0508) with the XRD measurements (see appendix A1), is under illumination it appears non-responsive; possibly due to HTL being a hydrophobic film which makes it difficult to form on top of the active layer of P3HT:PCBM. Hence this results in the possible diffusion of Ag ions and oxygen into the active layer, or unwanted electron extraction to the anode causing the device to short-circuit. However, when the HTL is replaced with the thermally evaporated MoO_x thin film a photoactive response is observed. The MoO_x thin film acts as a buffer layer to isolate the Ag anode from the P3HT:PCBM active layer, improving the quality of the interface and reducing recombination probabilities. Moreover, it facilitates hole transport to the Ag anode while providing blockage to the flow of electrons towards the anode. In addition, the buffer layer provides a barrier to effectively prevent diffusion of the Ag anode into the polymer active layer and protecting the active layer from being damaged during deposition of Ag [5.11, 5.12].

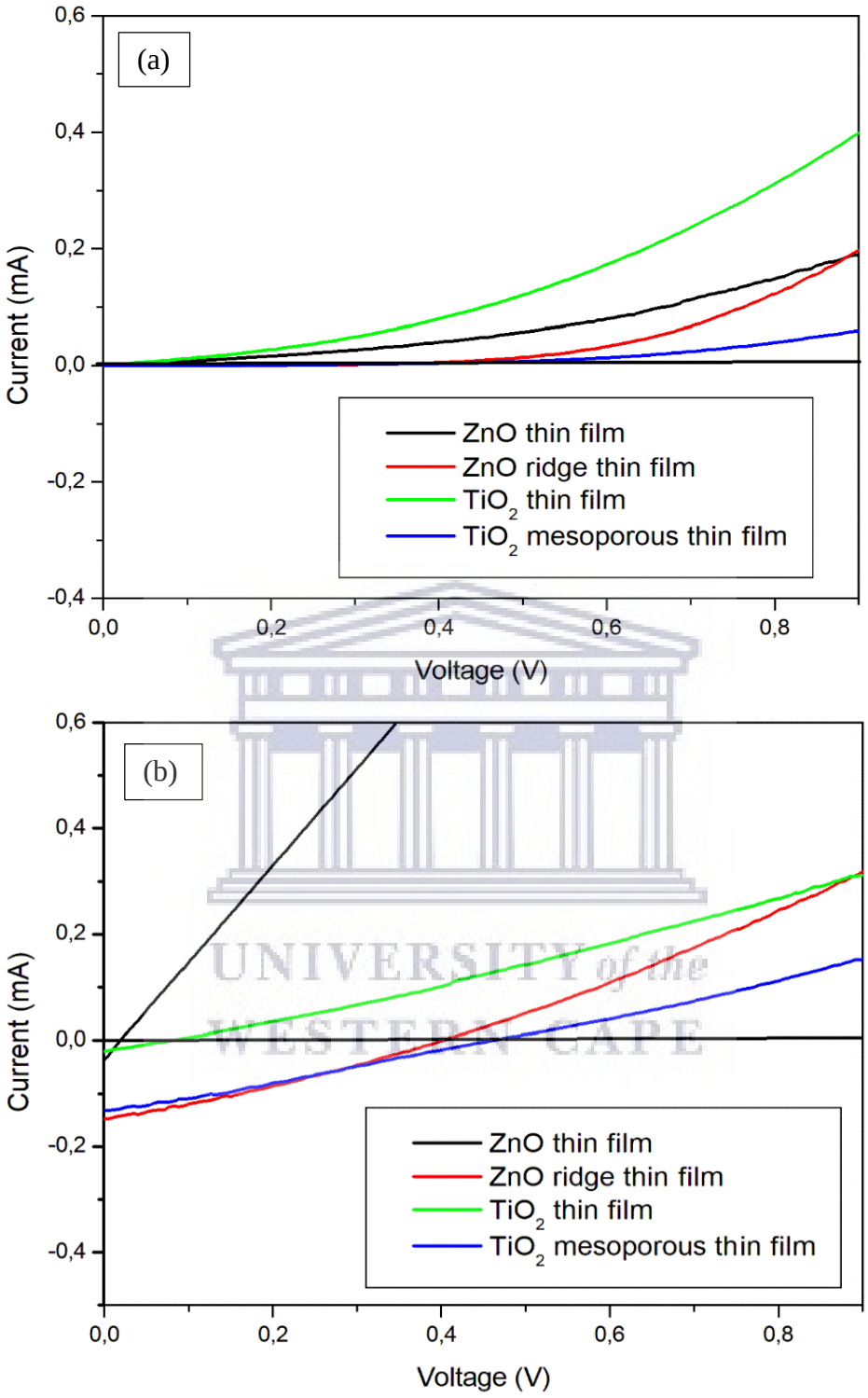

Figure 5. 5: Current-voltage curves of metal oxide ETLs and (a) solution-processed MoO_3 HTL in the dark, (b) solution-processed MoO_3 HTL under illumination.

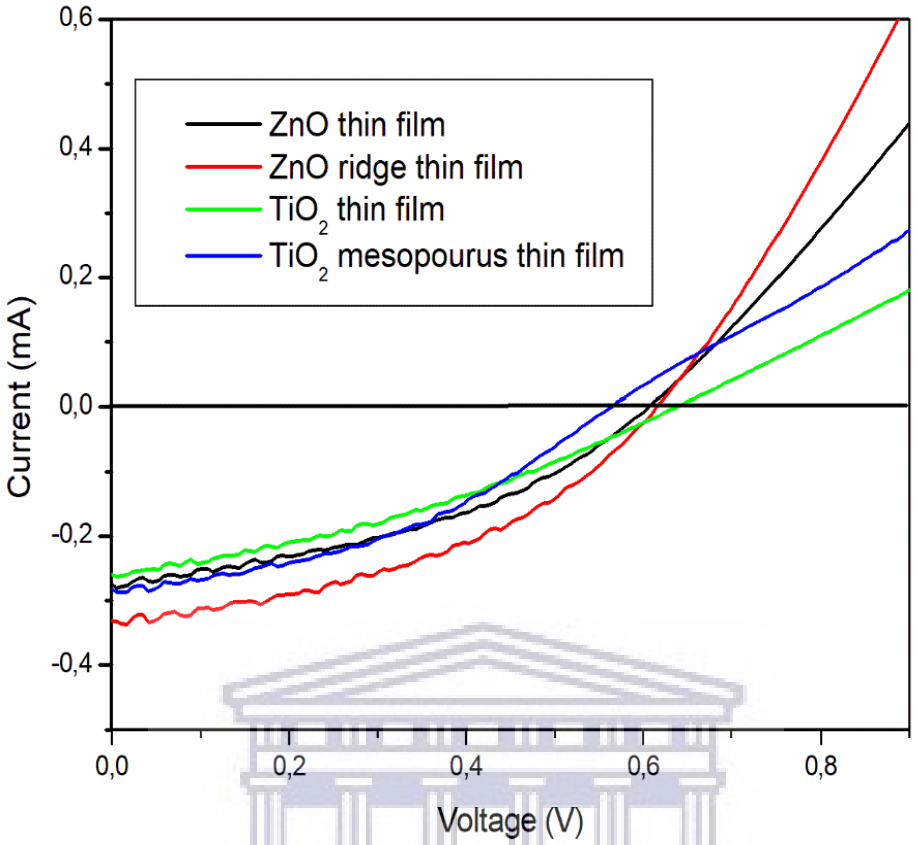

Figure 5. 6: Current-voltage curves of metal oxide ETL thermal evaporated MoO_x HTL under illumination.

The device performance is summarized in Table 5.2. Metal oxides, as interlayer material, plays an important role in the transportation of charge carriers. Furthermore, the metal oxide ETLs may enhance exciton dissociation at the polymer-blend ETL interface by increasing the number of excitons between acceptor and donor materials which leads to improved open-circuit voltage (V_{oc}). The PCE is governed by the number of charge carriers produced and those reaching the electrodes. When ZnO is ramp-annealed, the corresponding device showed remarkably improved performance over the device with ZnO which is conventionally annealed. For example, when the ZnO is ramp-annealed, the device has a PCE of 3.32% and when the device is conventionally annealed it has a PCE of only 2.57%. Yu et al. [5.13] also showed a PCE decrease from 2.88% to 2.08% for the ZnO thin film with decreased surface roughness. This is mainly caused by the decrease in the photocurrent from 0.33 mA to 0.27 mA and

the fill factor (FF). This change in current is due to the effect of the shunt resistance as the lower R_{sh} (135 $\Omega.cm^2$) gives rise to a reduced amount of current flow; meaning higher current leakage [5.14]. The same applies to the devices corresponding to the TiO_2 ETL. For device with TiO_2 ramp-annealed the PCE is 2.49% while the PCE is 2.19% for the device with TiO_2 conventionally annealed. The enhancement in performance of the device can be attributed to the lower leakage of current due to improvement in hole blocking and electron collecting capabilities of the ramp-annealed ETLs. The increased annealing temperatures in the conventional annealing approach may cause formation of electrically insulating oxide layers which creates a transport barrier and decreases performance [5.15], and decreases its efficiency to act as a buffer layer compared to the ramp-annealing approach. Since the conditions of the active layer, HTL and top electrode are kept the same throughout; the performance of the devices can be ascribed solely to the ETL. To clarify, the textured ETLs formed by ramp-annealing shows improved charge extraction and PCE which is correlated with the rougher ZnO surface and the mesoporous TiO_2. These textured ETLs provide an increased contact area with the photoactive layer, thereby reducing photo-carrier recombination during electron transport [5.16]. Excitons created in the photoactive layers during light absorption can more efficiently be separated by increasing the contact area between the ETLs and photoactive layer, with further increased light scattering provided by the ramp-annealed thin films. This makes enhanced photon absorption into the device possible. The overall photovoltaic performances of these devices are consequently improved, similar to previously reported experiments [5.17, 5.18].

Table 5. 2: Performance parameters of inverted OSCs based on thermal evaporated MoO_x.

DEVICE	V_{oc} (V)	I_{sc} (mA)	FF	Rsh ($\Omega.cm^2$)	Rs ($\Omega.cm^2$)	PCE (%)
ZnO thin film	0.61	0.27	0.40	135.38	12.59	2.57
ZnO ridge thin film	0.61	0.33	0.42	155.02	16.80	3.32
TiO_2 thin film	0.64	0.26	0.34	121.15	16.62	2.19
TiO_2 mesoporous thin film	0.57	0.28	0.40	145.29	19.76	2.49

Further investigation into the all solution-processed inverted solar cell yielded an electrical response. The application of a modified active layer - an increased concentration from 15 mg/ ml to 30 mg/ml and a spin deposition rate of 800 rpm for 80s, resulted in a thicker thin film of ~ 120 nm. Moreover, replacing the Ammonium hydroxide solvent of the MoO_3 solution with isopropanol lead to an increased adhesion between the MoO_x thin film and the P3HT:PCBM active layer, ensuring favorable HTL contact at the active layer/HTL/Ag interface. In addition to the change of solvent of the MoO_x solution, the volume used to spin-cast was increased to 400 µl. These changes were brought on by using the spin coating technique [5.19]. However, the solution still exhibits a discontinuous surface coverage. A moderate device response arose due to the aforementioned change for the devices with respective ETLs as depicted in Figure 5.7 below.

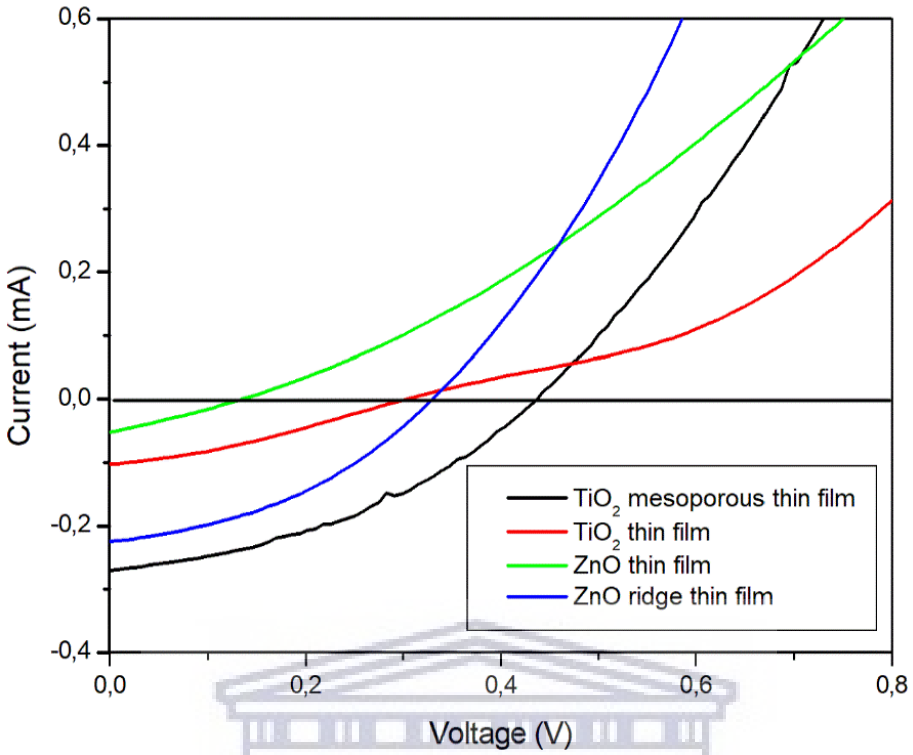

Figure 5. 7: Current-voltage curves of metal oxide ETL solution-processed MoO_x HTL under illumination.

The photovoltaic performance of the all solution processed devices are summarized in Table 5.3. The best performance is obtained from the device with the TiO_2 mesoporous thin film as the ETL. Making use of a solution processed MoO_x HTL resulted in a 72 % drop of the solar cell PCE with a considerably lower PCE of 1.8 % compared to the 2.49 % for the same inverted OSC with the thermally evaporated MoO_x HTL. The same effect applies for the OSC with the ZnO ridge thin film; although its PCE only decreased with 34 %, from an efficiency of 3.32 % to 1.14 %. This lower PCE is mainly due to a lower V_{oc}. This may be due to the difficulty of achieving a full coverage of the solution coated MoO_x HTL; thus creating a possibility for current leakage. The performance of the conventionally annealed ZnO and TiO_2 thin films exhibits an even further decrease in performance with an efficiency of around 0.1 % and 0.38 %, respectively. This behavior demonstrates that the method for producing the MoO_x HTL has a significant influence on the device performance.

Table 5. 3: Performance parameters of inverted OSCs based on solution-processed MoO_x.

DEVICE	V_{oc} (V)	I_{sc} (mA)	FF	Rsh ($\Omega.cm^2$)	Rs ($\Omega.cm^2$)	PCE (%)
ZnO thin film	0.14	0.05	0.27	69.70	18.30	0.08
ZnO ridge thin film	0.33	0.23	0.39	94.81	4.71	1.14
TiO_2 thin film	0.30	0.10	0.32	126.86	18.98	0.38
TiO_2 mesoporous thin film	0.43	0.27	0.39	115.52	6.07	1.80

It appears that increasing the thickness of the solution-processed MoO_x thin film is not necessarily an effective decision, due to the insulating nature of MoO_x thin films greater than 10 nm. This will reduce the short-circuit current even further, resulting in a decreased PCE [5.19]. However, in our experience we conclude that our devices are crucially reliant on the MoO_x layer.

It is thus feasible that an all solution-processed inverted OSC can be feasibly be constructed, depending on an optimized MoO_3 precursor solution.

5.4 Conclusion

At the conclusion of this series of studies, the OSC devices have been optimized in terms of annealing conditions and ETL/HTL materials. There is much potential in the field of organic photovoltaics. Different materials can be explored for the absorber layer as well as the HTL of the cell.

The solution processing technique was successfully employed to fabricate highly transparent ETLs with different annealing processes under ambient conditions. OSCs with solution-processed ETLs: ZnO and TiO_2 and thermal evaporated (MoO_x) HTL showed photoactive response. Taking into account the above results, it is strongly suggested that a thin metal oxide film as buffer layer between the anode and the photoactive layer blend of P3HT and PCBM polymer is necessary to form and complete the inverted OSC.

The importance of the surface morphology of the ETLs in determining the photovoltaic performance of the OSC was investigated. The results show that the OSCs with textured ETLs exhibit better photovoltaic performance in comparison with the OSCs with smooth ETLs. The increase in short-circuit current from 0.33 mA and 0.28 mA for ZnO and TiO_2, respectively, originated from the textured ETLs enhanced charge-carrier transport and enhanced light trapping capability. Furthermore, morphology differences created by ramp–annealing appear to have a more significant impact on the device performance compared to the conventional annealed approach. The best PCE is from the ZnO ridge thin film which shows superior charge transfer properties in inverted OSCs, with higher FF (0.42) leading to the PCE (3.32%). Consequently, by controlling the morphology by ramp-annealing one can significantly improve the performance of the inverted OSCs. From the evaluation of the electrical performance, the devices containing thermally evaporated MoO_x HTL shows superiority over the devices with solution-processed MoO_3 HTL. However, the effect of the viscosity of the MoO_3 solution to serve as an HTL is to be further studied due to the lack of charge transfer across the HTL and back contact in OSCs for solution-processed hole transport layers.

In summary, new materials, characterization techniques and deposition methods are likely to yield better performance for organic photovoltaics. Further study may be conducted to optimize the cell construction.

References

[5.1] Morvillo, P., Diana, R., Nenna, G., Bobeico, E., Ricciardi, R. and Minarini, C., 2016. High performance inverted polymer solar cells with solution processed metal oxides as electron transport layers: A comparative study. *Thin Solid Films*, *617*, pp.126-132.

[5.2] Zhang, F., Xu, X., Tang, W., Zhang, J., Zhuo, Z., Wang, J., Wang, J., Xu, Z. and Wang, Y., 2011. Recent development of the inverted configuration organic solar cells. Solar Energy Materials and Solar Cells, 95(7), pp.1785-1799.

[5.3] Peng, R., Yang, F., Ouyang, X., Liu, Y., Kim, Y.S. and Ge, Z., 2013. Enhanced photovoltaic performance of inverted polymer solar cells by tuning the structures of titanium dioxide. Thin Solid Films, 545, pp.424-428.

[5.4] Gupta, S.K., Sharma, A., Banerjee, S., Gahlot, R., Aggarwal, N. and Garg, A., 2013. Understanding the role of thickness and morphology of the constituent layers on the performance of inverted organic solar cells. Solar Energy Materials and Solar Cells, 116, pp.135-143.

[5.5] Chen, D., Zhang, C., Heng, T., Wei, W., Wang, Z., Han, G., Feng, Q., Hao, Y. and Zhang, J., 2015. Efficient inverted polymer solar cells using low-temperature zinc oxide interlayer processed from aqueous solution. Japanese Journal of Applied Physics, 54(4), pp.042301.

[5.6] Lattante, S., 2014. Electron and hole transport layers: their use in inverted bulk heterojunction polymer solar cells. Electronics, 3(1), pp.132-164.

[5.7] Singh, A., Kumar, A., Suri, N., Kumar, S., Kumar, M., Khanna, P.K. and Kumar, D., 2009. Structural and optical characterization of ZnO thin films deposited by sol-gel method. Journal of optoelectronics and advanced materials, 11(6), pp.790-793.

[5.8] Chirvase, D., Parisi, J., Hummelen, J.C. and Dyakonov, V., 2004. Influence of nanomorphology on the photovoltaic action of polymer–fullerene composites. Nanotechnology, 15(9), pp.1317.

[5.9] Reyes-Reyes, M., Kim, K. and Carroll, D.L., 2005. High-efficiency photovoltaic devices based on annealed poly (3-hexylthiophene) and 1-(3-methoxycarbonyl)-propyl-1-phenyl-(6, 6) C 61 blends. Applied Physics Letters, 87(8), pp.083506.

[5.10] Chambon, S., Derue, L., Lahaye, M., Pavageau, B., Hirsch, L. and Wantz, G., 2012. MoO3 thickness, thermal annealing and solvent annealing effects on inverted and direct polymer photovoltaic solar cells. Materials, 5(12), pp.2521-2536.

[5.11] Qi, B., Zhang, Z.G. and Wang, J., 2015. Uncovering the role of cathode buffer layer in organic solar cells. Scientific reports, 5, pp.7803.

[5.12] Elumalai, N.K., Saha, A., Vijila, C., Jose, R., Jie, Z. and Ramakrishna, S., 2013. Enhancing the stability of polymer solar cells by improving the conductivity of the nanostructured MoO_3 hole-transport layer. Physical Chemistry Chemical Physics, 15(18), pp.6831-6841.

[5.13] Yu, X.; Yu, X.; Hu, Z.; Zhang, J.; Zhao, G.; Zhao, Y. Effect of sol-gel derived ZnO annealing rate on light-trapping in inverted polymer solar cells. Mater. Lett. 2013, 108, 50–53.

[5.14] Liang, Z., Zhang, Q., Jiang, L. and Cao, G., 2015. ZnO cathode buffer layers for inverted polymer solar cells. Energy & Environmental Science, 8(12), pp.3442-3476.

[5.15] Ullah, I., Shah, S.K., Wali, S., Hayat, K., Khattak, S.A. and Khan, A., 2017. Enhanced efficiency of organic solar cells by using ZnO as an electron-transport layer. Materials Research Express, 4(12), pp.125505.

[5.16] Morvillo, P., Diana, R., Mucci, A., Bobeico, E., Ricciardi, R. and Minarini, C., 2015. Influence of annealing treatments on solution-processed ZnO film deposited on ITO substrate as electron transport layer for inverted polymer solar cells. Solar Energy Materials and Solar Cells, 141, pp.210-217.

[5.17] Sekine, N., Chou, C.H., Kwan, W.L. and Yang, Y., 2009. ZnO nano-ridge structure and its application in inverted polymer solar cell. Organic Electronics, 10(8), pp.1473-1477.

[5.18] Wiranwetchayan, O., Zhang, Q., Zhou, X., Liang, Z., Singjai, P. and Cao, G.Z., 2012. Impact of the morphology of TiO2 films as cathode buffer layer on the efficiency of inverted-structure polymer solar cells. Chalcogenide Lett, 9(4), pp.157-163.

[5.19] Spin coating: A guide to theory and techniques, Incomplete coating of substrate. [Online]. Available at: https://www.ossila.com/pages/spin-coating.

[5.20] Liu, J., Wu, X., Chen, S., Shi, X., Wang, J., Huang, S., Guo, X. and He, G., 2014. Low-temperature MoO_3 film from a facile synthetic route for an efficient anode interfacial layer in organic optoelectronic devices. *Journal of Materials Chemistry C*, *2*(1), pp.158-163.

CHAPTER SIX

6 Summary and future work

In the thesis, high purity ZnO and TiO_2 thin films were used in an inverted OSC as the ETLs and the HBL. The aim of the study was to find a combination of the optimal concentration of precursor solution and the post-annealing process method to produce textured ZnO and TiO_2 thin films to improve charge transfer in an inverted OSC; hence improving the photovoltaic performance. Moreover, an interface layer of MoO_x between the blend layer of P3HT:PCBM and the top contact Ag was fabricated by the spin coating method and thermal evaporation, respectively. This is beneficial for the device, providing efficient hole collection and electron blocking capabilities and exhibiting a protection layer during contact deposition. However, the hydrophobic solution-processed MoO_x hole transport layer introduces an issue of not being viable for direct contact onto the P3HT: PCMB active layer and thus resulting in a non-responsive device.

In chapter 2, a description of the deposition conditions in the preparation of the two metal oxides in the current study is described, with detailed analytical techniques used to characterize the thin films. The techniques include XRD for the determination of the structural changes which may have occurred during the heat treatment, HR-SEM were used to study the change of the surface of the material, with respect to the different annealing methods. The optical parameters such as the Tauc band gap were determined with the use of the optical transmission measurements. Furthermore, electrical characterization was employed to describe the behaviour of the inverted OSC.

HR-SEM analysis of ZnO and TiO_2 thin films prepared by different concentrations of precursor material and ramp annealing method revealed

that various morphologies such as ridges and porous structures could be produced. As a consequence of the growth process and the concentration of the precursor solution, the size of the structures was observed to have an effect on the overall roughness of the thin films. The thickness of the ZnO ridges ranging from 130 nm for lower concentration to approximately 500 nm for higher concentration. It was also observed that TiO_2 has porous structures with sizes in the low hundred nanometres for higher catalyst concentration and up to a micron for lower catalyst concentration. These structures are beneficial for thin film application in light-harvesting application since they exhibit greater light scattering capabilities; hence enhancing photon absorption.

Additionally, the ZnO and TiO_2 thin films fabricated by the spin coating method and conventionally annealed are investigated in comparison to the ramp-annealing method. A comparison of the two types of thin films was conducted, to observe the influences on the device performance. Analytical techniques describing how the overall structural and optical properties of the thin films are affected during the respective annealing methods were studied. HR-SEM analysis revealed that the morphology of ZnO and TiO_2 thin films can be controlled by the chosen annealing conditions. The major significant difference between the two annealing series described is the difference in the morphology of the thin films. The two annealing series revealed a granular and superior flat surface for conventionally annealed thin films and for ramp annealed samples a ridge-like and a porous structure for ZnO and TiO_2, respectively. X-ray diffraction peaks exhibited the ZnO thin films for both annealing types are crystalline and has a hexagonal wurtzite structure after annealing. Conventionally annealed ZnO thin film showed a greater size of grains and an increase in film strain compared to the ramp-annealed sample. The TiO_2 thin film, however, reveals a tetragonal structure for only the conventional annealed sample, with mixed anatase and rutile phases. The ramp-annealed TiO_2 sample did not show any relevant peaks to analyze. FTIR was employed to study the chemical structure of the

thin films and it was revealed that for both annealing parameters the individual layers were completely transformed into ZnO and TiO_2, respectively. Significant optical properties of the thin films illustrate that they are highly transparent with average transparency of approximately 80% for all. The presence of the textured structures on the surface of the ramp-annealed ETLs exhibits decreased transmittance compared to the conventionally annealed ETLs which is consistent with the light scattering effect for both the ZnO and TiO_2 ramp-annealed thin films. Overall the optical band gap red-shifted and blue-shifted for the ZnO thin films and TiO_2 thin films, respectively.

The incorporation of ZnO and TiO_2 thin films as electron transport layers with the active layer of P3HT:PCBM, the hole transport layer MoO_x and a silver electrode in inverted OSCs was investigated. The thin film of ZnO and TiO_2 in the OSC was varied between a ramp-annealed thin film and a conventionally annealed thin film. The MoO_x thin film was varied between two processes namely, thermal evaporation and spin coating method. The photovoltaic properties demonstrated a PCE of 3.32% in ZnO system and 2.49% in TiO_2 system. This was due to the incorporation of ZnO ridges, which facilitates the electron transport in the photoactive layer resulting in improved efficiency. Therefore, based on the above analyses we can conclude that ZnO is the most desirable ETL for improved efficiency.

Future work and Recommendations

A manuscript emanating from this work for participation at the **International Conference on Surfaces, Coatings and Nanostructured Materials (NANOSMAT-Africa)** was submitted for publication in Materials Today: Proceedings. Follow-up studies is planned to fabricate all solution-processed inverted OSCs to explore the effect of the film morphology produced from the two different annealing approaches on photovoltaic performances by using alternative active layer materials.

Additionally, exploring ways to enhance the adhesion properties of the solution processed MoO_x thin film can be investigated. An exploration into the air stability and illumination stability of the inverted OSCs can also be considered. Finally, an exploration into applying the mesoporous TiO_2 thin film and the ridge structure ZnO thin films in perovskite solar cells is considered.

7 Appendix

Appendix A1: XRD of solution processed MoO_x thin film.

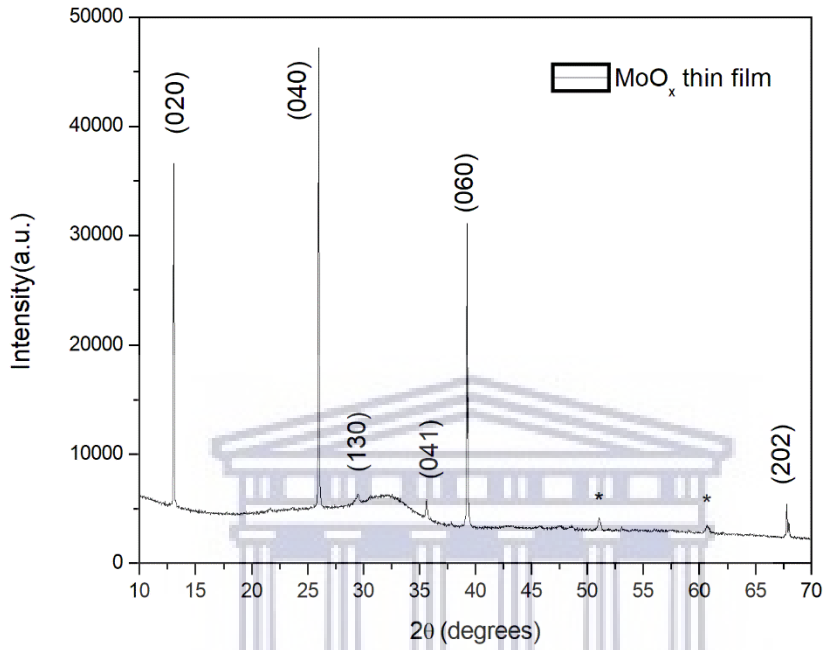

Apendix A2: Optical properties of solution-processed (S) and thermally-evaporated (T) MoO_x thin film.

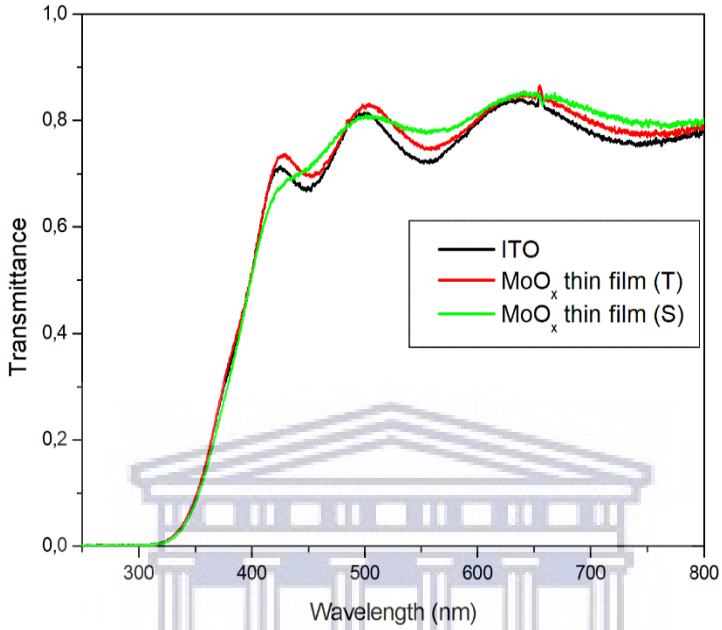

Optical properties of (a) solution-processed and (b) thermally-evaporated MoO_x thin film.